Physics and engineering of natural catastrophes : accelerometric and optical techniques to tracking solid intruder's penetration into liquefied soils

Gustavo Antonio Sanchez Colina

UNIVERSITÉ DE STRASBOURG

*ÉCOLE DOCTORALE _Sciences de la terre_*

Institut de Physique du Globe de Strasbourg, UMR7516

EN COTUTELLE AVEC LA UNIVERSIDAD DE LA HABANA

FACULTAD DE FISICA

THÈSE

présentée par :

Gustavo Antonio Sánchez Colina

soutenue le : **23 septembre 2016**

pour obtenir le grade de : **Docteur de l'université de Strasbourg**

Spécialité : Géophysique

Physique et ingénierie des catastrophes naturelles : techniques accélérométriques et optiques pour le suivi de pénétration d'intrus solides dans des sols liquéfiés.

THÈSE dirigée par :

Renaud Toussaint	**DR CNRS, IPGS, CNRS/Université de Strasbourg**
Ernesto Altshuler	**Pr, Universidad de La Habana**

RAPPORTEURS :

Stéphane Santucci	**CR CNRS, HDR, Laboratoire de Physique, ENS de Lyon**
Osvanny Ramos	**MdC, HDR, Institut Lumière, Université de Lyon II**

AUTRES MEMBRES DU JURY :

Mustapha Meghraoui	**Pr, IPGS, CNRS/Université de Strasbourg**

Dedicace

Para Alicia.

Remerciements

My acknowledgments list is so large, I’ll rather speak. I hope it will not take more than the presentation.

Contents

List of tables

List of figures

List of appendices

Introduction.

A natural hazard can be defined as a sudden natural event that has potential risk, i.e. can cause harm to people and constructions. It is an environmental phenomenon that can be induced by atmospheric, hydrologic, geologic, and wildfire-related occurrences. The level of risk associated with these hazards varies by location, season, and probability of a particular hazard occurring. Some of them –such as tropical storms and volcano eruptions– can be partially forecasted, while other –like earthquakes, mudslides and tornadoes– cannot. This thesis will focus on natural catastrophes associated to granular soils, particularly when they are fluidized, for example, in the presence of vibration –which may occur during earthquakes.

In just a matter of seconds an earthquake can cause massive damage, and leave thousands of people dead, injured, or homeless. Disruption of lifelines, transportation systems, and communication systems can be critical. The main geologic hazards associated with moderate-to large-magnitude earthquakes include ground shaking, surface fault rupture and tectonic subsidence, soil liquefaction and related ground failure, landslides, and various types of flooding.

The attention of this thesis will concentrate mainly in the penetration of intruders into dry fluidized granular beds, as an experimental model for buildings, or even vehicles. Fluidization can be provoked by vibrations –as in the case of an earthquake– by the stress associated to the penetration of an intruder into a particular granular material –as in the case of ultra-light grains– or even during penetration in an environment of decreased gravity –as the case of the sandy surface of an asteroid. In Chapter 1 of this thesis, an introduction to the penetration of intruders into dry granular matter is provided, as illustrated at the upper left corner of Fig I.1.

Chapter 1, however, will not deal with high-speed penetration of intruders (Ciamarra, Lara, Golman, Vishik, & Swinney, 2004) a subject very much studied in connection to ballistics and to impact cratering in astronomical objects. The chapter aims at the physics of low-velocity penetration, prominently including the case where the intruder starts resting on the free granular surface. It is discussed the seminal work of Tsimring and Volfson (Tsimring & Volfson, 2005)

where both experiments and simulations are used to determine the main contributions to energy dissipation during the penetration of an intruder into a granular bed. They conclude that the main sources of dissipation, are: (a) The inelastic collisions between the grains and between the grains and the intruder (b) Friction due to particle-particle sliding and intruder-grain sliding (c) Kinetic energy of the granular material ejected during collision into the air and (d) Increased potential energy of the granular bed due to the penetration of the intruder.

Careful experiments at Doug Durian's group resulted in a so-called "universal" force law for slow penetration of intruders into granular material (Katsuragi & Durian, Unified force law for granular impact cratering, 2007). In principle, it is possible to write Newton's second law for the intruder, where the gravitational force acts vertically down, and two distinct forces associated to the granular material act vertically upwards: (a) a "viscous-like" force, associated to the shocks between the intruder and the grains and (b) a "depth-dependent" force expressed as a certain constant times the depth into the granular material. The force is not completely understood, but is definitively connected to some of the dissipation mechanisms described by Tsimring and Volfson (Tsimring & Volfson, 2005). Interestingly enough, the proportionality constant between the depth and the depth-dependent force depends on the size and shape of the intruder, and the gravity.

A few years later, Pacheco and co-workers (Pacheco-Vazquez, Caballero-Robledo, & al., 2011) proposed a refined version of Katsuragi and Durian's "universal law": they modified the "depth-dependent" force term in such a way that interaction with the walls of the container is included: differently from liquids or solids, granular matter includes the so-called "force chains", i.e., a grain that interacts with a wall by friction, may transmit that interaction to the center of the container through chains of grains that are in good mechanical contact with each other: the walls help in that way to support the weight of an intruder located in the middle of a granular silo. Pacheco and co-workers introduced an exponential dependence in the depth-dependent force term in such a way that the Janssen effect is taken into account: for small penetration depths, Katsugari and Durian's law is recovered, while for high penetration depths, the term becomes depth-independent, so a "terminal speed" (typical of penetration in fluids) can be attained. The equation of motion of Pacheco and coworkers (Pacheco-Vazquez, Caballero-Robledo, & al., 2011) , illustrated at the top-left corner of Fig. I.1, will be used as a framework to explain the behavior of the penetrating intruders examined in later chapters.

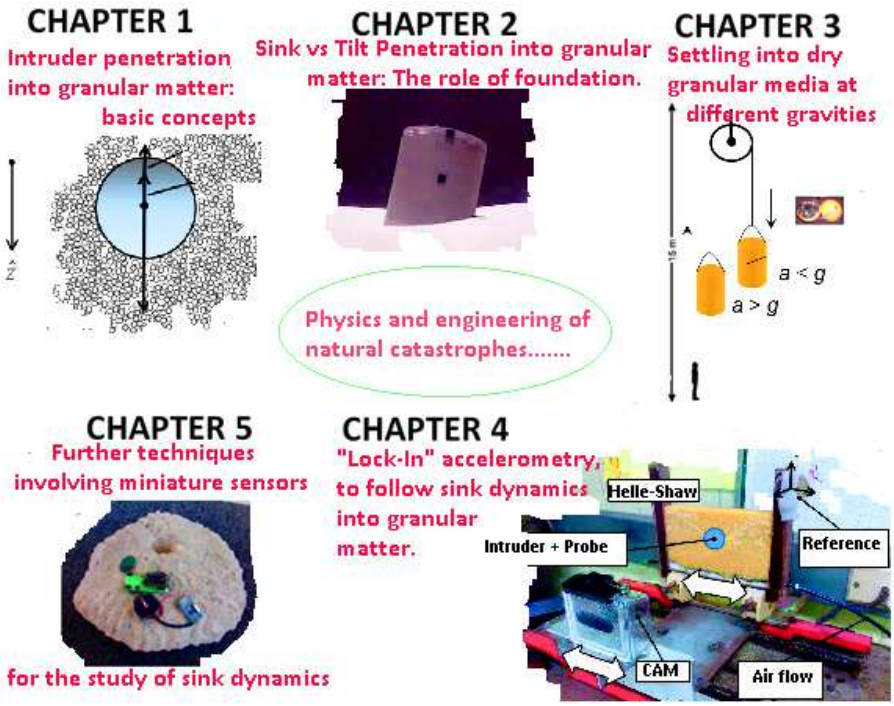

Chapter's structure of the thesis.

The thesis is organized in five chapters, four of them associated to scientific papers. Moving clockwise, starting from the top left: Chapter 1 offers an introduction of the penetration of intruders into granular matter. By means of image processing, Chapter 2 presents original findings relative of the penetration of an intruder into vibro-fluidized granular matter, and how it depends on its foundation. Using a wireless accelerometer, Chapter 3 provides new insights on the penetration of an intruder into granular matter fluidized by stress, at different gravities. Chapter 4 introduces a new technique for the study of penetration dynamics into vibro-fluidized granular matter using a couple of wireless accelerometers. Chapter 5 introduces the implementation of different electronic platforms for the study of intruder penetration into fluidized granular beds by means of miniature sensors.

But let us come back to the subject of soil fluidization. The importance of this effect in the scenario of natural catastrophes can be illustrated by the case of the Kocalei earthquake that occurred on August 17, 1999. It severely damaged many constructions in the city of Adapazari, Turkey. In particular, some buildings sank into the ground, others tilted, and a third group even shifted laterally, presumably due to soil liquefaction (Sancio, Bray, & als., 2004). In fact, shear waves released during earthquakes eventually generate cyclic shear stress that lead to the gradual buildup of pore water pressure. This may result in extended liquefaction, which has been studied on sandy, granular, and sedimentary soils (Berrill & Davis, 1985) (Obermeier

Stephen F, 1996) (Vanneste K. Meghraoui M. Camelbeeck T, 1999). But, how does an artificial construction like a building react when sitting on ground partially fluidized due to seismic waves? Does it sink, or perhaps tilt laterally? Does the behavior depend on the intensity and frequency of the seismic wave? Or perhaps the shape and size of the construction is the key element to predict its fate? We attempt to answer some of these questions in the first of the three papers presented in this thesis, which is presented in Chapter 2.

The experimental setup presented in Chapter 2 simplifies the actual scenario using a very basic setup: a box of dry sand is shaken laterally, in such a way that both the amplitude and frequency of the oscillations are controlled –illustrated at the top-center of Fig. I.1. While granular matter itself displays a variety of puzzling phenomena (Jaeger & Nagel, 1992), (Altshuler et al. 2003), (Altshuler et al. 2008), our understanding of the dynamics of objects penetrating into granular media has advanced quickly during the last decade or so (Uehara, Ambroso, Ojha, & Durian, 2003) (Katsuragi & Durian, Unified force law for granular impact cratering, 2007) (Pacheco-Vazquez, Caballero-Robledo, & al., 2011) (Torres, Gonzalez, & als., 2012) (Goldman & Umbanhowar, 2008) (Boudet, Amarouchene, & als., 2006) (Kondic, Fang, & als., 2012). In that context, laterally shaken granular beds have received a certain degree of attention (Metcalfe, Tennakoon, & als., 2002), but the performance of objects initially laying on the surface of a granular bed submitted to lateral shaking has been much less studied (Tennakoon, Kondic, & Behringer, 1999) (Liu & Dobry, 1997). The subject is tackled in Chapter 2 of the present thesis.

The penetrating object studied here is a “model building”: it simply consists in a 3D-printed cylinder with a flat bottom, studied against a similar cylinder where a “foundation ring” is added. Against intuition, for a range of frequencies and amplitudes available in the laboratory conditions –and relevant to real earthquake scenarios– the following behavior is observed: “model cylindrical buildings” with flat bottoms sink vertically, while those with a foundation shaped as a ring attached to its bottom, tilt laterally. The details of the dynamics are carefully followed by image analysis of videos taken with a camera attached to the laterally shaken box, for which *ad hoc* computational tools were created.

In spite of such quite surprising behavior, the physical explanation of the observed phenomena is quite simple. First, it must be said that, as a granular bed is shaken horizontally, there is a distinct layer of fluidized granular matter from the free surface to a certain depth, which

increased in general with the maximum dimensionless acceleration of the shaking: the fluidized layer acts, in many respects, as a true liquid. Below it, the granular bed resembles a solid. When a flat-bottom cylinder is released on the free surface, if just sinks vertically, eventually stopping as its bottom reaches the solid phase of the granular bed. However, if a ring is added to the bottom of the cylinder, the friction against the laterally shaken sand increased at the base of the cylinder, producing a tilting torque. As a result, the cylinder tilts –besides sinking. The tilting behavior, however, is found also in the case of no-ring cylinders if strong enough lateral shaking is provided –a range not easily achievable by the available experimental set up.

In the paper included in Chapter 2, the 3D experimental evidence is corroborated by 2D computer simulations where disk-shaped grains and flat cylinders with and without "basement" follow basic Newtonian dynamics. Moreover, the experimentally observed sink dynamics is reproduced using an equation of motion that considers the interaction of the intruder with granular matter following an appropriately modified equation of motion (Pacheco-Vazquez, Caballero-Robledo, & al., 2011), as pointed our earlier.

Chapter 3 uses a different tool to study the penetration into very light granular matter: a wireless accelerometer mounted inside a spherical intruder. Here, the granular bed is not shaken: it is easily fluidized by the stress caused by the gravity-driven penetration of the intruder, since it consists in ultra-light beads of expanded polystyrene originally introduced by Pacheco and co-workers (Pacheco-Vazquez, Caballero-Robledo, & al., 2011). The penetration of the intruder is followed by a wireless accelerometer, whose output is integrated two times to get the velocity vs. time record, and then, the depth vs. time record. To the authors' knowledge, this is the first systematic investigation of the penetration of an intruder equipped with a wireless accelerometer into granular matter. From the physical point of view, however, the main novelty of this work is the fact that the penetration process has been studied at different effective gravities, equivalent to experiments performed in other planets, like Mars($g_{Mars} \approx 0.4 g_{Earth}$). This kind of study is potentially important to design buildings and rovers able to perform efficiently on sand surfaces at gravities lower (and also higher) than that in the Earth. The different gravities are attained in a very simple and inexpensive way: instead of using zero-g planes or performing experiments in a space station, a 15-meter-long Atwood machine is used to control the acceleration of one of the counter-weights, which is, in fact, an accelerated granular laboratory thanks to the use of wireless technology.

The experiments have revealed two main facts: (a) The maximum depth of penetration of the intruder is independent from gravity and (b) The total sink time is proportional to the inverse of the square root of the acceleration of gravity. The first output is quite unexpected, but can be rationalized in the following way: as the gravity decreases (or increases) the weight of the intruder decreases (or increases), but this effect is compensated by a decrease (or increase) in the compaction of the granular material which results in different levels of dissipation. These qualitative ideas can be quantitatively justified using the equation of motion proposed by Pacheco and coworkers (Pacheco-Vazquez, Caballero-Robledo, & al., 2011) assuming that the coefficient of proportionality between the depth-dependent force and the penetration depth (in the case of low penetrations) is proportional to the effective gravity. The experimental finding that the maximum penetration is independent from gravity can be potentially useful to design more efficient Mars rovers[1], and also to explain features at the surface of Mars and other astronomical bodies, such as craters and gullies (Shinbrot, Duong, & als., 2004) (Aspaugh, 2007) (Almeida, Parteli, & als., 2008).

As said before, the integration of the vertical acceleration record allows to determine the evolution of velocity and depth as time goes by. The results are good for relatively fast penetrations into a bed of expanded polystyrene beads, but they are too noisy if the intruder penetrates at low speeds: that is the typical case in the penetration into a horizontally shaken bed of sand. In particular, if an intruder penetrates into a three-dimensional box of sand which is fluidized by horizontal shaking, videos are good while some section of the intruder is outside the sand (like the case described in Chapter 1), but they are of no use when the intruder sinks completely into the granular bed. So, if both video and simple accelerometric techniques are not good enough to follow the whole penetration process, what can be done?

A possible answer is presented in Chapter 4 of the thesis. A Hele-Shaw cell full of sand is laterally shaken, and an intruder is put on the surface of the sand in order to observe the penetration process, which is observed –as a reference– by means of a video camera attached to the horizontally shaken reference frame. The heart of the measuring system is the deployment

[1]It is well known that one of the rovers sent to Mars by the NASA got trapped in a very shallow dune of sand by 2009.

of two identical, wireless accelerometers: one (called *Ref*) is fixed to the Hele-Shaw cell, while the second one (called *Probe*) is attached to the sinking intruder (see the lower right corner in Fig. I.1). Instead of recording the vertical accelerations –useless due to the slow penetration process– we record the horizontal accelerations, and then calculate the correlation between them, through the Pearson's coefficient. This idea is inspired in lock-in amplifiers (LIA), an instrument commonly used to measure low-level voltages. In a typical setup, a sample is excited with an AC current, which is also injected through the "Ref" input of the LIA. The output signal from the sample –which is a "modified version" of the input excitation thanks to physical properties of the sample– is then injected by the "In" terminal of the LIA. Then, the device multiplies and filters the two signal. It is easy to show that the result is a DC signal proportional to the physical property of the sample than is supposed to be measured, and, quite importantly, *most external noise is eliminated*. It is easy to see the analogy between the LIA and the Lock-in accelerometry concept introduced here.

The idea behind the specific experiment presented in this thesis is the following: when the intruder is sinking, it cannot be tightly bounded to the granular mass, so there will be a delay between the horizontal accelerations measured by *Ref* and *Probe*, so the correlation between them is near zero. On the other hand, when the intruder ends the sinking process and lands on the "solid granular phase", it starts to move synchronously with the reference frame, and so the correlation between the Ref and Probe accelerations approaches unity. At least, using this method we can determine the exact moment when the intruder has stopped sinking.

Preliminary experiments show that we can detect (a) the moment when the intruder touches the "solid phase" at the end of the sinking process and (b) at least to different stages during the process before stopping: one of fast penetration, and a second of "creeping" penetration. In the future, it is worth examining if the study of other features of the correlation besides its amplitude could be used to reveal subtler features of the penetration dynamics. Although the method of Lock-in Accelerometry has been just presented here, it might be of interest as a standard system to track the motion of man-made or natural structures as they sink or move in shaking soils.

Up to this stage, the experiments described in the thesis have used (a) standard video acquisition equipment and (b) wireless accelerometer platforms which are available in the market with proprietary software. In the last chapter of the thesis, a number of new measuring platforms able

to support miniature sensors developed by the author are presented. Additionally, a wireless accelerometric platform as the one used up to here has serious limitations for certain experiments and applications of geophysical and environmental interest. One example illustrates the idea: the study of the erosional effect of waves and winds on the bottom of sandy beaches in Cuba –presently an important problem aggravated by frequent storms associated to "El Niño". One possibility to perform such study is to mount wireless sensors and GPS devices into "sample rocks", and deploy them at critical points on the bottom of a beach: the sensors inside the rock may allow reconstructing the motion of the sample rock on the sand, in entirely natural conditions. The rock will act as the intruders studied in lab conditions in previous chapters, and the sandy bottom will be a fluidized granular bed –both due to shaking associated to waves, and to the presence of actual fluid.

A wireless accelerometer will pose serious technical challenges in such experiment, since the signal can be easily lost for at least three causes: (a) If the rock moves more than 10 meters from the receiver (even in air), the signal is interrupted (b) The situation described is eventually aggravated by the sea water itself, which may act as an electromagnetic shield and (c) The need to have a receiver relatively near the rock carrying the sensor during the whole experiment can be inconvenient –especially in a salty and eventually windy environment. Then, data logging seems the solution: the sensor would discharge data in a local miniature memory device also mounted into the rock, and it is discharged later to a computer.

ARDUINO (Severance, Jan. 2014) has been the choice as a platform to control the miniature sensors. It has basically all the advantages searched for in this thesis: the design is open, and can be programmed in the C language, a standard independent for the operating system. On top, it can be assembled quite compactly, which facilitates its deployment into, for example, a sea rock. Sensors including a tri-axial accelerometer and a wireless module are controlled by the Arduino. For the data storage, several standards have been studied, considering different parameters, such as storage capacity, data acquisition speed, error margin in data transfer, operation autonomy –basically given by power consumption– and ability to control multiple sensors. So, for example, while Bluetooth excels in terms of storage capacity and autonomy, micro-SD cards is the choice when multiplicity is necessary. FRAM, on the other hand, is excellent both in terms of multiplicity and speed. These choices –always under the ARDUINO platform– are preliminary tried both in laboratory conditions (intruder penetrating into a shaken

box of sand) and in natural conditions, when installed into rocks deployed in a Cuban sandy beach.

In summary, the basic goal of the thesis is *to study the behavior of intruders in fluidized granular matter, eventually creating new experimental techniques to achieve that goal.*

In particular, the objectives of the thesis, are:

a) To determine the influence of the kind of basement in the behavior of a cylinder used as a model of a human construction or a rock, when it penetrates a vibrofluidized granular bed.
b) To establish the influence of gravity in the sinking of a spherical intruder into light granular matter, measured by wireless accelerometry.
c) To create an accelerometric technique suitable to study the slow penetration of an intruder into vibro-fluidized granular matter.
d) To implement an open-core and open-software Arduino-based platform to study the behavior of intruders into fluidized granular matter both in laboratory and in natural conditions.

Chapter 1: Penetration Of Intruders Into Dry Granular Media: Basic Concepts.

Penetration of solid objects into soils has been, for a long time, the reign of civil engineers, Earth scientists and astronomers. However, since the 1990's the matter has become a physicists' "hot topic". In particular, during the last decade the "physical understanding" of the resistance to objects penetrating into granular media has advanced quickly (Albert, Pfeifer, Barabasi, & Schiffer, 1998) (Uehara, Ambroso, Ojha, & Durian, 2003) (Walsh, Holloway, Habdas, & deBruyn, 2003) (Tsimring & Volfson, 2005) (Katsuragi & Durian, Unified force law for granular impact cratering, 2007) (Goldman & Umbanhowar, 2008) (Pacheco-Vazquez, Caballero-Robledo, & al., 2011) (Boudet, Amarouchene, & als., 2006) (de Vet & de Bruin, 2007) (Chen, Umbanhowar, & als., 2009) (Brzinski & Durian, 2010) (Constantino, Bartell, & als., 2011) (Dorbolo, Ludewig, & Vandewalle, 2013) (Katsuragi, Nonlinear wall pressure of a plunged granular column., 2012) (Kondic, Fang, & als., 2012). In this chapter, a limited number of key results in that field will be briefly presented. Due to its direct connection to later chapters of the thesis, emphasis will be put on the *slow* penetration of intruders into granular matter –a typical example being an object that starts its motion from a rest position on the free granular surface. For a more general overview of the field, the recent review by C. Ruiz Suárez (Ruiz-Suarez, 2013) is recommended.

1.1 Some scaling laws for intruder penetration.

Tsimring & Volfson (2005) carried out low-speed impact experiments of solid objects into granular media, in order to reproduce geophysical events and to test the unusual nature of the granular state of matter. Their observations were interpreted in terms of conflicting stopping forces expressed as powers of projectile depth and speed. Depending on the case, these were linear in speed; constant, proportional to the initial impact speed; or proportional to depth. In order to study the resistance forces in granular media during impact and the mechanisms of energy dissipation the projectile size, density, and impact velocity, as well as friction among the grains were systematically varied in their experiences. They found a final or stop time which decreases with increasing impact speed. In addition –and unexpectedly– the experiments

showed that deeper penetration requires less time. This suggested they that a single, "unified" force law underlies for all of the observations.

Tsimring and Volfson established the different ways for the energy redistribution during penetration (illustrated in Figure 1.1):

1. Lifting of grains during crater formation.
2. Inelastic collisions between the body and the grains and among the grains during impact.
3. Friction due to particle sliding contacts and body-grain sliding.

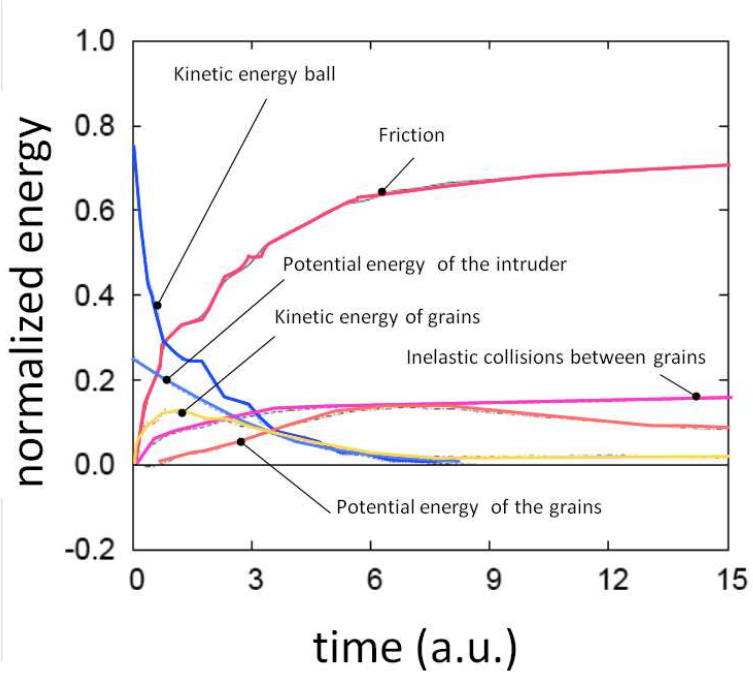

Figure 1.1 Energy dissipation of a spherical intruder sinking into a granular matter.

On the Figure 1.1 the simulation shows that the total energy of the intruder (kinetic plus potential) decreases as the penetration process takes place. In the end, most of it is dissipated as frictional energy, but inelastic collisions also contribute. The increase in the average potential

energy of the grains also gets a fraction of the initial energy of the intruder (Figure adapted from Tsimring and Volfson, 2005).

At low speed, the energy losses on friction between the intruder and the grains is negligible. For large impact energies, the kinetic friction term $\alpha \dot{s}^2$ has to be taken into account, which affects the initial phase of the object deceleration. Interestingly, the additional deceleration caused by the kinetic friction reduces the depth of penetration (it deviates from the linear scaling even for large penetration depths).

For small impact speeds, Durian & coworkers (Uehara, Ambroso, Ojha, & Durian, 2003) found the following scaling relationship between the crater depth *d* (defined as the distance between the unperturbed surface and the lowest point of the projectile at rest) and other parameters of the impact:

$$d = 0.14\mu^{-1}\left(\rho_b/\rho_g\right)^{\frac{1}{2}} D_b^{\frac{2}{3}} H^{\frac{1}{3}} \qquad (1)$$

Here, ρ_g, ρ_b are densities of grains and the spherical intruder, respectively, μ is the grain-grain friction coefficient defined through the repose angle of the grains θ, $\mu = tan\theta$, D_b is the diameter of the ball, and *H* is the total drop of the ball (the sum of the free-fall height $h = v_0^2/2g$ and the total penetration depth *d*).

From experiments at high impact velocity, (Ciamarra, Lara, Golman, Vishik, & Swinney, 2004) found that after a short initial phase, a "penetration phase" ensues, during which the deceleration of the ball *a* is roughly constant. This scaling implies that the stopping time is independent of the initial velocity, and the penetration depth is proportional to the square of the initial velocity:

$$d = \frac{v_0^2}{2a} \qquad (2)$$

A linear scaling between the ball penetration depth and the impact momentum mv_o was reported by de Bruyn & coworkers (Walsh, Holloway, Habdas, & deBruyn, 2003). The established theory of impact penetration (Forrestal & Luk, 1992)is based on the so-called Poncelet model, which assumes that the force acting on the object consists of three components: gravity $m_b g$, static resistance force F_z, and dynamic frictional force αv^2. Then the Newton's law is written as:

$$m_b \ddot{z} = m_b g - F_z - \alpha \dot{z}^2 \qquad (3)$$

where *z(t)* is the vertical coordinate of the lowest tip of the object with respect to the surface. Integrating this equation with appropriate boundary conditions and assuming constant F_z yields the so-called Poncelet formula for the maximum penetration depth:

$$d = (2\alpha)^{-1} log[1 + \alpha v_0^2 (F_z - m_b g)^{-1}] \qquad (4)$$

The dimensional parameter α is proportional to the cross section of the ball. This formula works reasonably well for medium- and high-speed impacts however it fails to describe low-speed impacts.

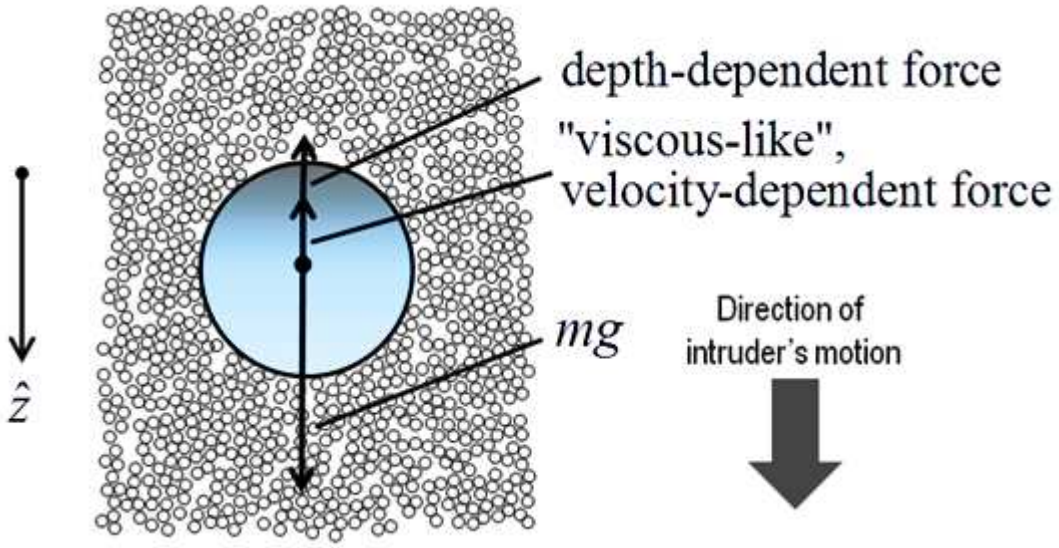

Figure 1.2 Force diagram of an intruder sinking into granular matter. The gravity force competes with two stopping forces pointing upwards.

Using 3D finite element simulations, Tsimring & Volfson generalize (3) and (4) in order to describe low-speed impacts. They focused on the depth-dependence of the static resistance force. Albert and co-workers showed experimentally (Albert, Pfeifer, Barabasi, & Schiffer, 1998) that in a slow drag regime the force acting on an object is proportional to its cross section times the local pressure. Following that, Tsimring & Volfson considered in the initial phase the free surface fixed at $z = 0$, and the pressure as $p = \rho_g g z$ (here ρ_g is the effective density of the granular material). In the penetration phase, the free surface moves down with the ball, so the pressure under the ball can be taken as $p = \rho_g g z_o$. Here $z_o = z - z_{zf} = cons = O(D_b)$, where z_{zf} is the position of the free surface near the ball.

The 3D discrete element simulations, yields a “static drag force” as:

$$F_z = \begin{cases} \eta \rho_g z^2 D_b, & z \ll D_b \\ \eta \rho_g z_0^2 D_b, & z \gg D_b \end{cases} \quad (5)$$

Where η is a dimensionless parameter dependent on the material properties of the grains and the ball (e.g., friction coefficient).

For small impact energies, the 3D scaling agrees with the experimental results of Durian’s group (Uehara, Ambroso, Ojha, & Durian, 2003), and for larger impact energy the model describes the transition to the penetration phase with constant deceleration in agreement with Ciamarra and coworkers (Ciamarra, Lara, Golman, Vishik, & Swinney, 2004).

These results suggest that for small initial speeds, the penetration depth scaling is reasonably well described by the Poncelet equation (Eq. 4) with a depth dependent static friction force (Eq. 5).

1.2 The "unified force law" of Katsuragi & Durian.

Katsuragi & Durian agreed with Tsimring & Volfson in the sense that a single, unified, force law underlies all of the observations on their experiments. Tsimring & Volfson argued that the form of F_z should vary from quadratic to constant owing to the shapes of the projectile and of the growing crater excavated by its motion. Such a force law can approximately account for a depth scaling $d = (d_0^2 H)^{1/3}$. The order of magnitude of this force is larger than that expected just from the Coulomb friction.

Katsuragi & Durian departed from the hypothetical formula:

$$\sum F = -mg + F_z + \frac{mv^2}{d_i} \quad (6)$$

were F_z is the term for the Coulomb friction and the last one is the inertial drag and d_i is a constant. Combining it with Newton's second law, the acceleration at a given fixed depth z_i should be quadratic in speed $a + g = \frac{F_{zi}}{m} + {v^2}/{d_i}$, where a is the acceleration of the intruder. They did tries for several depths z_i and found the same proportionality factor d_1 for all depths.

The good agreement of this expression with the experimental results indicates that the projectile experiences a force ${mv^2}/{d_i}$ that is independent of depth. In addition, they found an expression for the inertial force required for the projectile to mobilize a volume D_b^3 of granular material with density ρ_g (${mv^2}/{d_i}$ scaling as 0.8 $\rho_g D_b^2 v^2$).

Using the d_1 value, they found an expression for the Coulomb's friction term and even when Tsimring & Volfson argued the quadratic to linear variation in the expression of the force, Katsuragi and Durian found that a linear fit worked well over most of the experimental range. This suggested the friction term to be:

$$F_z = k|z| \,, \qquad {k}/{m} = 1.040 \pm 10\ s^{-2} \tag{7}$$

So the force law becomes:

$$\sum F = -mg + k|z| + {mv^2}/{d_i} \tag{8}$$

with order of magnitude of ${mv^2}/{d_i} = \rho_g D_b^2 v^2$ determined by the granular density and cross section area of the penetrating body. The characteristic length scale is given by the diameter of the body $L_c = D_b$ so the penetration depth is within an order of magnitude of the body diameter for a wide range of impact speeds. The time is contained in the gravity term, so the characteristic time and velocity scales as $T_c = ({D_b}/{g})^{1/2}$, which explains the typical stopping time and the velocity beyond which the typical stopping time becomes constant. This force law described the acceleration discontinuity as the body stops as $\Delta a = -g + (k/m)d$.

As the authors held “The only puzzles that remain are the linear form of the Coulomb friction term plus the precise values of k and d_1, as well as their scaling with system properties”.

1.3 Pacheco-Vázquez et al.: introducing Janssen's effect.

These achievements were insufficient to describe the dynamics when bodies penetrated inside granular media. Pacheco & coworkers in 2011 (Pacheco-Vazquez, Caballero-Robledo, & al., 2011) analyze the case when the depth-dependent force saturates with depth due to the presence of walls.

Reviewing the linear expression proposed by Katsuragi & Durian in 2007 (Katsuragi and Durian 2007) the term corresponding to Coulomb’s friction, should be dependent on the pressure, so, they incorporate the pressure p as a Janssen-type dependence on depth z:

$$P(z) \propto \rho g \lambda (1 - e^{-z/\lambda}) \tag{9}$$

Where ρ is the bulk granular density, g the gravity, and λ a characteristic length, close in value to the diameter of the container containing the granular material. Since according to this dependence the pressure saturates, the friction felt by a penetrating object must saturate as well, and a terminal velocity ought to be reached. The new force equation rewrites as follows:

$$m\ddot{z} = mg - \eta \dot{z}^2 - k\lambda\left(1 - e^{-z/\lambda}\right) \tag{10}$$

The quadratic dependence in velocity is sufficient to describe the inertial drag, at least in loose granular materials like expanded polystyrene beads. For small penetrations, the friction term becomes linear and for large ones it is constant. The latter case explains the existence of a terminal velocity V_t when the friction term reaches a value $k\lambda$ at saturation, occurring when the acceleration is zero. This lead to:

$$V_T^2 = mg/\eta - k\lambda/\eta \tag{11}$$

Which implies that a critical mass exists, above which the intruder is able to penetrate an infinite depth, reaching a terminal velocity equal to zero. This mass is given by $m_c = k\lambda/g$ (for smaller

masses, the intruder eventually stops at some depth inside the granular silo, and, for bigger masses, it reaches a finite, constant terminal velocity).

In order to individually determine k and λ, we consider the balance between the weight of the intruder and the depth-dependent force $mg = k\lambda\left(1 - e^{z/\lambda}\right)$. Solving for $z = z_{min}$, the minimum depth from were an intruder will not sink if it were "quasi-statically put there" with zero speed is:

$$z_{min} = -\lambda ln(1 - mg/k\lambda) \qquad (12)$$

Equations (10) – (12) will be eventually used in the present thesis to interpret penetration experiments into granular fluidized beds –both due to vibrations or to the shear produced by the intruder itself into very light granular matter.

Chapter 2: Sink Vs. Tilt Penetration Into Shaken Granular Matter: The Role Of Foundation.

2.1 Article: G. Sánchez-Colina, A. J. Batista-Leyva, C. Clément, E. Altshuler and R. Toussaint. Submitted (2016).

Sink vs. tilt penetration into shaken dry granular matter: the role of foundation

G. Sánchez-Colina,[1] A.J. Batista-Leyva,[2,1] C. Clément,[3] E. Altshuler,[1] and R. Toussaint[3]

[1] *Group of Complex Systems and Statistical Physics, Physics Faculty, University of Havana, 10400 Havana, Cuba*
[2] *Instituto Superior de Tecnologías y Ciencias Aplicadas (InSTEC), 10400 Havana, Cuba and Group of Complex Systems and Statistical Physics, Physics Faculty, University of Havana, 10400 Havana, Cuba*
[3] *Institut de Physique du Globe de Strasbourg (IPGS), Ecole et Observatoire des Sciences de la Terre (EOST), University of Strasbourg/CNRS, 67084 Strasbourg, France*

(Dated: April 23, 2016)

We study the behavior of cylindrical objects as they sink into a dry granular bed fluidized due to lateral oscillations, in order to shed light on the effects of earthquake-related fluidization of soils on human constructions and other objects. Somewhat unexpectedly, we have found that, within a large range of lateral shaking powers, cylinders with flat bottoms sink vertically, while those with a "foundation"consisting in a shallow ring attached to their bottom, tilt besides sinking. The latter scenario seems to dominate independently from the nature of the foundation when strong enough lateral vibrations are applied. We are able to reproduce the observed behavior by quasi-2D numerical simulations, and the vertical sink dynamics with the help of a Newtonian equation of motion for the intruder.

PACS numbers: 45.70.-n, 45.70.Mg, 07.05.Tp, 96.15.Wx, 07.07.Df

INTRODUCTION

The Kocalei earthquake occurring on August 17, 1999 affected in various ways many constructions in the city of Adapazari, Turkey. Following observers, some buildings sank vertically into the soil, others tilted, and some even suffered lateral translation over the ground [1–3]. This case illustrates well the diversity of damage that earthquake fluidization of soils may cause to man-made structures [4].

Ground fluidization [5, 6] has been investigated in different kinds of media like sand [6], dry granular soils [7] and sediments [8]. Of immediate interest for engineering and for the geosciences is to understand how man-made structures such as buildings, and massive rocks laying on granular soils respond to fluidization associated to seismic waves.

Granular matter itself displays a variety of puzzling phenomena [9–13], but during the last decade or so, our understanding of the dynamics of objects penetrating into granular media has advanced quickly [14–25]. While laterally shaken granular beds have received a certain degree of attention [26, 27], the performance of objects initially laying on the surface of a granular bed submitted to lateral shaking has been rarely studied [28–30].

In this paper we perform systematic experiments associated to the latter scenario, which may help understanding the performance of human constructions and rocks laying on granular beds during earthquakes. In particular, using a cylinder as a simplified model for buildings or rocks, we study its settling dynamics on a granular bed submitted to lateral vibrations. Somewhat unexpectedly, we have found that, within a large range of lateral shaking powers, cylinders with flat bottoms sink vertically, while those with a "foundation"consisting in a shallow ring attached to their bottom, tilt besides sinking. The latter scenario seems to dominate independently from the nature of the foundation when strong enough lateral vibrations are applied. Quasi-2D simulations were also performed mimicking the experiments. The settling dynamics of the simulated intruders, with or without foundation reproduces quite well the corresponding experimental results. We also developed a model that reproduces well the sinking dynamics and gives a qualitative explanation of the tilting process.

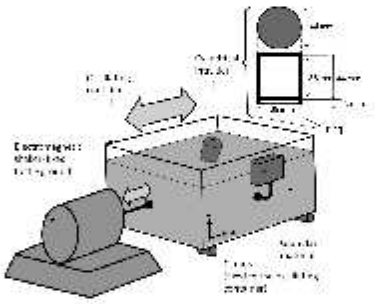

FIG. 1. Experimental setup. At the upper right, we have illustrated the intruder consisting in a cylinder with ring.

EXPERIMENTAL

The penetration experiments were performed on a granular bed contained into a test cell of approximately $25 \times 25 \times 25$ cm^3 filled with Ugelstad spheres of non expanded polystyrene with a density 1.05 g/cm^3, and diameter 140 μm (monodisperse within a 1 percent), type Dynoseeds ©, produced by Microbeads, Norway. The box was horizontally shaken at different amplitudes (A), and a frequency (f) of 5.0 Hz (a value commonly found in seismic waves), using a TIRA TV51120 shaker, type S51120, see figure 1. The maximum amplitude of oscillations allowed by the shaker corresponds to an acceleration of ≈ 12.2 m/s^2.

Two types of intruders were used in the experiments: (a) a hollow 3D printed cylinder of 44 mm diameter, 44 mm height (external dimensions), and 5 mm thick walls, and (b) the same cylinder with a ring of 5 mm height and 3 mm thickness glued to its bottom (illustrated in the upper right corner of Fig. 1). Intruders (a) and (b) will be called "No-ring"and "Ring", respectively, from now on. Their masses were adjusted with ballast in such a way that their densities matched the average effective density of the granular medium, which was measured as 0.43 g/cm^3. As far as the ballast used has a density near the effective density of the granular material, it was almost evenly distributed inside the cylinder. Note that, using a flat bottom cylinder and a ring-like bottom cylinder, we are modifying the "foundation"of our intruder.

A digital camera *Hero 2* made by GoPro was fixed to the electromagnetic shaker, in such a way that it could take a video of the sinking process from an oscillating reference frame locked to the test cell, as proposed in [30]. This method allowed a much better quality of the cylinder's images, and made easier their digital processing. Videos were taken at a maximum rate of 120 frames per second, with a resolution of 1920×1080 pixels.

The images were processed as follows. We first converted the videos to image sequences in *.jpg format, and cropped each picture, excluding irrelevant space. Then, the images were binarized through an appropriate threshold. Using the tool *regionprops* from *MatlabR2014a*, we identified and assigned coordinates to several bright marks we had glued to certain points of the cylindrical intruder. The coordinates of the marks where used to calculate the position of the intruder's geometrical center and inclination relative to the vertical in each picture. In some experiments where the sinking was particularly big, it was difficult to obtain the tilt angle, since part of the marks sank below the level of the sand surface, and they were impossible to follow. In such cases the upper border of the cylinder was identified using the Matlab's tools *find* and *bwtraceboundary*, and then fitted to a polynomial using the function *polyfit*. The fit was used to find the inclination. In the case of experiments ending in a very inclined position, the reference to calculate the inclination was the cylinder's corner above the sand surface, that was identified as the intersection of the two polynomial fits of the upper and one lateral borders of the cylinder.

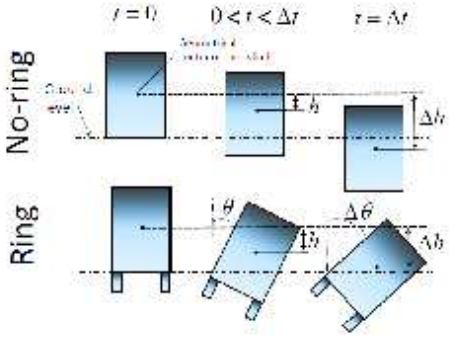

FIG. 2. Sketch of sinking and tilting processes. The top row illustrates the sinking process of a No-Ring cylinder in three moments during the experimental interval from $t = 0$ to $t = \Delta t$. The bottom row shows the same temporal sequence for a Ring cylinder, which tilts in addition to sink.

As the cylinder vibrates due to the vibration of the box, it is difficult to determine the final position, particularly when there is a big tilting. Then, in order to determine the sinking depth and tilting, we observe in the videos the onset of a cyclic movement of a reference point in the cylinder. Once this situation was reached, the final position could be measured in the frames filmed after the shaker was stopped.

The experimental protocol can be described as follows: (I) preparing the granular medium by stirring it evenly with a long rod, (II) gently depositing the cylinder in the upright position on the free surface of the granular bed, (III) turning ON the camera, (IV) switching ON the shaker after setting the desired frequency and amplitude (V) turning OFF the shaker and the camera after the penetration process had visibly finished.

In Fig. 2 we define the main parameters describing the sinking process of a No-ring cylinder (upper row), and the tilting and sinking of a Ring cylinder (bottom row), during the experimental lapse, defined as Δt. As the figure indicates, in the following we will call h the penetration of the geometrical center at a time t and Δh the total penetration. It is important to note that both magnitudes are defined as the vertical displacement of the geometrical center of the cylinder (without taking into account the ring).

We also explored the observed phenomenology through numerical simulations. They were based on a discrete

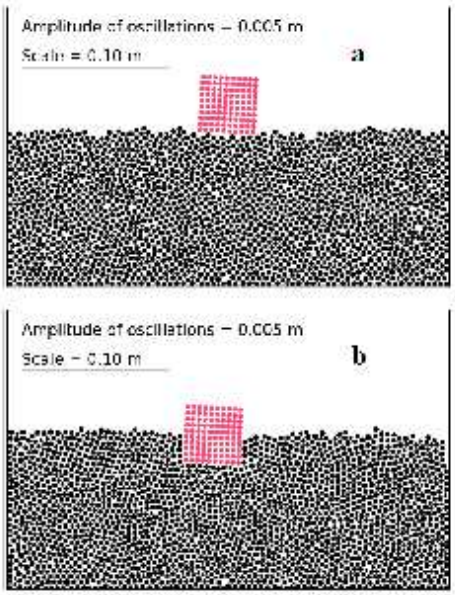

FIG. 3. (color online) Initial (a) and final (b) positions of No-ring intruder in a typical quasi-2D simulation using a frequency of 5 Hz (amplitude included in the graph).

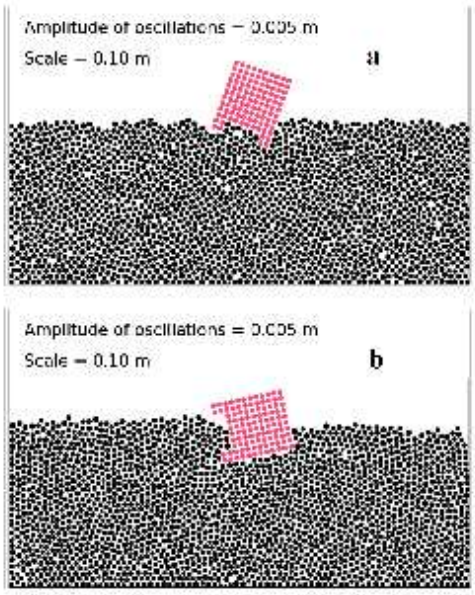

FIG. 4. (color online) Initial (a) and final (b) positions of Ring intruder in a typical quasi-2D simulation using a frequency of 5 Hz (amplitude included in the graph).

element method code (DEM) for the computation of granular system [31]. We modeled a quasi-2D granular medium, made of spheres of diameter 4 mm monodisperse within a 1 percent to avoid the effect of crystallization, and a thickness of 0.2 mm. The numerical medium contains 2000 particles, filling a virtual space of 30 cm width and 10 cm height. The code calculates the position and rotating angle of each sphere derived from the different forces applied on it. The friction coefficient μ is taken as 0.3. To approach the experimental conditions, we simulate particles of density 1.05 g/cm^3.

We created two intruders made of cohesive particles. One is a square of 40 mm side, made of 100 particles placed in a quasi-2D square arrangement, which simulates the No-ring intruder of the experiments. The second one is another square of 40 mm side attached to two small feet made of 4 particles each, mimicking the cross section of the ring attached to the bottom of the intruder. The particles density of the spheres which form the intruders is 1 g/cm^3, and the porosity of the intruders is 0.21 percent, so the intruder density is 0.78 g/cm^3, i.e., approximately the same effective density of the quasi-2D granular medium.

Once our granular medium is created, we place the intruder 1 mm above the medium. Then we let it drop and settle until the whole medium reaches equilibrium. Then, we apply a horizontal oscillation of different amplitudes and a frequency of 5 Hz to the walls of the medium and compute the time evolution of the position and tilting angle of the intruder.

Figures 3 and 4 show the initial and final positions of both types of intruders in two typical runs. Fig. 3 indicates that the No-ring cylinders almost do not tilt, while in Fig. 4 is obvious the wide inclination of a Ring one.

RESULTS AND DISCUSSION

Sink vs. tilt penetration

Figure 5(a) shows the time variation of the sinking depth for selected values of the adimensional acceleration $\Gamma = A(2\pi f)^2/g$ (where $g = 9.81$ m/s^2 is the gravitational acceleration and $A(2\pi f)^2$ is the horizontal peak acceleration of the sand box) for No-ring cylinders. It is easy to see that the penetration of the No-ring cylinders follows a common pattern for all the accelerations. A first process

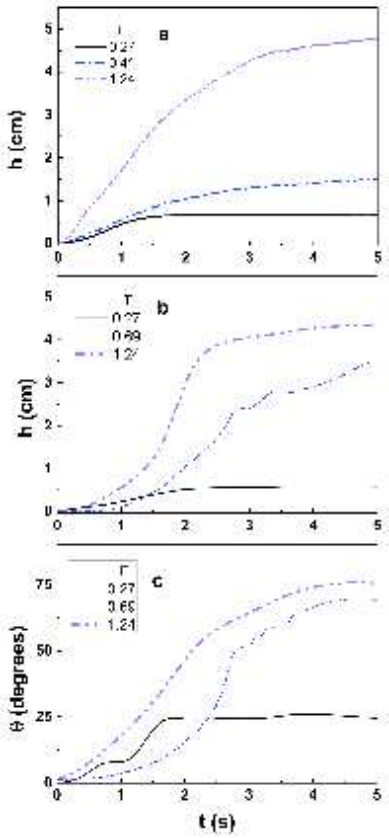

FIG. 5. (color online) Time evolution of penetration depths and tilt angles. Time dependence of the penetration depth of a No-ring cylinder (a), the penetration depth of a Ring cylinder (b) and the tilting angle of a Ring cylinder (c), for different adimensional accelerations. The long-time creep process is not completely shown. The tilting angle of No-ring cylinders is not displayed, due to the fact that it oscillates around angles not larger that 5° relative to the vertical direction

of fast sinking is followed by a slow creep. Only the penetration depth increases with Γ. In this figure we do not show the total creep process, due to its long duration. As the height of the cylinder is 44 mm, it is possible to check from Fig. 5(a) that, for an adimensional accelerations of 1.24, the cylinder sinks completely.

Figure 5(b) is similar to the previous one, only measurements were performed with Ring cylinders.

In [32] two videos labeled as "label1 "and "label2 "represent the sinking process of a No-ring cylinder and the sink-tilt behavior of a Ring one, respectively.

The general features of both graphics are very similar, but there is a difference, that will be better observed in the following figures: the adimensional acceleration at which the cylinder sinks completely in the medium is bigger for the Ring cylinders than for the No-ring ones. We could have a glimpse of why it occurs if we analyze Fig. 5(c), that presents the time evolution of the tilting angle for a Ring cylinder. Let us analyze, for instance, the curve for the highest adimensional acceleration shown in the figure ($\Gamma = 1.24$). In the first second the inclination angle reaches a value around 25°, resulting in the increase of the effective size of the intruder, with the corresponding increase of the forces impeding the sinking process (we will further develop these ideas below). All in all, it explains why the Ring cylinder sinks less than the No-ring one.

Another important difference is that the sinking and tilting dynamics of Ring cylinders is more irregular than that of the No-ring ones. It is easy to understand, if we imagine the tumbling process. Firstly the intruder gets an initial inclination along one of the two possible directions, due to the horizontal acceleration provoked by the shaker, that breaks the symmetry in a non predictable way. When the inclination appears, the gravity produces an additional torque that increases it. But, as the granular medium oscillates, the torque applied on the cylinder by the granular medium changes it orientation, provoking an oscillation in the emerged part of the intruder, so the tilting angle and the height of the center of mass relative to the surface of the granular medium also oscillate. This is illustrated in Fig. 5(b) and (c), even after being submitted to an averaging process.

In general, No-ring cylinders tend to sink vertically as the granular soil is fluidized by horizontal shaking, while cylinders with rings tend to tilt. Figure 6 quantifies the differences between the initial and final stages of the process, for almost all the range of accelerations our experimental setup was able to reach.

Figure 6(a) shows sink data for No-ring cylinders. As can be seen, the adimensional accelerations up to $\Gamma = 0.27$, there was no significant penetration of the intruder into the granular bed. Vertical penetrations started to increase significantly above $\Gamma \approx 0.3$, reaching a plateau around $\Gamma \approx 0.75$. At the plateau, the cylinder has sank completely, but stays "floating"into the fluidized granular medium, as expected for an object isodense relative to it.

In Fig. 6(b) the sinking process of the Ring cylinders is summarized. Differently from the previous case, the plateau is not observed for the range of accelerations recorded. Note that as far as the depth reached at $\Gamma \approx 1.2$ is approximately 4.4 cm (the height of the cylinder), for bigger accelerations this would also be the final penetration, so we can safely imply that the plateau appears at higher accelerations for that type of cylinders. But even at the highest accelerations, there is always a small

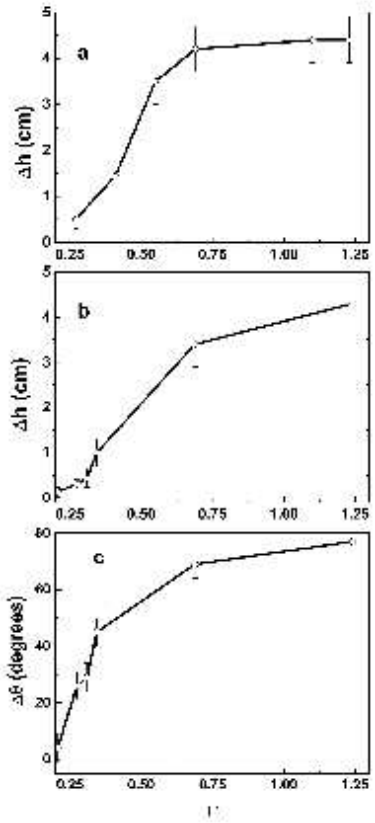

FIG. 6. Sinking and tilting: heights and angles. Final vs. initial sink heights for No-ring cylinders (a) and for Ring cylinders (b). Tilt angles for Ring cylinders (c). Tilt angles of No-ring cylinders are not shown for the same reasons of the previous figure.

part of the cylinder above the ground level.

Figure 6(c) shows the tilt data for Ring cylinders. No significant tilting is observed for Γ smaller than approximately 0.25. With the increase of the adimensional accelerations, the cylinder significantly tilts, increasing abruptly the tilting angle with Γ, until saturation starts at $\Gamma \approx 0.75$. As was stated in the figure caption, we do not show the tilting angle of No-ring cylinders, because it is always smaller than 5°, with a random distribution of values around the vertical direction.

Figures 6(b) and (c) are closely related, because they are two descriptions of the same process: the motion of Ring cylinders into the granular medium, that includes both sinking and tilting. The fact that at the accelerations shown in this figure the plateau in the sinking depth is barely reached while for the tilting angle it is, could be explained by the increase of the friction of the intruder with the granular medium when the tilting angle increases. Then, at $\Gamma \approx 0.75$ the intruder has approximately reached its maximum inclination, but is not completely submerged in the medium. An increase in the acceleration does not increases significantly the angle, because the resulting torque has diminished due to the influence of both sinking and tilting, but the increase in fluidization helps further sinking, until most of the cylinder is submerged, reaching the plateau.

The overall behavior in Fig. 6(a) can be understood taking into account the experimental results in Ref. [28]. When the system is submitted to lateral shaking, a "solid" layer is formed, starting at a depth h_f that depends on the adimensional acceleration Γ. For accelerations in the range we used, h_f varies almost linearly with Γ (see Fig. 3(a) in Ref. [28]), so we can write

$$h_f(\Gamma) = \alpha(\Gamma - \Gamma^*); \Gamma > \Gamma^* \qquad (1)$$

where Γ^* is the onset of fluidization and α is the slope of the linear dependence. If $\Gamma \leq \Gamma^*$ the depth of the fluidized layer is zero.

According to reference [33], Γ^* can be taken as proportional to the friction coefficient μ between the cylinder and the granular medium. So in this experiments we can approximate $\mu \approx 0.3$, that is the value we use for the simulations. They also conclude that the final depth of intrusion depends on isostasy, and on the severity of shaking. It can be entirely determined by isostasy, when the shaking completely unjams the medium and suppresses the average friction around the intruder.

Then, at low values of Γ the granular media is not fluidized, and the cylinder almost does not sink (merely 5 mm at $\Gamma = 0.27$; see Fig. 6(a)). At accelerations above the fluidization threshold, the cylinder sinks until it gets in contact with the solid layer. The larger is the acceleration, the deeper is that layer, so the bigger is Δh. But as soon as the solid layer appears at a depth larger than the cylinder's height, it does not sink further: instead, it "floats" due to isodensity with the sand, so a plateau is reached.

The strong differences in the dynamics of No-ring and Ring cylinders within the adimensional acceleration range $0.3 \leq \Gamma \leq 1.3$ can be rationalized qualitatively as follows. The bottom of the cylinders with no ring offers small tangential friction to the sand surface during the first moments of the fluidization process (when they are on top of the granular surface), which implies a small torque between the horizontal friction at the bottom and the horizontal inertial force that can be represented at the center of mass of the cylinder. So, the cylinder keeps its vertical position since the beginning of the process,

and just sinks vertically into the sand due to the action of gravity.

Differently from No-ring cylinders, the basement of a Ring one is firmly settled in the granular material, so, when an acceleration is imposed by the shaker, a significant torque appears, arising from the force exerted by the sand on the ring, and the inertial force at the cylinder's center of mass, forcing it to tilt. Moreover, the presence of the ring prevents the free flow of sand near the bottom of the cylinder, which makes more difficult its vertical sinking: as the sink time increases, the torque caused by horizontal forces has "better possibilities" to tilt the cylinder.

Two additional factors influence the sinking dynamics of this type of intruder: firstly, the tilting process changes the effective size of the cylinder, changing the drag and hydrostatic forces (in a way that will be analyzed below), which contributes to a Brazil nut like effect: isodense large particles tend to rise during shaking. Additionally, when the inclination is high, most of the cylinder could be inside the sand, and it starts to float, preventing further tilting.

Comparing figures 6 (a) and (b) it is possible to see that when the cylinder tilts it reaches a smaller final depth that when it sinks without tilting, for similar adimensional accelerations. It supports the idea that the inclination of the body increases the resistance forces acting on it.

Figure 7(a) reports the time interval needed by No-ring cylinders to penetrate into the granular material, from the moment when the vibration was turned ON, until they find their new equilibrium position. If we compare this figure with figure 6(a), a main difference can be appreciated: the plateau is now reached at a higher acceleration. Anyway, both the sinking depth and sinking times increase monotonically with the increase of Γ and saturate for accelerations at which the cylinder is eventually completely immersed in the material.

Figure 7(b) shows a different tendency: the Ring cylinders tilt very fast, reaching a final inclination long before the final depth of the No-ring ones is reached. A careful inspection of the videos shows that No-ring cylinders sink fast during the first few seconds, but dramatically slow down during the penetration of the last millimeters, resulting in long sinking times. On the other hand, when Ring cylinders end the tilting process, they do not significantly sink further, perhaps due to the increase of the friction and buoyancy. That is why we do not show the sinking times of Ring cylinders: they are almost equal to the times shown in Fig. 7(b).

When we compare this figure with Fig. 6(c), an important difference is easily appreciated: though the tilt angle increases monotonically with Γ, the tilt times increase abruptly, and then saturate. That behavior could be related with the fact that, for small accelerations, the tilting process occurs slowly, but the tilting angle is small.

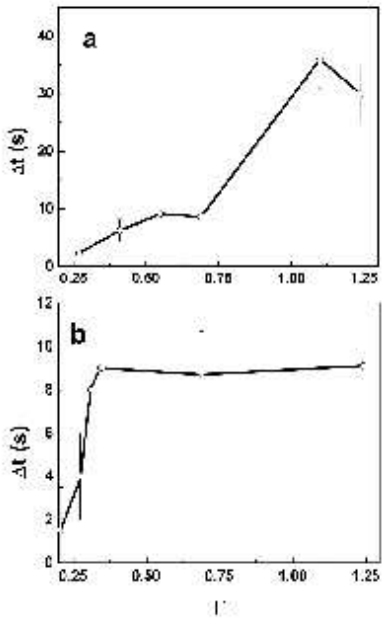

FIG. 7. Sinking times for No-ring cylinders (a) and tilting times for Ring cylinders (b). Sinking times for Ring cylinders are almost equal to their tilting times, so they are not shown.

By contrast, for bigger accelerations the tilting angle is larger, but the tilt occurs at bigger angular velocities, giving almost constant tilting times ($\Delta t = \theta/\omega$).

A phenomenological Newtonian model

In order to formulate a model to describe analytically the sinking process, let us consider the forces acting on the cylinder. As soon as the shaking starts, if the adimensional acceleration is above the threshold, the upper part of the granular bed is fluidized, and the intruder sinks.

Let us assume that the cylinder just sinks vertically, and let us name the vertical downward axis as z. The force balance on the intruder can be written as

$$m\vec{a} = m\vec{g} + \int (-P)\hat{n}dS + \int \sigma_s \cdot \hat{n}dS \qquad (2)$$

where P is the pressure, σ_s the shear stress tensor, $\hat{n}$ is the vector normal to the intruder's surface, and the integrals run over the boundary of the intruder that is inside

the granular material. Assuming a hydrostatic pressure profile, we can write:

$$P = \int_0^h \rho(z')g dz' \tag{3}$$

where h, as previously, is the depth reached by the cylinder below the surface of the granular medium. In Eq. (3) we have made explicit that the density of the material varies with depth. Let us assume that it varies as a power law between zero and the density of the solid layer, ρ_{sl}, that is reached at a depth h_f:

$$\rho(z') = \rho_{sl}\left(\frac{z'}{h_f}\right)^p \tag{4}$$

where $p \in [0, 1]$.

By combining (4) and (3) and integrating, we find the hydrostatic buoyancy force acting on the cylinder with a length h under the (average) level of the granular bed, as:

$$\int (-P)\hat{n}dS = -\frac{\rho_{sl}Sg}{(p+1)h_f^p} h^{p+1}\hat{h} \tag{5}$$

where S is the characteristic area of the intruder crossection, and $\hat{h}$ is a unit vector pointing downwards. It is easy to see that the buoyancy force depends on the volume submerged into the granular medium.

Assuming that inertial forces can be neglected, the shear stress component goes as

$$\int \sigma_s \cdot \hat{n}dS = -D\gamma v\hat{h} \tag{6}$$

where γ has the dimensions of a viscosity, D is the characteristic size of the cross section of the intruder, v is its sinking speed and $\hat{h}$ is the unit vector pointing downwards [34, 35]. By substituting Eq. (5) and Eq. (6) into Eq. (2), and only recovering the modular values, we get:

$$m\frac{d^2h}{dt^2} + D\gamma\frac{dh}{dt} + \frac{\rho_{sl}Sg}{(p+1)h_f^p} h^{p+1} = mg \tag{7}$$

Before solving Eq. (7) we will assume that the sink velocity is constant, which follows quite well the behavior during the fast sink regime, as seen in Fig. 8 (*i.e.*, we neglect the inertial term). So,

$$\frac{dh}{dt} + \frac{\rho_{sl}Sg}{D\gamma(p+1)h_f^p} h^{p+1} = \frac{mg}{D\gamma} \tag{8}$$

which can be written as

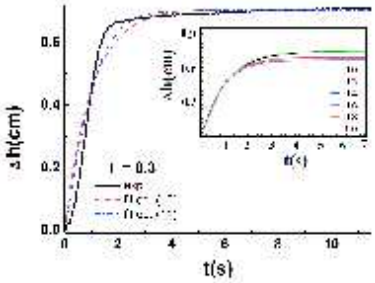

FIG. 8. (color online) Time dependence of sinking depth for the No-ring cylinder from experiment, compared with that determined from Eqs. (10, 11). The inset shows the solutions of Eq. (7) for different values of p (see text).

$$\frac{dh}{dt} + ah^{p+1} = b \tag{9}$$

The definitions of a and b are easily deduced comparing Eqs. (8) and (9).

Equation (9) has analytical solutions if $p = 0$ or $p = 1$, which correspond to the extreme cases of constant density and a linear density profile with depth, respectively. The solutions are

$$h(t) = \frac{b}{a}(1 - e^{-at}) \tag{10}$$

if $p = 0$, and

$$h(t) = \sqrt{\frac{b}{a}}\tanh(\sqrt{ab}t) \tag{11}$$

if $p = 1$.

It is easy to see that both expressions correspond to an exponential growth that saturates.

Figure 8 shows the experimental results (continuous line) obtained for an adimensional acceleration $\Gamma \simeq 0.3$. It is possible to see in more detail the initial fast sinking process, followed by the slow creep. Fig. 8 also shows the fitting of equations (10,11) to experimental data. Even the simplified Eq. (10) reproduces well the main features of the sinking process.

It is almost impossible to determine experimentally the exact density profile. But we do not need to know it in order to validate our model, if we use the following rationale. Firstly, we fit Eqs. (10,11) to the experimental data and obtain the values of a, b that correspond to $p = 0$ ($a(p = 0), b(p = 0)$) and $p = 1$ ($a(p = 1), b(p = 1)$). Let us assume that a and b vary linearly with p between

the extremes values which were obtained from the fitting process. For an intermediate value of p (say, p_1) we can calculate the corresponding values of $a(p_1)$ and $b(p_1)$. With them, we can in turn determine the constants of Eq. (7). Then, we solve this equation numerically. This procedure is repeated for values of p between 0 and 1, with a step of 0.1.

The inset in Fig. 8 shows some of the numerical solutions for the values of p in the legend. The main conclusion is that the density profile has small influence on the first (and most important) part of the sinking process. Of course, the final depth is influenced by the value of p, but due to experimental uncertainties, it is almost impossible to choose any particular value.

Let us now study the influence of the values of p in the quality of the fit of the solution of Eq. (7) to the experimental data. For doing this we note that the values of a and b in Eq. (10) can be easily obtained from the experiments. Considering Eq. (9) in the first moments of motion, as h is small, $h'(t) \simeq b$, so b can be evaluated as the initial slope. As at large times $h(t) \sim h_{eq}$ ($h_{eq} = \Delta h$ if $h(0) = 0$) then $a = b/h_{eq}^{p+1}$. Then solving (7) for a given value of $b, p, a(p)$ and naming the result h_{mod}, the best value of p arises from the minimization:

$$min \sum_{i=1}^{N} (h_{mod}(t,p) - h_{exp}(t))^2 \qquad (12)$$

where $h_{exp}(t)$ are the experimental values of h.

The result for $\Gamma \leq 1.0$ is indifferent to p: the fit is equally good no matter which is the value of $p \in [0,1]$. For $\Gamma = 1.24$ there are differences in the quality of fits for different p, but Eq. (12) gives a minimum for $p = 0$, so, we will assume $p = 0$ in the following. Then, Eq. (7) becomes:

$$m\frac{d^2h}{dt^2} + D\gamma\frac{dh}{dt} + \frac{\rho_{sl}Sg}{h_f}h = mg \qquad (13)$$

that can be taken as the simplest equation of motion that describes the vertical sink dynamics of our cylinders. It is worth noticing that (13) reproduces quite closely the results reported in Fig. 8, and can be used to explain the vertical sinking of Ring-cylinders while tilting, as we will see below.

Before that, it is instructive to compare equation (13) for a granular bed fluidized by shaking, with that proposed in [18] to describe the penetration of an intruder into ultra-light granular material that eventually behaves like a fluid medium even in the absence of shaking. The equation proposed in [18] reads as:

$$m\frac{d^2h}{dt^2} = mg - \eta\left(\frac{dh}{dt}\right)^2 - \kappa\lambda\left(1 - e^{-\frac{h}{\lambda}}\right) \qquad (14)$$

Firstly we will analyze the last term of Eq. (14) which is related to Janssen's pressure. If we were applying this equation to our system, we should have taken into account that the shaking promotes the destruction of the force chains. That is equivalent to assume a very big λ, which yields a pressure force of the form $\kappa\lambda(z/\lambda) = \kappa z$, as proposed earlier in [16]. Comparing with Eq. (13) we see that the depth-dependent terms in both equations are similar, provided that

$$\kappa = \frac{\rho_{sl}S}{h_f}g \qquad (15)$$

(notice that the linear relation of κ with g has been demonstrated experimentally in [24]).

However, there is an important difference in the "viscous drag" terms between equations (13) and (14): in the first, the velocity is linear, while it is squared in the second. Indeed, we cannot reproduce our experimental sink process if we insert in Eq. (13) a squared velocity term. However, the difference can be justified by the fact that the sink velocities in our shaken-bed experiment are much smaller than those observed in the penetration experiments reported in [18] and [24].

Now we concentrate again in the interpretation of our experimental results. In order to understand the tilting dynamics, it is useful to note that, when applying Eq. (13) to a tilted cylinder, the values of both D and S change. The reason is that when we calculate the surface integral, the result will be proportional to the cylinder's immersed volume. As the cylinder tilts, the immersed surface increases more than in the case of sinking without tilting, so the drag force is bigger in the former case. Considering, for instance, the situation represented in the lower row of Fig. 2, when the cylinder sinks a distance Δh, the surface increases as the inverse of $\cos\theta$ (of course, other intruder geometries may follow different laws).

To test it, let us assume a simplified model: the increase factor of S and D is proportional to the characteristic size of the cross section of the cylinder projected on the horizontal plane, i.e., it is proportional to the inverse of $\cos\theta$. Then, instead of D and S, we will solve Eq. (13) using $D/\cos\theta(t)$ and $S/\cos\theta(t)$, where $\theta(t)$ is a function that grows from zero to the maximum angle reached by the cylinder, mimicking Fig. 5(c).

The consequences can be seen in Fig. 9. While in the beginning the sinking process in all situations occurs with the same dynamics, as the cylinder approaches the final angle, the behavior changes, been the final depth larger for the situations corresponding to low tilting.

The upper curve, calculated for θ =0 coincides with the upper curve in the inset of Fig. 8 (calculated for $p = 0$). Subsequent curves are calculated for values of θ varying in steps of $\pi/15$, the lowermost curve corresponds to $\theta = \pi/3$. As the inclination of the cylinder increases, both the buoyancy and the viscous drag do. The effect of

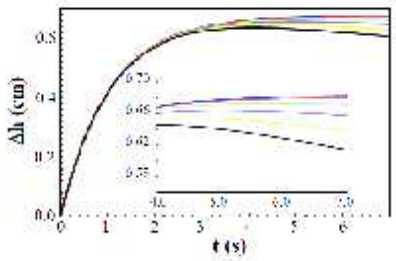

FIG. 9. (color online) Time dependence of sinking depth as calculated solving numerically Eq. (13) considering the variation of S and D provoked by tilting (see text). Upper curve is for $\theta = 0$ while the lower one is for $\theta = \pi/3$. Between them, θ varies in steps of $\pi/15$. The inset shows the last three seconds.

these factors on the sinking process of Ring cylinders was already noted in Fig. 5(b): an immediate consequence is the decrease of the sinking depth (for a given Γ), compared with that of the No-ring ones, which can be easily observed in the experiments. In the inset it is possible to deduce that, for the larger angles, a small decrease in the depth is observed, suggesting the influence of a Brazil nuts like effect.

In spite of the simplifications assumed, it is worth noting that the basic differences between Fig. 6 (a) and (b) are reproduced by our model.

Finally, there is another element that was also not considered in our model: as the container shakes horizontally, it is equivalent to a horizontal drag that changes periodically its direction. According to [36], it creates an additional lift force, and also a dependence of the drag force with depth, which, of course, must influence the detailed penetration dynamics of the Ring cylinders.

Quasi-2D numerical simulations

In figure 10 we can see the behavior of the quasi-2D No-ring intruder for three different adimensional accelerations. The same accelerations have been applied to a medium containing the simulated Ring intruder, see Fig. 11.

Regarding the vertical sinking, we do not observe major changes between Ring and No-ring intruders. We can notice that they sink less than in the experiments, which may be related with the dimensionality of the simulation relative to the real experiment. Quasi-2D granular media allow less choices of readjustment than in 3D: they are easily jammed, which makes it more difficult for an object to sink. Moreover, the size ratio of the intruder over the particles is 15 times smaller in the simulations than in the experiments (experiments: 44mm/0.280mm = 150; simulations: 40mm/4mm = 10), which means that if one

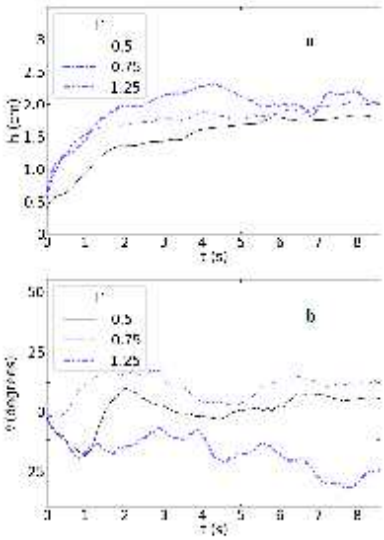

FIG. 10. (color online) Time dependence of sinking depth (a) and tilting angle (b) for a simulated 2D No-ring cylinder.

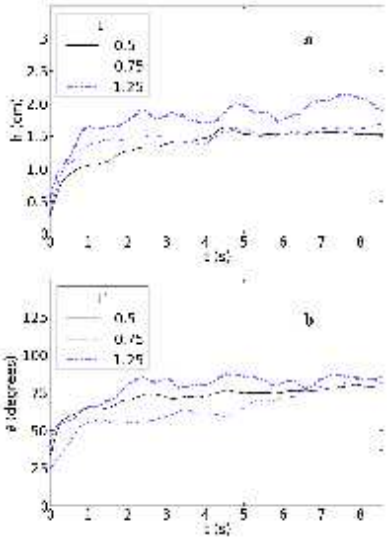

FIG. 11. (color online) Time dependence of sinking depth (a) and tilting angle (b) for a simulated quasi-2D Ring cylinder.

particle is stuck under the intruder during the simulations, it will slow down the intruder significantly more than if the particle were 15 times smaller. In addition, since the numerical intruder is made out of particles of the same size as the particles of the medium, it may be rougher that the experimental intruder.

For the tilting, we find that the presence of foundation at the bottom of the intruder causes a large tilting. Indeed, for the shaking with No-ring, the intruder tilting angle is a few tens of degrees, but during the shaking with ring, the intruder tilts fast, reaching a angle between 80 and 90°(see Fig. 4): the intruder almost ends up lying on one of its sides.

An interesting result of the simulations is seen in figure 10 (a): while for the smaller accelerations the tilting angle of the No-ring cylinders oscillate around 0°, for the adimensional acceleration $\Gamma = 1.25$ the No-ring cylinder reaches an angle of approximately 25°. It suggests that, for big enough accelerations, it is possible to tilt the cylinder, independently of the details of its foundation. Some preliminary experimental results obtained by us using higher frequencies of shaking (which gives higher adimensional accelerations) does confirm that finding.

Conclusions

In this paper, we have studied the behavior of cylindrical objects as they sink into a dry granular bed fluidized by horizontal oscillations, as a model system to understand the effects of earthquake-related fluidization of soils on human constructions and other objects like rocks.

We have found that, within a relatively large range of lateral shaking amplitudes at a frequency of 5 Hz, cylinders with flat bottoms sink vertically, while those with a "foundation"consisting in a shallow ring attached to their bottom, tilt laterally besides vertically sink. The tilting is associated to the torque experienced by the cylinder when the ring at the bottom increases the friction with the laterally-accelerated granular bed.

We have been able to mimic the above described behaviors by quasi-2D numerical simulations. We have also reproduced the vertical sink dynamics of cylinders with a flat base using a Newtonian equation of motion for an object penetrating a fluidized layer of granular matter, where the granular effective density increases with depth, eventually reaching a solid phase. The same model allows to understand the sinking even in the present of tilting.

Finally, it is worth noting that preliminary experimental data and quasi-2D numerical simulations suggest that, when strong enough lateral shaking is applied, the tilting scenario tends to dominate regardless the nature of the intruder's foundation.

ACKNOWLEDGEMENTS

We acknowledge support from Project 29942WL (Fonds de Solidarité Prioritaire France-Cuba), from the EU ITN FlowTrans, and from the Alsatian network REALISE. E. A. drew inspiration from the late M. Álvarez-Ponte.

[1] J. D. Bray and J. P. Stewart "Damage patterns and foundation performance in Adapazari, in Kocalei, Turkey earthquake of August 17, 1999". Reconnaisance Report, Earthquake Spectra **16** (Suppl. A), 163-189 (2000).
[2] R. B. Sancio, J. D. Bray, J. P. Stewart, T. L. You, H. T. Durgunoglu, A. Onalp, R. B. Seed, C. Christensen, M. B. Baturay and T. Karadayilar, *Soil Dyn. Earthquake Engng.* **22**, 1093-1102 (2002).
[3] R. B. Sancio, J. D. Bray, T. Durgunoglu and A. Onalp. Proc. 13th Conference in Earthquake Engineering, Vancouver, B.C., Canada (August 1-6, 2004), Paper No. 935.
[4] N. N. Ambraseys, Engineering seismology, Special Issue-the 1987 Mallet-Milne lecture. *J. Earthq. Eng. Struct. Dyn.* **17**, 1-105 (1988).
[5] National Research Council, "Liquefaction of Soils During Earthquakes", (National Academy Press, Washington, DC, 1985).
[6] J. B. Berril and R. O. Davis, *Soils Found.* **25**, 106118 (1985).
[7] E. Clément and J. Rajchenbach, *Europhys. Lett.* **16**, 133 (1991).
[8] C. Y. Wang and M. Manga, "Earthquakes and Water" (Springer, Berlin, Heidelberg, 2014).
[9] H. Jaeger, S. Nagel and R. Beringer, *Rev. Mod. Phys.* **68**, 1259 (1996).
[10] T. Shinbrot and F. N. Muzzio, *Phys. Rev. Lett.* **81**, 4365-4368 (1998).
[11] E. Altshuler, O. Ramos, E. Martínez, A. J. Batista-Leyva, A. Rivera and K. E. Bassler *Phys. Rev. Lett.* **91**, 014501 (2003).
[12] I. S. Aranson and L. S. Tsimring *Rev. Mod. Phys.* **78**, 641 (2006).
[13] B. Andreotti, Y. Forterre and O. Pouliquen, "Granular matter: between fluid and solid" (Cambridge University Press, Cambridge, 2013).
[14] J.S. Uehara, M.A. Ambroso, R.P. Ojha, and D.J. Durian, *Phys. Rev. Lett.* **90**, 194301 (2003).
[15] J.F. Boudet, Y. Amarouchene, and H. Kellay, *Phys. Rev. Lett.* **96**, 158001 (2006).
[16] H. Katsuragi and D. Durian, *Nat. Phys.* **3**, 420 (2007).
[17] D.I. Goldman and P. Umbanhowar, *Phys. Rev. E* **77**, 021308 (2008).
[18] F. Pacheco-Vázquez, G.A. Caballero-Robledo, J.M. Solano-Altamirano, E. Altshuler, A.J.Batista-Leyva and J.C. Ruiz-Suárez, *Phys. Rev. Lett.* **106**, 218001 (2011).
[19] L. Kondic, X. Fang, W. Losert, C.S. O'Hern, and R.P. Behringer, *Phys. Rev. E* **85**, 011305 (2011).
[20] H. Torres, A. González, G. Sánchez-Colina, J. C. Drake and E. Altshuler, *Rev. Cub. Fis.* **29**. 1E45 (2012).
[21] A. H. Clark and R. P. Behringer, *Europhys. Lett.* **101**, 4001 (2013).

[22] J.C. Ruiz-Suárez, *Rep. Prog. Phys.* **76**, 066601 (2013).
[23] T. A. Brzinski III, P. Mayor, and D.J. Durian, arXiv: 1307.4638 [cond-mat.soft] (2013).
[24] E. Altshuler, H. Torres, A. González-Pita, G. Sánchez-Colina, C. Péres-Penichet, S. Waitukaitis and R. C. Hidalgo, *Geophy. Res. Lett.* **41**, 3032 (2014).
[25] S. Joubaud, T. Homan, Y. Gasteuil, D. Lohse and D. van del Meer, *Phys. Rev. E* **90**, 060201(R) (2014).
[26] G. Metcalfe, S. G. K. Tennakoon, L. Kondic, D. G. Shaeffer, and R. P. Behringer *Phys. Rev. E* **65**, 031302 (2002).
[27] Ch. A. Kruelle *Rev. Adv. Mater. Sci.* **20**, 113 (2009).
[28] S. G. K. Tennakoon, L. Kondic, RP Behrenger. *Europhys. Lett.* **45(4)**, 470 (1999).
[29] H. Liu and R. Dobry, *J. Geotechnical and Geoenvironmental Engng.* **123**, 557-567 (1997).
[30] G. Sánchez-Colina, L. Alonso-Llanes, E. Martínez, A. J. Batista-Leyva, C. Clément, C. Fliedner, R. Toussaint and E. Altshuler *Rev. Sci. Inst.* **85**,126101 (2014).
[31] P. A.Cundall and O. D. Strack. A discrete numerical model for granular assemblies. Geotechnique, Ice Virtual Library, **29**, 47-65 (1979).
[32] See EPAPS Document No. [number will be inserted by publisher] two watch two videos that display the sinking and tilting processes.
[33] R. Toussaint, C Clément, C Fliedner, M. Stojanova, E. Aharonov, G. Sanchez, E. Altshuler, A. Batista and E. G. Flekkoy, *Geophysical Research Abstracts* **16** EGU2014, 12539, (2014).
[34] J. R. de Bruyn and A. M. Walsh,*Can. J. Phys.* **82**, 439 (2004)
[35] M. Hou, Z. Peng, R. Liu, Y. Wu, Y. Tian, K. Lu, and C. K. Chan,*Sci. Tech. Adv. Mat* **6**, 855 (2005)
[36] X. Zhang, D. Sheng, G.P. Kouretzis, K. Krabbenhoft, and S. W. Sloan *Phys. Rev. E* **91**, 022204 (2015).

2.2 Supplementary information.

Our test cell is a 0.0156 m^3 (25x25x25 cm^3) acrylic cube filled to approximately 2/3 of the volume with a grains bed. It was firmly fixed to a cradle driven over sliders with 0DOF (0 degrees of freedom) by a TIRA TV51120 shaker. The shaker governs the cradle through a rigid steel shaft. Fit to the front side of the cradle a Gopro HERO-II camera is recording the experimental sequences at 120 frames per second (fps), as it is pointing to the center of the cell transversely to the movement's sense. We chose for the granular bed Ugelstad spheres of non-expanded polystyrene with a density 1.05 g/cm^3, and diameter 140 μm (monodisperse within a 1 percent).

The intruders were 44 mm height x 44 mm diameter 3D printed cylinders with 3 mm wide walls, made of alumide by Sculpteo. One of the cylinders has a flat bottom, imitating a mat foundation. The other one has a 5 mm high and 3 mm wide ring in the base as a circular strip foundation. A ballast inside the intruders make them isodense with the medium.

To warrant the loose condition on the medium, beforehand disposing the intruder on the surface, we plow with a stick along and cross the bed, deep to the bottom, until the grains present the least opposition. This step is mandatory, as the grain bed consolidates on every shaking session. Before we turn on the shaker, the camera is set to record, and then the shaker is on for around 20 s. Then backwards, first the shaker, then the recording is stopped up to set the next sequence.

The camera records the image sequences at 120 fps in MP4 format. On the front face of the intruder, a pair of black patches vertically disposed, helps to tag the body in the frame with the image processing software. A flicker-free 400 W spotlight (Dedolight HMI) illuminates the experimental setup.

2.2.2 Image processing: further details.

Each sequence must be converted from MP4 form to a JPG sequence of color images before processed. The process is done with the help of MatlabR2014a. The task to translate to images is carried out with the FFMPEG software. The resulting image sequences are the input to a Matlab script that in general follows always the same algorithm, loading the frame, crop the image to keep the zone were the intruder will move along the frames, which reduces the pixels to process. The image is converted to gray scale and then filtered to homogenize the

bright levels and then converted again to black and white (BW) taking a standard contrast level as a gray value binarization reference. The BW image is filtered again to isolate the black patches. The patches are the references to identify the center of mass and, consequently, the position of the intruder. At the same time, they trace a central line that traces the angular position giving us the angle and position change from frame to frame. The data returned in workspace variables is saved in a file after every session to be processed in a calculation sheet.

In some experiments the sloshing sand or reflects or glows in the cell surface spoils the images, then is necessary to apply more filtering or even to discard the patches as references. By instance, on the experiments that finish in a toppling cylinder, usually the patches goes into the grains surface. On these cases, the edges of the cylinder helps to track the position. This means that to program the script, we must inspect the video before, to assess if there are blurring of the image, if the marks are always visible, and if possible, to cut out useless frames to speed out the process. Some frames are much damaged when various sources of error combines, on these cases there is still the resource to measure the initial and final position of the intruder with another image process software, as ImageJ.

Figure 2.1 shows a block diagram of the image processing algorithm, which was implemented in Matlab. The corresponding script is explained below.

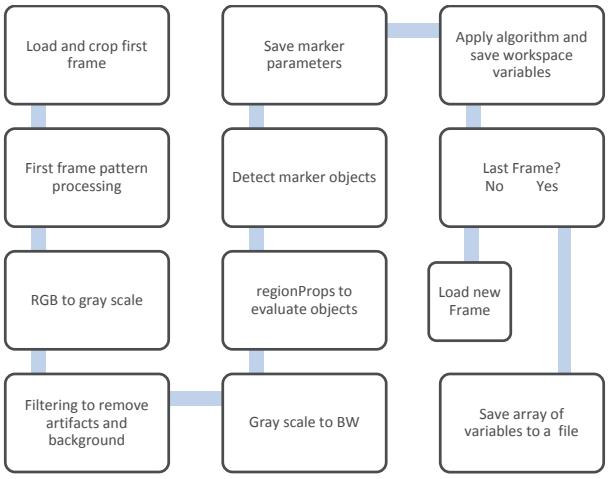

Figure 2.1 Block diagram of the Matlab's image processing algorithm.

The diagram on the figure shows the normal procedure carried out to calculate the position of the intruder's center of mass position through the sequence of frames originated from the recorded experiment (see figure 2.2.2).

The first operation is to load the sequence into the Matlab's work space:

```
close all
clear all

filFolder = 'C:\Users\Owner\Documents\MATLAB\Nr5Hz300c\';
filePattern = dir(fullfile(filFolder,'noring_5Hz_300mV_c-*.jpg'));
filNames = {filePattern.name}';        %Trasposing the pixels array
cfilNames = filNames;
nFrames = numel(filNames);
%Customized threshold and areas
% nr5Hz300a gray - BW threshold 0.47
% nr5Hz300b gray - BW threshold 0.44
% nr5Hz200d gray - BW threshold 0.45 Area cn>130
% nr5Hz200b gray - BW threshold 0.47 Area cn>120
% noring_5Hz_300mV_c gray - BW threshold 0.47 cn>130
% noring_5Hz_400mV_a gray - BW threshold 0.5 cn> 80
Angle = 90; %Parameter to calculate angle

for p = 1:nFrames
rgb = imread(filNames{p});              %JPG frame to RGB
```

Next to loaded the images sequence, is to crop it to speed up the process avoiding to process pixels without useful information.The first frame is pre-processed to determine the position parameters of the intruder and the marks (shown as dark spots in Fig. 2.2). These parameters will be used as initial settings to process the subsequent frames, as follows:

```
%Cropping coordinates (was done by just tampering on the first frame ...
                                                    %for each sequence)
start_row = 50;%Works for all
start_col = 300;
% Crop the Image to save processing time
rgbcrop = rgb(start_row:300, start_col:700, :);
                                            %  figure, imshow(rgbcrop);
```

```
Igr = rgb2gray(rgbcrop);                    %Convert to grayscale

L_HH = stretchlim(Igr);       %Enhancing the contrast, see Matlab's example
Ig = imadjust(Igr,L_HH,[]);

dim = size(Ig);                              %Take the n of col and rows
cn = 120;                            %Area, parameter for the mark to detect
                                         %it will change along the execution
                                             %of the algorithm
ix1 = 1;                              %Reset the order number for
ix2 = 2;                                     %the detected areas

%%%%%%%%%%%%%%%%%%%%%%%%%%%%%%%%%%%%%%%%%%%%%%%%%%%%%%%%%%%%%%%%%%%%%%%%%%%%%%%
%Clearing the background
Ibw = im2bw(Ig, 0.47);                 %starting threshold for the sequence
if Angle < 80                          %Adjust the threshold for shadows
    Ibw = im2bw(Ig, 0.5);                            %on tilted images
end
                             %figure, imshow(Ibw), title('Erased bkground');
%%%%%%%%%%%%%%%%%%%%%%%%%%%%%%%%%%%%%%%%%%%%%%%%%%%%%%%%%%%%%%%%%%%%%%%%%%%%%%%
%Create mask for the marks on the intrus
 Igm = immultiply(Ig, ~Ibw);        %Isolating Marks on the grayscale image
                                %  figure, imshow(Igm), title('Raw Gris');

 Ig = imfill(~Igm,'holes');                 %Cleaning some spureous marks
                          %figure, imshow(Ig), title('Ig Mask after imfill');
%%%%%%%%%%%%%%%%%%%%%%%%%%%%%%%%%%%%%%%%%%%%%%%%%%%%%%%%%%%%%%%%%%%%%%%%%%%%%%%
%Further cleaning Marks
Marks = immultiply(Igm,Ig);
                             % figure, imshow(Marks), title('Igm xIg mask');
IM =(Marks*2);
Ibwm = im2bw(IM);
Ibxm = imfill(Ibwm,'holes');
me = [9 5];
 se = strel('Rectangle', me);%
 Ibm = imclose(Ibxm, se);
% figure, imshow(Ibm), title('Preprocessed Frame');
%%%%%%%%%%%%%%%%%%%%%%%%%%%%%%%%%%%%%%%%%%%%%%%%%%%%%%%%%%%%%%%%%%%%%%%%%%%%%%%
%Taking the first frame as a pattern
if p == 1

CC = bwconncomp(Ibm);
S = regionprops(CC, 'Area','BoundingBox','Extrema');
NE = numel(S);
L = labelmatrix(CC);
Arefs = [S.Area];
 [Ai,in]=sort(Arefs,'descend');
 cn = Ai(2)-1;                          %Sets the lower boundary for the area
[RfArea,Adx]=max(Arefs);
BW1 = ismember(L, find([S.Area] > cn));

ColLimExtr = S(Adx).Extrema(:,1)+20;%Sets the boundary to find the intrus
                                     %upper point + 20 pixels
                                  % figure, imshow(BW1), title('Region #1');
%Again regionprops to erase side shadow
%and to set the reference points in the intrus
```

```
% if p == 1                  %Just to be used to tamper in a test frame
CC0 = bwconncomp(BW1);
S0 = regionprops(CC0,'Area','Extrema');
L0 = labelmatrix(CC0);
ATops = [S0.Area];
[MaArea,Aidx]=max(ATops);
%Deleting spureous bodies to the right of the marks
BWI = ismember(L0, find(S0(Aidx).Extrema(:,1) < ColLimExtr));
                      % figure, imshow(BWI), title('Frame #1 first marks');


CC1 = bwconncomp(BWI);
S1 = regionprops(CC1, 'Area','Centroid','BoundingBox','Extrema');
L1 = labelmatrix(CC1);
Lmap = label2rgb(L1,'lines','k');

                     % figure, imshow(Lmap), title('Frame #1 second marks');
%Taking the centers of the Mark to be used as a beginning pattern
Frstcenter=S1(1).Centroid;%(col,row)
Scndcenter=S1(2).Centroid;
RefCenter = vertcat(Frstcenter,Scndcenter);

end
%%%%%%%%%%%%%%%%%%%%%%%%%%%%%%%%%%%%%%%%%%%%%%%%%%%%%%%%%%%%%%%%%%%%%%%
```

The marker is isolated from the background pixels after cropping the region of interest by means of a polygonal mask. The polygon is placed taking the coordinates from the previous frame's mask. These parameters are updated by the corresponding parameters from the regionProps structure in the region comprising the mark:

```
%Here starts the processing of the sequence
if p ~= 1
%%%%%%%%%%%%%%%%%%%%%%%%%%%%%%%%%%%%%%%%%%%%%%%%%%%%%%%%%%%%%%%%%%%%%%%
% Pick the marks by check the matching points

if RefCenter(3)> RefCenter(4)
    st = RefCenter(3);
    RefCenter(3)= RefCenter(4);
    RefCenter(4)= st;
st = RefCenter(1);
    RefCenter(1)= RefCenter(2);
    RefCenter(2)= st;
end
refCol = RefCenter(:,1)';
refRow = RefCenter(:,2)';

BW2 = bwselect(Ibm,refCol,refRow,4);
                           % figure, imshow(BW2), title('Matching Points');
CC1 = bwconncomp(BW2);                  %Reuse CC1 to spend memory space
S1 = regionprops(CC1, 'Area','Centroid','BoundingBox');
```

```
Nl = numel(S1);
if Nl~=2              %If one of the marks isn't detected expand the search
    ci = refCol(1) -30;
    cd = refCol(2) +30;
    ru = refRow(1) -20;
    rl = refRow(2) +20;
c = [ci ci cd cd];
r = [ru rl rl ru];
MBW = poly2mask(c,r,dim(1),dim(2));
                                    % figure, imshow(MBW),title('Mask 2');
BW2 = immultiply(Ibm,MBW);
%                               figure, imshow(BW2),title('New centers');
CC1 = bwconncomp(BW2);
S1 = regionprops(CC1, 'Area','Centroid','BoundingBox');
Nf = numel(S1);
end
L1 = labelmatrix(CC1);
Lmap = label2rgb(L1,'lines','k');
Arnw = [S1.Area];
 [An,in]=sort(Arnw,'descend');
  ix1 = in(1);                                %Sort the areas
   ix2 = in(2);
                        % figure, imshow(Lmap), title('N processed Frame');

% hold on;
end

Frstcenter=S1(ix1).Centroid;                                    %(col,row)
Scndcenter=S1(ix2).Centroid;

Center = vertcat(Frstcenter,Scndcenter);
```

The Mark is identified amid of the objects as the one with the biggest area:

```
if p ==1
    RefCenter = Center;
%     break;

else
    DfCenter = RefCenter - Center;
    RefCenter = Center;
end


%%%%%%%%%%%%%%%%%%%%%%%%%%%%%%%%%%%%%%%%%%%%%%%%%%%%%%%%%%%%%%%%%%%%%%%%%%%
% Finding line  between centers to calculate angle

linvec = polyfit(Center(:,1),Center(:,2),1);%polyfit(x,y,n)
% linx = [0 dim(1)];
% Pendientes(p,1)= linvec(1);
```

```
%    Hallar angulo
if Center(1)== Center(2)
    Ang = 90;
%     AngI = 90;
else
    vect1 = [1 linvec(1)]; % create a vector based on the line equation
    vect2 = [1 0];
    dp = dot(vect1, vect2);

    % compute vector lengths
    length1 = sqrt(sum(vect1.^2));
    length2 = sqrt(sum(vect2.^2));
    A =(acos(dp/(length1*length2))*180/pi);
    % obtain the larger angle of intersection in degrees
    if linvec(1)< 0
        Ang =  acos(dp/(length1*length2))*180/pi;
%           AngI = 180 - atand(linvec(1));                    %Doesn't works
    else
        Ang = (acos(dp/(length1*length2))*180/pi);
            AngI =  atand(linvec(1));
    end
end
```

After extracting the X-Y coordinates of the mark over the complete sequence of images, and the inclination based on the X-Y coordinates of both marks, those parameters are exported, from the Workspace to a txt file:

```
Angle(p,1) = (Ang);  %Angles including the first frame
% Angle(p,1) = (AngI);
ROW(p,1)= (Center(1));
COL(p,1) = (Center(3));
YXA = horzcat(ROW,COL);
YXA = horzcat(YXA,Angle);%incorporate all the vectors to the array
end
%Run this function in the command window to save a file
% save('Nr5Hz30Oc.txt', 'YXA','-ascii','-tabs');
```

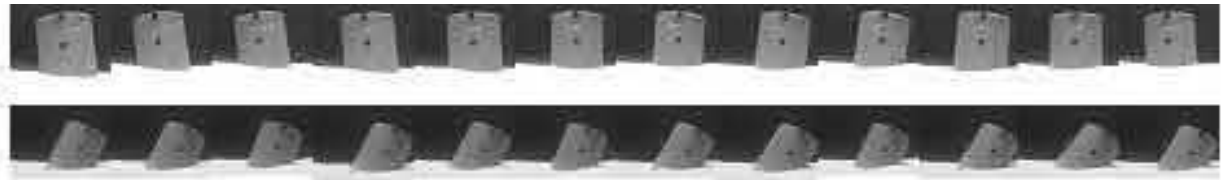

Figure 2.2 Sequence of images, top row, oscillating, bottom row, tilting to the right.

2.2.3 Fluidization and structural damage.

Structural damage and fluidization in real buildings are linked complex ways. For example, modern buildings in Adazapari, Turkey, were mostly 3 to 6 story reinforced concrete structures with firm reinforced concrete mat foundations. After undergoing ground failures, many structures moved without substantial structural damage (Bray & Dashti, 2010). Many of the structures settled into the soil without tilt.

Tilting of structures after the earthquake without significant physical damage was attributed to the behavior of these foundations, which allows the building to respond more as a rigid body while it undergoes significant differential downward movement, tilt, or lateral translation. Tilt or toppling was related in many buildings to be laterally unconstrained with high aspect ratios (Sancio, Bray, & als., 2004). This effect had been observed before in the 1964 Niigata and 1990 Luzon earthquakes, typically in corner buildings, in buildings without adjacent structures on one or both sides, in buildings surrounded by lightweight structures, and in those parts of the area where there was greater separation between adjacent buildings (Liu & Dobry, 1997).

The structural damage was more significant for buildings with individual footing allowing differential settlements. New buildings with continuous and mat foundations settled and/or tilted as a whole, with little damage to the superstructure (Liu & Dobry, 1997). All of these observations pointed to the importance of the confining effect of the whole building and adjacent structures in reducing the level of settlement. In current design practice, a liquefiable soil deposit would be treated before a new structure is built on it. In fact, it is a well-established fact that there is a relationship between parameters as the width of the foundation, the thickness of the liquefied layer, and the foundation contact pressure, to displacements of foundations on granular soils. In model tests, it has been found that the vertical foundation movement is inversely proportional to the foundation width. (Liu & Dobry, 1997).

However, a building settlement is also affected by a large number of other variables that cannot be independently assessed. Hence, the development of engineering tools for evaluating the consequences of liquefaction on building performance warrants more attention. Perhaps the experiments previously described in this chapter may help to establish a laboratory framework

to determine the effect of each individual feature of a building's foundation when the soil is fluidized.

In fact, the experiments reported in the present chapter study a variable usually overlooked in the study of the behavior of the building stressed by a seism: the shape of the foundation.

Architecture establishes a diversity of foundations, grouped under the shallow or depth foundation classifications. Shallow foundations are by large the most used for household buildings, because they are technologically easy and affordable –it is perhaps reasonable to identify them with the flat-bottom cylinders studied earlier in the present chapter. Shallow foundations are also the most affected by soil fluidization in earthquakes. With this motivation, we headed the experiments to study the mat or raft foundations, and the circular footing (strip, continuous spread or wall footing). Depth foundations, as pillars, usually go down to the bedrock or up to the safe zone where there is no chance of liquefaction –such foundations could be identified with the ring-shaped basement cylinders. Then, it seems reasonable as a future research track to make a careful survey of sink and tilt effects of earthquakes on real buildings with shallow and depth foundations, and compare them with the laboratory results reported earlier in the present chapter.

Chapter 3 Settling into dry granular media in different gravities.

3.1 Article: E. Altshuler, H. Torres, A. González-Pita, G. Sánchez-Colina, C. Pérez-Penichet, S. Waitukaitis and R. C. Hidalgo, Geophysical Research Letters 41, 3032 (2014).

AGU PUBLICATIONS

Geophysical Research Letters

RESEARCH LETTER
10.1002/2014GL059229

Key Points:
- The settling depth in granular media is independent of gravity
- The settling time scales like $g^{-1/2}$
- Layering driven by granular sedimentation should be similar

Supporting Information:
- Readme
- Text S1

Correspondence to:
E. Altshuler,
ealtshuler@fisica.uh.cu

Citation:
Altshuler, E., H. Torres, A. González-Pita, G. Sánchez-Colina, C. Pérez-Penichet, S. Waitukaitis, and R. C. Hidalgo (2014), Settling into dry granular media in different gravities, *Geophys. Res. Lett.*, *41*, 3032–3037, doi:10.1002/2014GL059229.

Received 7 JAN 2014
Accepted 10 APR 2014
Accepted article online 14 APR 2014
Published online 1 MAY 2014

Settling into dry granular media in different gravities

E. Altshuler[1], H. Torres[1], A. González-Pita[1], G. Sánchez-Colina[1], C. Pérez-Penichet[1], S. Waitukaitis[2], and R. C. Hidalgo[3]

[1]"Henri Poincaré" Group of Complex Systems, Physics Faculty, University of Havana, Havana, Cuba, [2]Department of Physics, James Franck Institute, University of Chicago, Chicago, Illinois, USA, [3]Department of Physics and Applied Mathematics, University of Navarra, Pamplona, Spain

Abstract While the penetration of objects into granular media is well-studied, there is little understanding of how objects settle in gravities, g_{eff}, different from that of Earth—a scenario potentially relevant to the geomorphology of planets and asteroids and also to their exploration using man-made devices. By conducting experiments in an accelerating frame, we explore g_{eff} ranging from 0.4 g to 1.2 g. Surprisingly, we find that the rest depth is independent of g_{eff} and also that the time required for the object to come to rest scales like $g_{eff}^{-1/2}$. With discrete element modeling simulations, we reproduce the experimental results and extend the range of g_{eff} to objects as small as asteroids and as large as Jupiter. Our results shed light on the initial stage of sedimentation into dry granular media across a range of celestial bodies and also have implications for the design of man-made, extraterrestrial vehicles and structures.

A loosely packed bed of sand sits precariously on the fence between mechanically stable and flowing states. This has especially strong implications not only for the geomorphology of the Earth but for that of extraterrestrial bodies where the surface is predominantly granular [*Shinbrot et al.*, 2004; *Almeida et al.*, 2008; *Thomas and Robinson*, 2005; *Asphaug*, 2007; *Miyamoto et al.*, 2007]. Beyond surface morphology, extraterrestrial exploration and development requires navigation in and on loose granular media, but little is known regarding how objects settle in granular systems with gravitational conditions different from Earth's. Such understanding may have helped prevent the difficulties encountered by the Mars rover, Spirit, as it sank into and tried to escape from a sand dune in 2009 (see, for example, http://marsrover.nasa.gov/spotlight/20091019a.html). Other endeavors, such as asteroid or lunar mining [*Elvis*, 2012], will certainly involve both navigation and construction on granular surfaces.

During the last decade, our understanding of the resistance to objects penetrating into granular media under Earth-like conditions has advanced quickly [*Uehara et al.*, 2003; *Walsh et al.*, 2003; *Boudet et al.*, 2006; *de Vet and de Bruyn*, 2007; *Katsuragi and Durian*, 2007; *Pacheco-Vázquez et al.*, 2011; *Katsuragi*, 2012; *Kondic et al.*, 2012; *Ruiz-Suárez*, 2013]. A handful of attempts have mimicked low-gravity conditions [*Goldman and Umbanhowar*, 2008; *Brzinski and Durian*, 2010; *Chen et al.*, 2009; *Constantino et al.*, 2011; *Dorbolo et al.*, 2013; *Brzinski et al.*, 2013], mainly by using air-fluidized granular beds or grains immersed in a liquid, but the main focus has typically been on the role of intruder velocity or grain friction. Here we focus exclusively on the role of gravity as an object settles into granular media. By conducting experiments in a freely falling reference frame, we are able to create true low- and high-gravity conditions as a sphere gently settles into a loose granular bed. We confirm the previously reported [*Goldman and Umbanhowar*, 2008], but hereto unexplained, observation that the rest time, t_{rest} (i.e., the total time required for the object to come to rest), scales like $g_{eff}^{-1/2}$. We also find, surprisingly, that the rest depth, z_{rest}, is *independent* of g_{eff}. We confirm these results and extend the range of g_{eff} with the aid of discrete element modeling (DEM) simulations, which highlight the sudden transition from fluid-like to solid-like response when the sphere comes to rest. Finally, with a simple analytical model we show that the depth-dependent stopping force against penetration of an intruder into granular matter is proportional to the effective gravity, an hypothesis widely used, but never before verified in an experiment where the effective gravity is changed.

We vary g_{eff} using a five-story (15 m) tall Atwood machine in which one of the counterweights is a wireless "lab-in-a-bucket" (Figure 1). The cylindrical bucket (30 cm diameter by 26 cm depth) is filled with expanded polystyrene beads (average diameter $d = 5.0$ mm, density $\rho = 0.014 \pm 0.002$ g/cm^3, and packing fraction $\phi = 0.68 \pm 0.01$). We choose this as our granular material because its low density facilitates the penetration

AGU Geophysical Research Letters 10.1002/2014GL059229

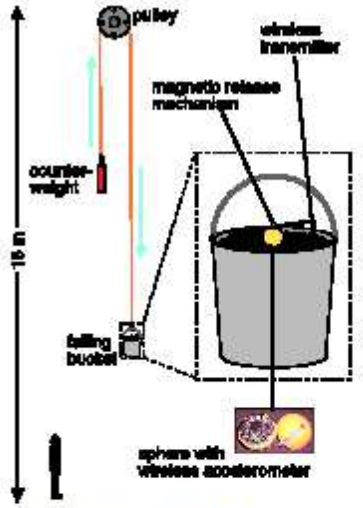

Figure 1. Freely falling granular laboratory. A five-story (15 m) tall Atwood machine controls the downward/upward acceleration of a 30 cm diameter laboratory in a bucket filled with the granular medium. As the bucket falls/rises, a sphere is released from rest and allowed to sink while "feeling" the effective gravity g_{eff} of the accelerating frame. We use an accelerometer embedded in the sphere for real-time measurement of the post-release acceleration.

of the intruder, thus making the experiments possible. Although it is lighter and indeed much softer than terrestrial or extraterrestrial soils, our results can be explained without any consideration of bead compression, which suggests that it behaves similarly to more "typical" granular media. Depending on the relative masses of the counterweight and bucket (plus contents), the laboratory can either fall or rise. As it does so, the bucket and the equipment inside it "feel," for a few seconds, a gravitational acceleration, g_{eff}, different than g (smaller if it is falling and larger if it is rising). During the fall (or rise), we release a sphere (diameter $D = 4$ cm, mass $m = 23$ g) held at rest just above the free surface and let it sink into the granular medium. The sphere houses a three-axis wireless accelerometer in its interior, allowing us to record its instantaneous acceleration. The sphere/accelerometer is light enough to prevent the "infinite penetration" encountered by *Pacheco-Vázquez et al.* [2011] (For further experimental details, see supporting information.).

Figure 2a shows the sphere's acceleration a versus time t relative to the Lagrangian frame of the moving bucket (normalized by $g = 9.8$ m/s^2) for six values of g_{eff} (note that z positive points downward and that the data represent the proper acceleration of the sphere, i.e., the acceleration caused by the forces exerted on it by the granular medium). Each curve has three well-defined sections: (i) a region of positive slope associated with the release (caused by magnetic trigger and occurring in the first ~50 ms), (ii) a second region of negative slope corresponding to the majority of the penetration process, and (iii) a third region of positive slope corresponding to sudden stopping of the sphere (a feature also seen in experiments performed at $g_{eff} = g$). We note the presence of a brief, damped oscillation that occurs near the instant the sphere comes to rest, which may signify the presence of a granular shock. The oscillations in the a versus t curves are not an experimental artifact but instead are real fluctuations from the granular medium (the simulations show similar oscillations). The minor differences between the curves in Figure 2 (especially those in region (i)) arise from the sensitivity to vibrations of the magnetic release system. Error bars are estimated from repeated runs of the same experiment (i.e., the same g_{eff}) and subsequent calculation of the standard deviation from the mean for the three representative parameters: the duration of the penetration process, the maximum (positive) acceleration, and the minimum (negative) acceleration (5 ms, 0.6 m/s^2, and 1.0 m/s^2, respectively). These relatively small errors are consistent with the fact that the "global" experimental features described below are reproducible not only for the set of curves displayed in Figure 2 but also for several other runs not included in the graph to avoid overcrowding. As we shall show shortly, the validity of these experimental results is also confirmed by discrete computer simulations.

Comparison of the different curves in Figure 2a shows that as g_{eff} decreases from approximately Uranus' gravity to Mars' gravity, the peak acceleration increases while the depth of the minimum decreases. Additionally, the duration of the process as a whole increases. This point is made particularly clear in Figure 2b, where we integrate a versus t and plot the velocity v versus t, which also shows that the maximum speed of the sphere increases with higher g_{eff}. In Figure 2c, we integrate once more to plot the distance traveled below the surface z versus t, which reveals the key observation that the rest depth z_{rest} is essentially the same for all g_{eff} (average value $z_{rest} = 14.0 \pm 0.6$ cm). If instead of plotting the a versus t we plot it against z (normalized by g_{eff}, as in Figure 2d), we collapse the data to a line with slight upward curvature (apart from the brief initial and final moments, corresponding to sections (i) and (iii), respectively).

AGU Geophysical Research Letters 10.1002/2014GL059229

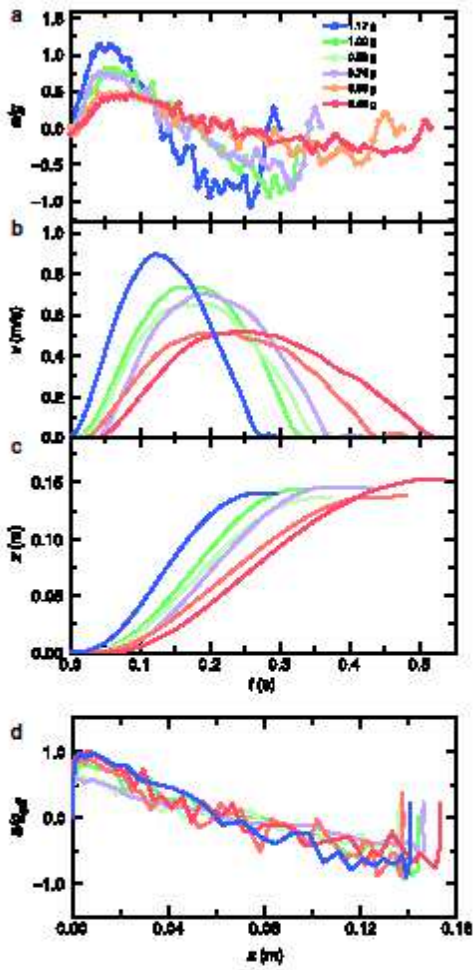

Figure 2. Experimental sink dynamics. (a) Sphere acceleration a/g versus time t for six representative values of g_{eff}. Values for g_{eff} are indicated in the legend in the figure and also correspond to following panels. (b) Time dependence of the sphere's velocity v via numerical integration of Figure 2a. (c) Time dependence of sphere's penetration below free granular surface z, calculated via integration of Figure 2b. (d) Normalized sphere acceleration a/g_{eff} versus penetration distance z.

Figures 3a–3d show the simulation results for similar gravitational accelerations to those used in the experiments. (For simulation details, see supporting information.) Several experimental features are reproduced quantitatively with no free parameters, e.g., the duration of the process, the size of the acceleration peaks, the maximum velocities, and the rest depth. Closer inspection reveals that the fluctuations in the acceleration become stronger as the sphere comes closer to stopping, likely indicative of the building up and breaking down of force chains (this will be the subject of future work). This suggests that the stopping and eventual static support of the intruder is associated with the medium transitioning from a fluidized to jammed state [*Kondic et al.*, 2012; *Bi et al.*, 2011].

In Figure 4, we plot the rest depth, z_{rest}, (Figure 4a) and rest time, t_{rest}, (Figure 4b) versus g_{eff}, which shows that z_{rest} is essentially independent of g_{eff} while t_{rest} scales like $g_{eff}^{-1/2}$. We can explain the scaling of the rest time with g_{eff} based on the work of *Pacheco-Vázquez et al.* [2011], who proposed a simple equation of motion for an object penetrating into a granular medium

$$ma = mg - \eta v^2 - \kappa\lambda(1 - e^{-(z/\lambda)}), \quad (1)$$

where m is the impactor mass, η characterizes inertial drag, κ is a friction-like coefficient related to the pressure in the granular medium (unit N/m), and λ is a characteristic length on the order of the width of the container. (The exponential term arises from the well-known Janssen effect in which the pressure in a granular system saturates at a finite depth owing to redistribution of weight to the container walls [*Sperl*, 2006].) For sufficiently large m, the combination of the inertial term ($\propto v^2$) and the saturating, depth-dependent term (i.e., the exponential) leads to "infinite penetration" of the projectile at a constant, terminal velocity. Here, however, because the sphere starts at rest and is relatively light, we can ignore the drag term. Thus, the equation of motion can be approximated as

$$ma = mg_{eff} - \kappa\lambda\left(1 - e^{-(z/\lambda)}\right). \quad (2)$$

This quickly explains the shape of the a/g_{eff} versus z curves shown in Figure 2d (in particular reproducing the upward curvature). Fitting each of the a/g_{eff} versus z curves with equation (2) while using the bucket

AGU Geophysical Research Letters 10.1002/2014GL059229

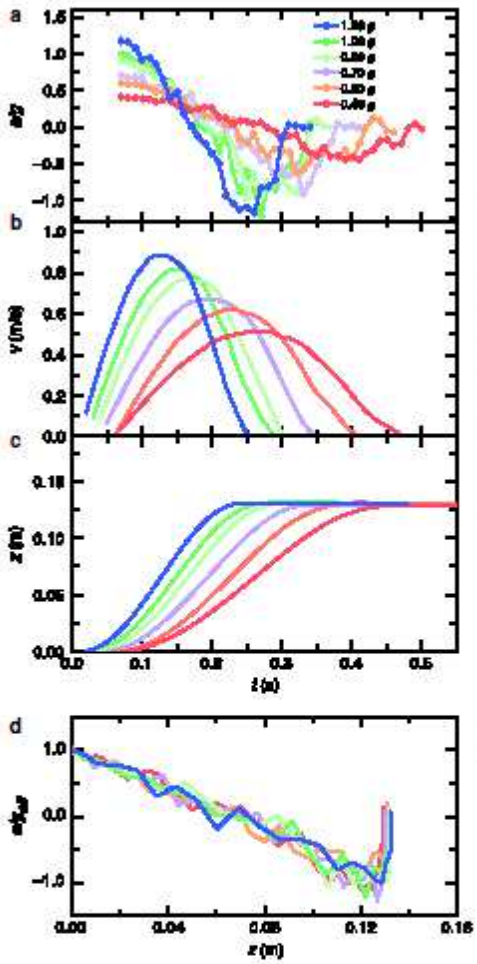

Figure 3. Simulation sink dynamics. (a) Sphere acceleration a/g versus time t for six representative values of g_{eff}. Values for g_{eff} are indicated in the legend in the figure and also correspond to the following panels. (b) Time dependence of the sphere's velocity v via numerical integration of Figure 4a. (c) Time dependence of sphere's penetration below free granular surface z, calculated via integration of Figure 4b. (d) Normalized sphere acceleration a/g_{eff} versus penetration distance z.

radius for the parameter λ and leaving κ as a free parameter, we find $\kappa = \alpha g_{eff}$, where $\alpha = 0.415 \pm 0.004$ Ns^2/m^2, as shown in Figure 4c. The proportionality between κ and α has been proposed before [*Katsuragi and Durian*, 2007; *Constantino et al.*, 2011], but here we demonstrate its validity at gravities above and below g for the first time (and indeed even with a much lighter granular material). Taking into account the numerical value obtained for α, we point out that this depth-dependent term is *not* caused by "hydrostatic pressure." If this were the case, we would expect $\alpha \approx \rho\pi D^2/4$. However, we find $\alpha/(\rho\pi D^2/4) \approx 34.6$, indicating that hydrostatic pressure adds just a small contribution to the depth-dependent force (in other experimental configurations, the equivalent ratio is smaller [*Constantino et al.*, 2011]).

We can reconcile our phenomenological model with the observation that the rest time scales like $g_{eff}^{-1/2}$. To show this, we begin by rewriting equation (2) as

$$v\frac{dv}{dz} = g_{eff}\left[1 - \frac{\alpha\lambda}{m}\left(1 - e^{-(z/\lambda)}\right)\right]. \quad (3)$$

We integrate this equation with respect to z (with the initial conditions $z_0 = 0$ and $v_0 = 0$) to find

$$\frac{1}{2}v^2 = g_{eff}\left[z\left(1 - \frac{\alpha\lambda}{m}\right) - \frac{\alpha\lambda^2}{m}\left(e^{-z/\lambda} - 1\right)\right]. \quad (4)$$

Next, we isolate the velocity term, take the square root of both sides (note we are interested in $t_{rest} > 0$ and thus use the positive root), and integrate once more, which gives

$$t_{rest} = (2g_{eff})^{-1/2}\int_0^{z_{rest}}\left[z\left(1 - \frac{\alpha\lambda}{m}\right) + \frac{\alpha\lambda^2}{m}\left(1 - e^{-z/\lambda}\right)\right]^{-1/2} dz. \quad (5)$$

The term in the integral is independent of g_{eff} (as λ, α, and m are strictly independent of g_{eff} and z_{rest} is empirically so). This reveals that $t_{rest} \propto (l_c/g_{eff})^{1/2}$, where l_c is a characteristic length. In the limit $\lambda \to \infty$, it is easy to show that $l_c \propto z_{rest}$, and consequently, the whole problem can be rescaled in terms of t_{rest} and z_{rest}. For finite λ, the average stopping force is smaller and the ball penetrates further into the medium than this simple scaling would suggest. Nonetheless, in realistic geophysical situations where no confining walls are present, λ is indeed large and the simple scaling might prove very useful.

AGU Geophysical Research Letters 10.1002/2014GL059229

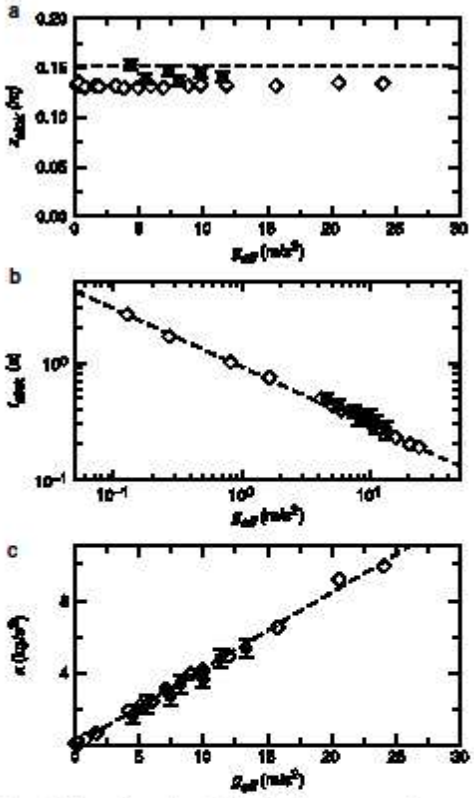

Figure 4. Penetration scalings. (a) Rest depth z_{rest} versus g_{eff} for experiment (black circles) and simulations (open diamonds). Dashed line is the predicted rest depth based on equation (6). (b) Rest time t_{rest} versus g_{eff}. Fit to simulation data is power law with exponent −1/2, as predicted in equation (5). (c) Frictional sink parameter κ versus g_{eff}. Values for κ are calculated from individually fitting σ versus z curves to equation (3) with λ = 15 cm (i.e., the radius of the container holding the granular material). Symbols in Figures 4b and 4c are the same as in Figure 4a.

Finally, this model also leads to the conclusion that z_{rest} is independent of g_{eff}. When the sphere reaches its resting spot, the velocity vanishes, and thus, we can set the left-hand side of equation (4) to zero, i.e.,

$$\left(1-\frac{\alpha\lambda}{m}\right)z_{rest}=\frac{\alpha\lambda^2}{m}\left(e^{-z_{rest}/\lambda}-1\right). \quad (6)$$

This is a transcendental equation that cannot be solved analytically. However, quick inspection reveals that z_{rest} is independent of the gravitational acceleration as g_{eff} is not present. Moreover, we can use the experimental parameters λ = 0.15 m and α = 0.415 Ns^2/m^2 to solve equation (6) numerically, which gives $z_{rest} \approx$ 0.15 m, close to what we actually measure (0.14 ± 0.06 m). The fact that it is somewhat larger may result from ignoring the velocity term in equation (1), which would tend to make the sphere stop a little earlier. (Indeed, numerically solving equation (1) directly with the value for η from *Pacheco-Vázquez et al.* [2011] gives z_{rest} = 0.14 m, in better agreement still with the data from the experiments and simulations.)

To our knowledge, this work is the first to report on the full settling dynamics of an object into granular media at different gravities from that of Earth. By using a freely falling laboratory, we are able to investigate g_{eff} ranging roughly from the conditions of Mars to Uranus. We reproduce and extend this range with the aid of DEM simulations, which highlight the importance of transient force fluctuations in the penetration process that may be related to the continual buildup and breakdown of granular force chains. In both the experiments and simulations, we make a counterintuitive observation that may have important implications for extraterrestrial navigation and engineering, namely that the rest depth of an object set on the surface of granular media is independent of the ambient gravitational acceleration. We explain this peculiar observation with a force law that includes a depth-dependent frictional term proportional to g_{eff}, which effectively removes any gravitational term from the equation of motion at the point of static equilibrium. From the point of view of surface morphology, our results suggest that the initial stage of sedimentation into granular media on different celestial bodies should be largely independent of local gravitational acceleration, i.e., the size of the body. Furthermore, this has the fortuitous implication that Earth-based experiments aimed at reproducing the conditions of robot navigation on permanent construction on another planet or asteroid should be performed without "adjusting" the mass for the extraterrestrial gravity conditions.

Acknowledgments

The data for this paper are available by contacting E. Altshuler (ealtshuler@fisica.uh.cu). The Spanish MINECO project FIS2011-26675, the PIUNA program (U. Navarra), and the Project 29942WL (Fonds de Solidarité Prioritaire France-Cuba) have partially supported this research. We acknowledge the collaboration of O. Ramos, J. Wu, A. J. Batista Leyva, and the Zeolites Group (IMRE, University of Havana). E. Altshuler thanks the late M. Álvarez-Ponte for inspiration.

The Editor thanks two anonymous reviewers for their assistance in evaluating this paper.

References

Almeida, M. P., E. J. Parteli, J. S. Andrade Jr., and H. J. Herrmann (2008), Giant saltation on Mars, *Proc. Natl. Acad. Sci. U.S.A.*, *105*, 6222–6226, doi:10.1073/pnas.0800202105.

Asphaug, E. (2007), The shifting sands of asteroids, *Science*, *316*, 993–994, doi:10.1126/science.1141971.

Bi, D., J. Zhang, B. Chakraborty, and R. P. Behringer (2011), Jamming by shear, *Nature*, *480*, 355–358, doi:10.1038/nature10667.

Boudet, J. F., Y. Amarouchene, and H. Kellay (2006), Dynamics of impact cratering in shallow sand layers, *Phys. Rev. Lett.*, *96*, 158001-4, doi:10.1103/PhysRevLett.96.158001.

Brzinski, T. A., III, and D. J. Durian (2010), Characterization of the drag force in an air-moderated granular bed, *Soft Matter*, *6*, 3038–3043, doi:10.1039/B926180J.

Brzinski, T. A., III, P. Mayor, and D. J. Durian (2013), Depth-dependent resistance of granular media to vertical penetration, *Phys. Rev. Lett.*, *111*, 168002, doi:10.1103/PhysRevLett.111.168002.

Chen, L., P. B. Umbanhowar, H. Komsuoglu, D. E. Koditschek, and D. I. Goldman (2009), Sensitive dependence of the motion of a legged robot on granular media, *Proc. Natl. Acad. Sci. U.S.A.*, *106*, 3029–3034, doi:10.1073/pnas.0809095106.

Constantino, D. J., J. Bartell, K. Scheidler, and P. Schiffer (2011), Low-velocity granular drag in reduced gravity, *Phys. Rev. E*, *83*, 011305-4, doi:10.1103/PhysRevE.83.011305.

de Vet, S. J., and J. R. de Bruyn (2007), Shape of impact craters in granular media, *Phys. Rev. E*, *76*, 041306-4, doi:10.1103/PhysRevE.76.041306.

Dorbolo, S., F. Ludewig, and N. Vandewalle (2013), Bouncing trimer: A random self-propelled particle, chaos and periodical motions, *Granular Matter*, *15*, 033016-033038, doi:10.1088/1367-2630/11/3/033016.

Elvis, M. (2012), Let's mine asteroids—For science and profit, *Nature*, *485*, 549, doi:10.1038/485549a.

Goldman, D. I., and P. Umbanhowar (2008), Scaling and dynamics of sphere and disk impact into granular media, *Phys. Rev. E*, *77*, 021308-14, doi:10.1103/PhysRevE.77.021308.

Katsuragi, H., and D. J. Durian (2007), Unified force law for granular impact cratering, *Nat. Phys.*, *3*, 420–423, doi:10.1038/nphys583.

Katsuragi, H. (2012), Nonlinear wall pressure of a plunged granular column, *Phys. Rev. E*, *85*, 021301-5, doi:10.1103/PhysRevE.85.021301.

Kondic, L., X. Fang, W. Losert, C. S. O'Hern, and R. P. Behringer (2012), Microstructure evolution during impact on granular matter, *Phys. Rev. E*, *85*, 011305-17, doi:10.1103/PhysRevE.85.011305.

Miyamoto, H., et al. (2007), Regolith migration and sorting on asteroid Itokawa, *Science*, *316*, 1011–1014, doi:10.1126/science.1134390.

Pacheco-Vázquez, F., G. A. Caballero-Robledo, J. M. Solano-Altamirano, E. Altshuler, A. J. Batista-Leyva, and J. C. Ruiz-Suárez (2011), Infinite penetration of a projectile into a granular medium, *Phys. Rev. Lett.*, *106*, 218001-4, doi:10.1103/PhysRevLett.106.218001.

Ruiz-Suárez, J. C. (2013), Penetration of projectiles into granular targets, *Rep. Prog. Phys.*, *76*, 1–23, doi:10.1088/0034-4885/76/6/066601.

Shinbrot, T., N.-H. Duong, L. Kwan, and M. M. Alvarez (2004), Dry granular flows can generate surface features resembling those seen in Martian gullies, *Proc. Natl. Acad. Sci. U.S.A.*, *101*, 8542–8546, doi:10.1073/pnas.0308251101.

Sperl, M. (2006), Experiments on corn pressure in silo cells: Translation and comment on Janssen's paper from 1895, *Granular Matter*, *39*, 59–65, doi:10.1007/s10035-005-0224-z.

Thomas, P. C., and M. S. Robinson (2005), Seismic resurfacing by a single impact on the asteroid 433 Eros, *Nature*, *436*, 366–369, doi:10.1038/nature03855.

Uehara, J. S., M. A. Ambroso, R. P. Ojha, and D. J. Durian (2003), Low-speed impact craters in loose granular media, *Phys. Rev. Lett.*, *90*, 194301-4, doi:10.1103/PhysRevLett.90.194301.

Walsh, A. M., K. E. Holloway, P. Habdas, and J. R. de Bruyn (2003), Morphology and scaling of impact craters in granular media, *Phys. Rev. Lett.*, *91*, 104301-4, doi:10.1103/PhysRevLett.91.104301.

3.2 Supplementary information.

3.2.1 Experimental setup: furher details.

The granular media consists of expanded polystyrene particles with a density of 0.014 ± 0.002 g/cc and diameters ranging from approximately 2.0 to 6.5 mm (with a peak at 5.8 mm). To ensure that the system has a similar initial configuration each experiment, we use the following procedure adapted from Torres et al. (Torres et. al, 2012): First, we inject air from below through a wire mesh with a pressure ramp just until the top of the bed just becomes fluidized. Then we slowly lower the pressure until there is zero flow. Next, we shake the container horizontally for 5 seconds (the oscillations are approximately sinusoidal, with a period of 0.225 ± 0.004 s and an acceleration amplitude of 1.9 ± 0.3 m/s^2). This process repetitively produces a volume fraction of 0.68 ± 0.01 and maximum angle of stability of $30.29^o \pm 0.50^o$.

The sphere is quickly released into free-fall with the aid of a magnetic latch. The exact moment of release is determined by remotely observing the bucket acceleration with a computer and, once it is confirmed that the bucket moves with constant acceleration g_{eff}, deactivating the latch. Care is taken to ensure that little lateral motion occurs and that at release the bottom of the sphere is just gently touching the free granular surface. The 3-axis accelerometer inside the sphere has a resolution of 10−4g and is able to transmit data in real time at 2.4 GHz to a USB node on an external PC at a data point rate of 120 Hz. The device had a saturation acceleration of ~ 8g (Freescale semiconductor, 2009).

3.2.2 Discrete elements simulations: further details.

We use discrete element modeling (DEM) to simulate a large sphere sinking into a granular bed composed of smaller spheres (Poschel & Schwager, 2005). The implementation is a hybrid CPU/GPU algorithm that allows us to efficiently evaluate the dynamics of several hundred thousand particles (Hidalgo, Kanzaki, Alonso-Marroquin, & Luding, 2013), (Longmore, Marais, & Kuttel, 2013) (Owens, Houston, Luebke, & als., 2008). We initiate each simulation

by generating a random granular packing of monodisperse spheres (radius r and density ρ) at packing fraction $\varphi = 0.62 \pm 0.02$. The spherical intruder (R = 8r and density $\rho_{int} = 50\rho$) is released from the free granular surface with zero initial velocity.

For each particle $i = 1 \ldots N$ the DEM simulation includes three translational degrees of freedom and the rotational movement is described by a quaternion formalism. The interaction force between particle i and particle j, is composed by normal and tangential components $\vec{F}_{ij} = \vec{F}_{ij}^{n} + \vec{F}_{ij}^{t}$. In our approach, the normal interaction force between the particles $\vec{F}_{ij}^{n}$ depends non-linearly on the particles overlap distance δ. Moreover, the local dissipation is introduced by a non-linear viscous damping term, which depends on the normal relative velocity $\vec{v}_{rel}^{n}$. Hence, the total normal force reads as $\vec{F}_{ij}^{n} = -k_n \delta^{\frac{3}{2}} \hat{n} - \gamma_n m_e \vec{v}_{rel}^{n} \delta^{\frac{1}{4}}$, where k_n and γ_n represent elastic and damping coefficients and $m_e = m_i m_j / (m_i + m_j)$. The tangential component $\vec{F}_{ij}^{t}$ also includes an elastic term and a viscous term, $\vec{F}_{ij}^{t} = k_t \vec{\varepsilon} - \gamma_t m_e \vec{v}_{rel}^{t}$, where γ_t is a damping coefficient and $\vec{v}_{rel}^{t}$ is the tangential relative velocity of the overlapping pair. The variable $|\vec{\varepsilon}|$ represents the elongation of an imaginary spring with elastic constant k_t. As long as there is an overlap between the interacting particles, $\vec{\varepsilon}$ increases as $d\vec{\varepsilon}/dt = \vec{v}_{rel}^{t}$ (Pöschel and Schwager, 2005). The elastic tangential elongation $\vec{\varepsilon}$ is kept orthogonal to the normal vector (Weinhart et. al, 2012) and it is truncated as necessary to satisfy the Coulomb constraint $|\vec{F}_{ij}^{t}| < \mu |\vec{F}_{ij}^{n}|$, where μ is the friction coefficient.

The translational and rotational motion of each particle is governed by the Newton's equation of motion,

$$\sum_{j=1}^{N_c} \vec{F}_{ij} + m\hat{g} = m\frac{d\vec{v}}{dt} \qquad (1)$$

and

$$\sum_{j=1}^{N_c} \left(\vec{I}_{ij} X \vec{F}_{ij}\right) = I\frac{d\vec{w}}{dt} \qquad (2)$$

In Eq (1) and Eq (2), the sums run over the N_c contacting particles of particle i. Moreover, the intensity of the gravitational field is represented by $\hat{g}$. The mass m and the moment of inertia $I = 2/5\ m\ R^2$ are input parameters and the branch vector $\vec{I}_{ij}$ characterizes the vector from the center of particle i and each contact point j. Eq (2) is the first step to simulate the evolution of

the particles angular velocity ω, in the body frame. However, a second step is necessary to solve the particle orientation, which is necessary to model frictional particles. Furthermore, the orientation coordinate is described by using a quaternion representation, which has demonstrated several technical advantages (Kuipers 2002). So that, in our model a normalized unit quaternion$= q_0 + q_1\hat{\imath} + q_2\hat{\jmath} + q_3\hat{k}$, $(\sum_{i=0}^{3} q_i^2 = 1)$ characterizes the particle orientation (see details in Wang et. al [2002]).

The equations of motion are integrated using Fincham's leap-frog algorithm (rotational) (Fincham, 1992) and a Verlet Velocity algorithm (translational) (Verlet, 1968). The molecular dynamics time step was set in $\Delta t = 10^{-6}$s.
In all the simulations reported here the values of elastic constant $k_n = 1.2 \times 10^6 \mathrm{N/m^{3/2}}$, density $\rho = 14\ \mathrm{kg/m^3}$, normal damping coefficient $\gamma_n = 12$ and friction $\mu = 0.5$ have been used. We keep $k_t/k_n = 2/7$ and $\gamma_t/\gamma_n = 0.1$, and only modify the gravitational field $\hat{g}$ from one simulation to the next. The gravity values are presented in terms of the gravity of Earth $g_{eff}\ g/g_e$.

The used contact parameters correspond approximately to particles with a Young's modulus $E = 10^4$kPa and normal and tangential restitution coefficient $e_n = e_t = 0.2$, which are very reasonable for expanded polystyrene (see http://polymoldingllc.com/ and http://www.starrfoam.com/ for more details). Although our contact formulation corresponds to a non-linear Hertz contact with constant restitution coefficient (Luding, 1998), similar outcomes were obtained when using a spring-dashpot formulation (Luding, 1998).

3.2.3 Article: H. Torres, A. González, G. Sánchez-Colina, J. C. Drake and E. Altshuler, Revista Cubana de Física, 29, 1E45 (2012).

Rev. Cub. Fis. **29**, 1E45 (2012) CONTRIBUTIONS

IMPACT DYNAMICS IN "HARD" AND "SOFT" GRANULAR MATTER

DINÁMICA DE IMPACTO EN MATERIA GRANULAR "DURA" Y "BLANDA"

H. Torres[a ‡], A. González[a ‡], G. Sánchez-Colina[a,b], J. C. Drake[a,b] and E. Altshuler[a †]

a) "Henri Poincaré" Group of Complex Systems, Physics Faculty, University of Havana, 10400 Havana, Cuba, ealtshuler@fisica.uh.cu†
b) General Physics Department, Physics Faculty, University of Havana, 10400 Havana, Cuba
‡ contributed equally as first authors.
† corresponding author

Using a wireless accelerometer, we explore the dynamics of penetration of a sphere falling into very light granular matter prepared with different compactions. The duration of the penetration process until the sphere stops is ~30% bigger for less compacted granular matter, while the maximum penetration depth is ~40% bigger in that case. These outputs are quite remarkable, considering that the differences in the filling factors of the two granular media were smaller than 5%.

Utilizando un acelerómetro inalámbrico, exploramos la dinámica de penetración de una esfera que cae sobre material granular muy ligero, preparado con dos compactaciones diferentes. La duración del proceso de penetración hasta que la esfera se detiene es un ~30% mayor para el medio menos compacto, mientras que la penetración máxima para ese medio es un ~40% mayor. Estos resultados son notables, considerando que la diferencia entre ambos factores de llenado es menor del 5%.

PACS: Granular materials rheology, 83.80.Fg; compaction, granular systems, 45.70.Cc; granular materials, 81.05.Rm

INTRODUCTION

Crater formation by impact in granular matter has been a subject of intense research in the last decade [1-7]. There is still debate about the form of the force law against penetration of the impactor, and how it depends on different experimental parameters, such as the density of the impacting object and the granular matter, the impact speed, the roughness and shape of the impactor, etc. Many of the existing reports concentrate in the study of the maximum penetration depth of the impacting object, and the diameter of the resulting crater. "Dynamical" studies, on the other hand, typically record the vertical position of the impactor during the penetration process [5], and only very few record *directly* its acceleration [6, 7].

In this paper, we use a wireless accelerometer to directly measure the acceleration of a sphere falling into extremely light granular matter, in order to find out how the penetration dynamics depend on the level of compaction of the granular medium.

EXPERIMENT

A cylindrical container of 30 *cm* diameter and 26 *cm* depth was filled with expanded polyestirene particles of density 0.014 ± 0.002 *g/cc* and diameter distributed between 2.0 and 6.5 *mm*, peaking at 5.8 *mm* [7]. Near the bottom of the container there was a fine horizontal mesh that allowed air to flow upwards injected by a compressor through a hole at the bottom of the system without loosing any granular material. This setup allowed us to prepare two types of granular matter:

Soft granular matter (SGM): Air was injected from the bottom from zero flow to a maximum, and then decreased back to zero flow (the maximum flow was selected in such a way that it produced visible "turbulence" at the free surface of the grains). The resulting granular medium, had a volume fraction of 0.64 ± 0.01. Using a rotating drum, we found that the maximum angle of stability for SGM was 29.52° ± 0.25°.

Hard granular matter (HGM): First, SGM was obtained. Then, the container was shaken horizontally for 5 seconds (the oscillations were approximately sinusoidal, with a period of 0.225 ± 0.004 *s* and acceleration amplitude of 1.9 ± 0.3 m/s^2). The resulting volume fraction was of 0.68 ± 0.01, and the maximum angle of stability was 30.29° ± 0.50°.

The impactor consisted in a 3-axis wireless accelerometer mounted into a 4-*cm* diameter ping-pong ball, in such a way that the z-axis of the accelerometer was pointing downwards along the vertical direction. The impactor weighted 23 grams (the lower hemisphere was more massive than the upper to guarantee minimal tilting when traveling through the granular media). The accelerometer had a resolution of 0.0001 *g*, and was able to transmit data in real time at 2.4 *GHz* to a USB node on an external PC, at a data point rate of 120 *Hz* [8].

A small magnet was glued to the top of the ping-pong ball, so

the impactor could be "magnetically hanged", through a fixed, thin horizontal plastic plate, from the lower end of a vertical iron rod that initially touched the upper face of the fixed plate. When the rod was lifted up using a computer-controlled electro-mechanical device, the impactor was dropped onto the granular system with very small lateral tilting. The impactor was always released from a height where its lower end was just "touching" the free granular surface.

In the experiment, the vertical acceleration of the impactor was recorded in real time during its penetration into the granular medium (its horizontal acceleration was negligible compared to that along z).

RESULTS AND DISCUSSION

Fig. 1 shows the evolution of the vertical acceleration, velocity and position of the sphere as it penetrates the granular matter for HGM (left column) and SGM (right column). Velocity and position graphs were obtained after one and two integrations, respectively, of the acceleration vs. time graph -i.e., the direct output from the accelerometer. The insets have been constructed by plotting the acceleration vs. the calculated position. The positive direction is taken downwards.

Let us examine Figs 1 (a) and (d), as time increases. Initially, $a = 0$, which indicates that the impactor is hanging from the release system. The release process takes less than 70 *ms* both for HGM and SGM, and occurs before the impactor has dropped to a depth of 0.5 *cm* (as suggested by the insets). Then, the downward acceleration increases to average maximum values of 8 ± 1 m/s^2 for HGM and 9 ± 1 m/s^2 for SGM (ideally it should reach 9,8 m/s^2, but the ball is touching the granular surface before being released). After that, a increases in the upwards direction due to the action of granular resistance, reaching average minima of 8 ± 1 m/s^2 for HGM and 9 ± 1 m/s^2 SGM respectively. Finally, zero acceleration is reached, meaning that the sphere has stopped moving (in the case of SGM, $a = 0$ only after a few damped oscillations). The final stage of the stopping process occurs sharply within a few-*mm* distance. A major difference between the two media is the duration of the whole process from release to stop: 340 ± 10 *ms* for HDM, and 470 ± 20 *ms* for SGM.

Figs 1 (b) and (e) show the velocity records resulting from integrating in time the acceleration. In both cases, velocity starts at zero, and reaches maxima of 0.7 ± 0.1 *m/s* and 1.0 ± 0.1 *m/s* for HGM and SGM, respectively. Then, it goes back to zero quite symmetrically in time.

Figs 1 (c) and (f) show the z-position resulting from the integration of the velocity records. In the case of HGM, the depth inside the granular matter goes from zero (at the surface) to 0.14 ± 0.01 *m* (approximately in the middle of the granular column). In the case of the SGM, the final depth gives $0,22 \pm 0,01$ *m* (we checked both values using a thin thread attached to the sphere). Notice that, in the latter case, the ball stops only 4 *cm* from the bottom of the bucket. The damped oscillations of the acceleration at the end of the penetration process may be related to a jammed (more compacted) section of the granular material produced by the impactor itself immediately under it, which acts as a "solid wall". The process is probably enhanced by the proximity of the bottom wall in the case of SGM.

All in all, we have shown that, when a granular system is compacted in such a way that the filling factor decreases just to 94% of its original value, the total penetration time can be reduced to a 70%, the maximum velocity of the impactor can decreased to a 70%, and its maximum penetration depth can be reduced to a 60% of its initial value.

It has been shown before that the equation of motion for penetration of a spherical intruder into a larger system analogous to our SGM can be written as [7]

$$m\frac{d^2z}{dt^2} = mg - \eta\left(\frac{dz}{dt}\right)^2 - \kappa\lambda\left(1 - e^{-\frac{z}{\lambda}}\right), \qquad (1)$$

where m and z are the mass of the sphere and the penetration depth from the free surface, respectively, λ is a characteristic length of the order of the diameter of the container, and the coefficients η and κ characterize the inertial drag, and a depth-dependent friction, respectively. This equation follows well most of the motion [7], but it cannot describe the release process at the very beginning and the final stopping stage (where the acceleration goes suddenly to zero when the ball stops in the bulk of the granular system).

In order to estimate parameters, we use two expressions associated to the motion far from its ends. From (1), it is not difficult to see that

$$\kappa = m\left|s_{a\to 0}\right|e^{z_{a\to 0}/\lambda}, \qquad (2)$$

where $s_{a\to 0}$ and $z_{a\to 0}$ are the slope of the a vs. z graph (see insets), and the depth of the impactor when the acceleration approaches zero, respectively. Assuming $\lambda \sim 0.3$ *m* the resulting values for HGM and SGM cannot be clearly differentiated, and give a value of $\kappa = 1.9 \pm 0.3$ kg/s^2, which is near the value reported in [7] for a 6-*m* long cylinder with SGM. Additionally,

$$\eta = \frac{1}{v_{max}^2}\left[mg - \kappa\lambda\left(1 - e^{-z_{max}/\lambda}\right)\right], \qquad (3)$$

where v_{max} is the maximum speed of the impactor during penetration, and z_{max} is the depth at which the ball experiences that speed. Equation (3) gives $\eta_{HGM} = 0.16 \pm 0.02$ kg/m for HGM and $\eta_{SGM} = 0.05 \pm 0.02$ kg/m for SGM. The latter value is close to that estimated in [7].

CONCLUSION

We have shown that, when a granular system is compacted, a small increase in compaction produces an increase in the penetration time, a decrease in the total penetration depth, and a sizable increase in the inertial drag coefficient.

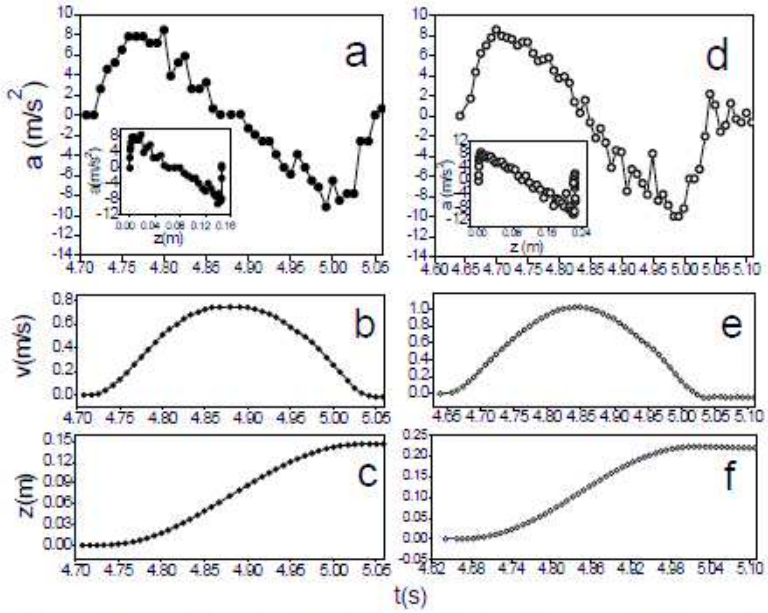

Figure 1: Experimental results. (a) - (c) Vertical acceleration, velocity and position of the impactor vs. time graphs, respectively, for Hard Granular Matter (inset is Acceleration vs. position). (d) - (f) Analogous graphs for Soft Granular Matter. Positive reference points downward.

ACKNOWLEDGEMENTS

We acknowledge C. Pérez-Penichet for contributing to the electronics, O. Ramos, J. Wu and C. Ruiz-Suárez for support in the experimental setup, and A. Batista-Leyva, L. P. Kadanoff and S. Waitukaitis for useful discussions.

[1] J. S. Uehara, M. A. Ambroso, R. P. Ojha and D. J. Durian, Phys. Rev. Lett. **90**, 194301 (2003).
[2] A. M. Walsh, K. E. Holloway, P. Habdas and J. R. de Bruyn, Phys. Rev. Lett. **91**, 104301 (2003).
[3] S. J. de Vet and J. R. de Bruyn, Phys. Rev. E. **76**, 041306 (2007).
[4] J. F. Boudet, Y. Amarouchene, and H. Kellay, Phys. Rev. Lett. **96**, 158001 (2006).
[5] H. Katsuragi and D. Durian, Nat. Phys. **3**, 420 (2007).
[6] D. I. Goldman and P. Umbanhowar, Phys Rev. E **77**, 021308 (2008).
[7] F. Pacheco-Vázquez, G. A. Caballero-Robledo, J. M. Solano-Altamirano, E. Altshuler, A. J. Batista-Leyva and J. C. Ruiz-Suárez, Phys. Rev. Lett. **106**, 218001 (2011).
[8] See MMA7660FC ZSTAR3 accelerometer details at www.freescale.com/zstar
[9] T. Brzinski and D. J. Durian, Soft Matter **6**, 3038 (2011).
[10] D. J. Constantino, J. Bartell, K. Scheidler and P. Schiffer, Phys. Rev. E **83**, 0011305 (2011).

CHAPTER 4 "Lock-in accelerometry" to follow sink dynamics in shaken granular matter.

4.1 Article: G. Sánchez-Colina, L. Alonso-Llanes, E. Martínez, A. J. Batista-Leyva and E. Altshuler, *Review of Scientific Instruments* 85, 126101 (2014).

4.2 Supplementary information.

4.2.1 L. Alonso-Llanes, G. Sánchez-Colina, E. Martínez, A. J. Batista-Leyva, R. Toussaint and E. Altshuler, accepted by the *Revista Cubana de Física* (2016).

4.1 Article: G. Sánchez-Colina, L. Alonso-Llanes, E. Martínez, A. J. Batista-Leyva and E. Altshuler, Review of Scientific Instruments 85, 126101 (2014).

REVIEW OF SCIENTIFIC INSTRUMENTS 85, 126101 (2014)

Note: "Lock-in accelerometry" to follow sink dynamics in shaken granular matter

G. Sánchez-Colina,[1] L. Alonso-Llanes,[1] E. Martínez,[1] A. J. Batista-Leyva,[1,2] C. Clement,[3] C. Fliedner,[3] R. Toussaint,[3] and E. Altshuler[1,a)]
[1]"Henri Poincaré" Group of Complex Systems, Physics Faculty, University of Havana, 10400 Havana, Cuba
[2]Instituto Superior de Tecnologías y Ciencias Aplicadas, 10400 La Habana, Cuba
[3]Institut de Physique du Globe de Strasbourg (IPGS), Ecole et Observatoire des Sciences de la Terre (EOST), University of Strasbourg/CNRS, 67084 Strasbourg, France

(Received 29 October 2014; accepted 18 November 2014; published online 3 December 2014)

Understanding the penetration dynamics of intruders in granular beds is relevant not only for fundamental physics, but also for geophysical processes and construction on sediments or granular soils in areas potentially affected by earthquakes. While the penetration of intruders in two dimensional (2D) laboratory granular beds can be followed using video recording, this is useless in three dimensional (3D) beds of non-transparent materials such as common sand. Here, we propose a method to quantify the sink dynamics of an intruder into laterally shaken granular beds based on the temporal correlations between the signals from a *reference* accelerometer fixed to the shaken granular bed, and a *probe* accelerometer deployed inside the intruder. Due to its analogy with the working principle of a lock-in amplifier, we call this technique lock-in accelerometry. © *2014 AIP Publishing LLC.* [http://dx.doi.org/10.1063/1.4902979]

During earthquakes, some soils can lose their ability to sustain shear and deform, causing subsidence and sometimes substantial building damage due to deformation or tumbling.[1–3] This soil liquefaction phenomenon happens typically in granular soils, wet or dry, and in saturated sedimentary soils. The stability under seismic waves has been studied for sand[4] and dry granular soils,[5] or for sediments.[3] Laboratory research related to the subject is usually performed by rheological tests and numerical modeling.[3] The study of soil liquefaction using free surface boundary conditions, similar to the natural one, can benefit from direct measurement of the acceleration of soils submitted to oscillatory motion similar to those due to seismic waves. The present article describes the development of a lock-in accelerometry technique aimed at such measurements.

In the case of quasi-2D systems (like an intruder sinking into a Hele-Shaw cell filled with smaller sized grains) the penetration can be followed by means of a video camera.[6–8] But video techniques are of no use to study the penetration into a 3D system of non-transparent grains, where the dynamics can be quite complex.[9] In those cases, wireless accelerometry constitutes a natural alternative that has been reported in very few occasions, as far as we know.[10–13]

However, *in situ* accelerometry has never been used to quantify the penetration into horizontally shaken, sandy granular beds, where the vertical acceleration is small and then, difficult to follow. In this Note, we propose a method to determine the sink time of an intruder into a horizontally shaken, fluidized granular bed based on the correlations between the signals of reference and probe accelerometers. The effectiveness of the system has been tested experimentally both in quasi-2D and in 3D systems.

a)Electronic mail: ealtshuler@fisica.uh.cu

Figure 1 shows our experimental quasi-2D setup. We use a Hele-Shaw cell that can oscillate laterally using an electromagnetic shaker with an amplitude of 1.5 cm and a maximum frequency of $\nu = 6$ Hz. The cell consists in two vertical glasses separated by a gap of 21.4 ± 0.2 mm with wooden walls at the bottom and sides, filled up with multidisperse polymer particles, with average size of 0.7 ± 0.1 mm. At the bottom of the cell, a horizontal hose with 30 holes of 0.5 mm diameter each can inject air into the granular system at a flow rate ranging from 200 to 2200 cm^3/h. In the experiments presented here, the air flow ranges from 600 to 800 cm^3/h. Up to here, the system is analogous to previous ones reported in the literature.[14] However, in our case an intruder consisting in a squared parallelepiped 50 mm side, 19 mm thickness, and a weight of 51 g is released on the free surface of the granular medium to study its sinking following a protocol to be explained later on. A digital camera *Hero 2* made by *GoPro* is fixed to the electromagnetic shaker, in such a way that it can take a video of the sinking process from an oscillating reference frame locked to the Hele-Shaw cell. Videos can be taken at a maximum rate of 120 frames per second (fps), with a resolution of 1920 × 1080 pixels.

Finally, two 3-axis, wireless accelerometers are fixed to the Hele-Shaw cell (labeled *Ref*), and inside the intruder (labeled *Probe*), respectively. The x, y, and z axis of the accelerometers are oriented as illustrated in Fig. 1 for the case of the reference accelerometer. Each 3-axis accelerometer has a resolution of 10^{-4} g and is able to transmit data in real time at 2.4 GHz to a USB node on an external PC at a maximum data point rate of 120 Hz. This signal is used in the experiments here reported. The device[15] has a saturation acceleration of 8 g ($g = 9.81$ m/s^2).

The protocol of a typical experiment can be described as follows. First, the granular bed is prepared by injecting air

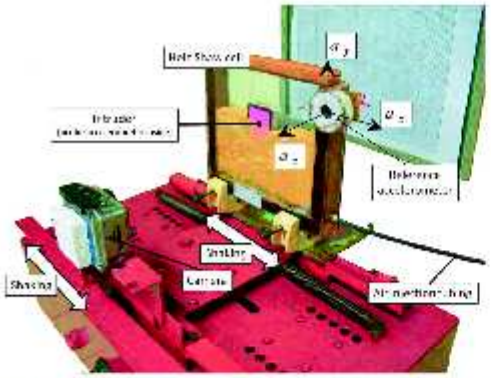

FIG. 1. Experimental setup for quasi-2D measurements. Both the Hele-Shaw cell and the camera are synchronously shaken in the lateral direction. Accelerometers attached to the Hele-Shaw cell and the intruder bring the key information to quantify the sink dynamics.

from the bottom, for 10 s. Then, the intruder is settled on the free surface of the granular bead. After activating the video camera and the accelerometers, the electromagnetic shaker and the air injection system are started at the same time, and turned off after 10 s, where the penetration process has ended. Then, the video and the acceleration records are analyzed.

As the horizontal acceleration is oriented in the x direction for both accelerometers (*Ref* and *Probe*), we will compare both data sets $a_{x,R}$, $a_{x,P}$ using a modification of the Pearson correlation coefficient[16] aimed at decreasing the noise in the output. The modification consists in calculating the evolution of the Pearson's coefficient within time intervals of size D, each one starting at moment k, as follows:

$$r(k) = \frac{\sum_{i=k}^{k+D} a_{x,R}(i)a_{x,P}(i)}{\left[\sum_{i=k}^{k+D}(a_{x,R}(i))^2 \sum_{i=k}^{k+D}(a_{x,P}(i))^2\right]^{\frac{1}{2}}}. \quad (1)$$

In the formula above, i represents the sampled time index and N is the total number of experimental data points (so k runs from 1 to $N - D$).

The idea behind our experiment is that when the intruder is sinking, it cannot be tightly bounded to the granular mass, so there will be a delay between $a_{x,R}$ and $a_{x,P}$, giving a low correlation coefficient. On the contrary, when the intruder ends the sinking process, it starts to move synchronously with the reference frame, and so the correlation between $a_{x,R}$ and $a_{x,P}$ will be high. Since lock-in amplifiers work by comparing an oscillatory excitation (or reference) signal with an output signal from the probe, we call our technique lock-in accelerometry. However, in our case we can excite the system by a non-periodic vibration as could be expected in the case of earthquakes.

An important property of our lock-in method is that its results do not depend on changes in the relative orientation of the accelerometers caused by fixed misalignment between *Ref* and *Probe*. Also the correlation is not affected by slow

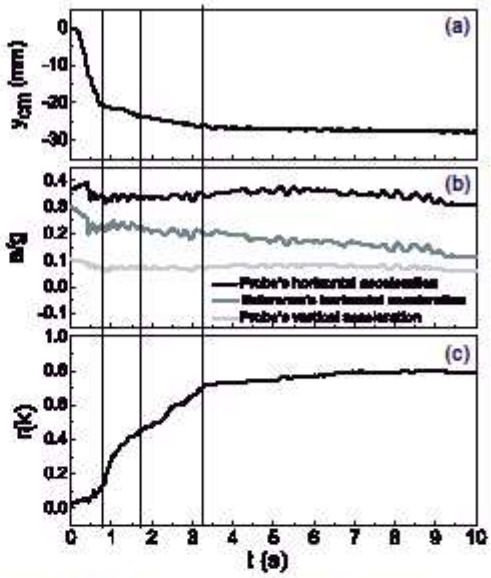

FIG. 2. Time evolution of (a) penetration depth of the center of mass, (b) normalized accelerations, and (c) correlation coefficient for a quasi-2D experiment.

rotations of the intruder. Both statements are confirmed in Ref. 17.

Figure 2 summarizes the main results from one sink experiment.

Figure 2(a) shows the time evolution of the penetration depth of the center of mass of the intruder, measured from a video recorded with the camera. Different stages are clearly identified. After an initial process of fast sinking, that takes around 1 s, the velocity of penetration decreases, and after around 4 s, a slow "creep" process takes place. After approximately 8 s, the sinking process ends as the intruder is confined by the "jammed" granular phase near the bottom of the cell.

In Figure 3(b), three accelerations are shown simultaneously: the horizontal acceleration, $a_{x,R}$, measured by the reference sensor (dark grey central line), the horizontal acceleration, $a_{x,P}$, measured with the probe sensor (black, upper line), and the vertical acceleration, $a_{y,P}$, measured by the probe sensor (light grey line, at the bottom). It is easy to see that the latter shows no evident features allowing us to follow the sinking process.

Finally, Figure 2(c) shows the time evolution of the correlation coefficient, $r(k)$, calculated by Eq. (1) for $D = 70$. It is easy to see that the value of r reflects the main stages shown in Fig. 2(a): fast penetration between 0 and approximately 3 s, and "creep" motion between 3 s and approximately 8 s (a more detailed interpretation of the correlation curve will be the subject of future work).

In order to test our method in a 3D system, sink experiments were performed on a 3D printed cylinder of 44 mm diameter, 10 mm height (external dimensions), and 19.5 ± 0.5 g

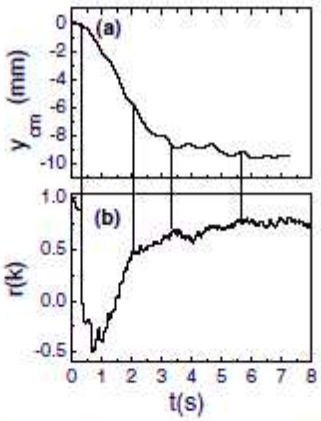

FIG. 3. Time evolution of the (a) penetration depth and (b) the correlation coefficient between the accelerometer of reference and the probe one in a 3D experiment.

of mass—of effective density 1.28 g/cm^3. It was released in the upright position on the free surface of a granular bed contained into a box of 25 × 25 cm^2 base and 40 cm height, filled with polystyrene spheres of 80 μm diameter (monodisperse within a 1%) and a bulk density of 1.05 g/cm^3 (Ugelstad spheres[18]). The box was horizontally shaken with an amplitude of 1.4 ± 0.1 cm and a frequency of 2.75 Hz. One accelerometer was fixed to the box, and the other to the sinking cylinder. The correlation between both was calculated during the sinking process, while the top of the cylinder (that never entered the granular bed) was observed, in the same spirit of the Hele-Shaw experiment previously described. Here, the accelerometers where Analog Devices ADXL345 (Ref. 19) and the data were acquired by Arduino 2009 boards (Ref. 20).

The results of the experiment are shown in Fig. 3. Figure 3(a) shows the penetration depth as function of time in the 3D experiment as determined from the video. It is possible to see two stages in the process. First a fast sinking, followed by a slower process until, finally, the depth stays constant.

Figure 3(b) shows the time evolution of the correlation coefficient between the accelerometers located into the intruder and the reference attached to the container in the same experiment. The beginning of time was taken before the start of the oscillations, and coincident with the origin in Fig. 3(a), when the correlation coefficient is 1 because both accelerometers are at rest. We selected $D = 40$ in Eq. (1) (see Ref. 17 for a discussion about its influence on the results).

It is easy to see a steep decrement of r as soon as the oscillations start: it indicates that the intruder moves freely in the first moments, almost uncorrelated with the granular medium. Then, the intruder sinks fast during approximately the first 2 s. As depth increases, it slows down probably when it reaches the "jammed" granular phase, and the correlation increases until approximately 0.8, where it stabilizes. This curve also shows steps with different slopes, related with the two regions in Fig. 3(a).

In summary, we have demonstrated that our method is able to determine the time interval of sinking of an intruder into shaken granular beds for both quasi-2D and 3D systems. Further insight into the dynamics could be attained by studying the maximum normalized cross correlation between the accelerometers in time, and the phase lag between an intruder at different depths, and the granular surface.

In the present contribution we have studied dry materials, but the technique can also be used for wet granular matter. Finally, substituting the intruder by a solid rock and the granular bed by actual soil may expand the technique to measure, *in situ*, the rheological response of a soil during an earthquake.

We acknowledge support from Project 29942WL (Fonds de Solidarité Prioritaire France-Cuba), from the EU ITN FlowTrans, and from the Alsatian network REALISE.

[1]N. N. Ambraseys, "Engineering seismology," Earthquake Eng. Struct. Dyn. **17**, 1–105 (1988).
[2]National Research Council, *Liquefaction of Soils During Earthquakes* (National Academy Press, Washington, DC, 1985).
[3]C. Y. Wang and M. Manga, *Earthquakes and Water* (Springer, Berlin, Heidelberg, 2014).
[4]J. B. Berril and R. O. Davis, Soils Found. **25**, 106–118 (1985).
[5]E. Clement and J. Rajchenbach, Europhys. Lett. **16**, 133 (1991).
[6]I. Sánchez, G. Gutiérrez, I. Zuriguel, and D. Maza, Phys. Rev. E **81**, 062301 (2010).
[7]M. J. Niebling, E. G. Flekkøy, K. J. Måløy, and R. Toussaint, Phys. Rev. E **82**, 051302 (2010).
[8]M. J. Niebling, E. G. Flekkøy, K. J. Måløy, and R. Toussaint, Phys. Rev. E **82**, 011301 (2010).
[9]T. Shinbrot and F. J. Muzio, Phys. Rev. Lett. **81**, 4365 (1998).
[10]F. Pacheco-Vázquez, G. A. Caballero-Robledo, J. M. Solano-Altamirano, E. Altshuler, A. J. Batista-Leyva, and J. C. Ruiz-Suárez, Phys. Rev. Lett. **106**, 218001 (2011).
[11]H. Torres, A. González, G. Sánchez-Colina, J. C. Drake, and E. Altshuler, Rev. Cubana Fis. **29**, 1E45 (2012).
[12]R. Zimmermann, L. Fiabane, Y. Gasteuil, R. Volk, and J.-F. Pinton, New J. Phys. **15**, 015018 (2013).
[13]E. Altshuler, H. Torres, A. González-Pita, G. Sánchez-Colina, C. Pérez-Penichet, S. Waitukaitis, and R. Cruz, Geophys. Res. Lett. **41**, 3032 doi:10.1002/2014GL059229 (2014).
[14]G. Metcalfe, S. G. K. Tennakoon, L. Kondic, D. G. Shaeffer, and R. P. Behringer, Phys. Rev. E **65**, 031302 (2002).
[15]See www.freescale.com/zstar for details of MMA7660FC ZSTAR3 accelerometer.
[16]F. Kutgiri and J. Glazebrook, Proc. Natl. Acad. Sci. U.S.A. **100**, 10842 (2003).
[17]See supplementary material at http://dx.doi.org/10.1063/1.4902979 for computations which show, based on Eq. (1), that the correlation between *Ref* and *Probe* is almost unaffected by misorientations or slow rotations of the accelerometers.
[18]R. Toussaint, J. Akselvoll, E. G. Flekkøy, G. Helgesen, and A. T. Skjeltorp, Phys. Rev. E **69**, 011407 (2004).
[19]See www.analog.com/static/imported-files/data-sheets/ADXL345.pdf for details of the accelerometer ADXL345.
[20]See www.arduino.cc/en/Main/arduinoBoardDuem for details of the Arduino 2009 board.

4.2 Supplementary information.

4.2.1 L. Alonso-Llanes, G. Sánchez-Colina, E. Martínez, A. J. Batista-Leyva, R. Toussaint and E. Altshuler, accepted on Revista Cubana de Física (2016).

Intruder penetration into Granular matter studied by lock-in accelerometry.

L. Alonso-Llanes[a], G. Sanchez[a], E. Martinez[a], A. J. Batista-Leyva[b], R. Toussaint[c] and E. Altshuler[a*].

a- Group of complex systems and statistical physics, Physics faculty, University of Havana, 10400 Havana.Cuba.

b- Instituto superior de tecnologias y ciencias aplicadas (INSTEC), 10400 Havana Cuba.

c- Institute de Physique du Globe de Strasbourg (IPGS), Ecole des Sciences de la Terre (EOST), Universite de Strasbourg/CNRS. 67084, Strasbourg, France.

* Correspondent author.

Abstract.

Understanding the penetration dynamics of intruders in granular beds is relevant not only for fundamental physics, but also for geophysical processes and construction on sediments or granular soils in areas potentially affected by earthquakes. In this work, we use lock-in accelerometry to study the penetration of intruders into quasi-2D granular matter fluidized by lateral shaking. We observed that there are two well-defined stages in the penetration dynamics as the intruder sinks into the granular material.

Keywords. 45.70.-n, 45.70.Mg, 07.07.Df, 07.50.Qx.

By applying an external oscillatory force is possible to find a transition from a solid phase to a fluidized one in a granular media (Duran, 1999). Such effect provoke the loss of strength of the material and causes an object laying on its surface to sink laterally (Duran, 1999). This fluidization has a destructive effect during earthquakes because the building on its surfaces loss

stability and eventually collapse (Ambraseys, 1988) (Council, 1985) (Wang, 2014). Although earthquakes cannot be forecasted, the after-effects can be reduced (Ambraseys, 1988). In this paper we propose an experimental technique aiming to understand the effects of fluidization in order to reach those objectives.

While in quasi-2D systems the penetration of an intruder can be followed by means of a video camera (Sanchez, 2010) (Niebling, 2010), in the case of 3D systems of no transparent grains this is not possible. Wireless accelerometry has been used in a few occasions to quantify, as far as we know, the sink dynamics of an intruder (Goldman & Umbanhowar, 2008) (Seguin, 2013) (Umbanhowar, 2010) (Pacheco-Vazquez, Caballero-Robledo, & al., 2011) (Altshuler, 2014). In this note we use a method called Lock-in accelerometry (LIA), previously reported by our group in order to circumvent those problems (Sánchez, 2014). As a result we are able to establish two well-defined stages in the dynamics of penetration of an intruder into shaken granular matter, as the penetration depth increases.

The figure 4.1 shows the experimental setup with consists in a Hele-Shaw cell with a gap of 21.4 +/- 0.2mm filled up with polidisperse spherical particles with 0.7 +/- 0.1mm of average size and effective density of 0.715g/cm^3. At the bottom of the cell there is a horizontal hose with 30 holes of 0.5mm diameter each through which is possible to inject air into the granular

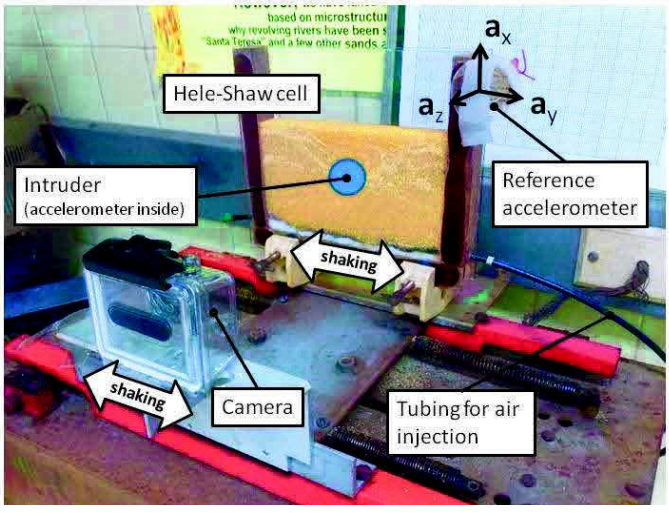

Figure 4.1 Experimental setup for quasi-2D measurements. Both, the Helle-Shaw cell and the camera are synchronously shaken in the lateral direction.

system. The cell is able to oscillate laterally using an electromagnetic shaker with an amplitude of 1.5cm and a maximum frequency ν = 6Hz. Released on the granular system there is an intruder, a squared parallelepiped 40 +/- 0.3mm side, 17 +/- 0.3mm thickness, and a weight of 51 +/- 1g, whose sinking is followed by a digital camera Hero2 that moves synchronously with the Hele-Shaw cell. Finally two three axis wireless accelerometers are fixed to the Hele-Shaw cell (labeled Ref) and inside of the intruder (labeled probe) (Freescale semiconductor, 2009).

A typical experiment consists in injecting air into the granular system for 10 seconds ensuring the same initial conditions. Later is released the intruder (with the probe accelerometer inside) on the free surface of the bed. Then the data acquisition is activated from the camera and accelerometers and finally the electromagnetic shaker and the air injection systems are started at the same time until the sinking process ends.

The essence of the technique LIA is the combined use of the information from the accelerometer fixed to the Hele-Shaw cell (Ref) and from the accelerometer inside the intruder (Probe). Then, the experimental parameter used to study the sinking process is the correlation between the horizontal accelerations from both accelerometers. For that it is used a modification of the Pearson's correlation coefficient aimed at decreasing the noise in the output that consist in calculating the evolution of the Pearson's coefficient within time intervals of size D, each one starting at moment K, as follows:

$$r_{(k)} = \frac{\sum_{i=k}^{k+D} a_{xR}(i) a_{xP}(i)}{\sqrt[2]{\left[\sum_{i=k}^{k+D}\left(a_{xR}(i)\right)^2 \sum_{i=k}^{k+D}\left(a_{xP}(i)\right)^2\right]}} \qquad (4.1)$$

Were a_{xR} and a_{xP} represent the horizontal accelerations of the reference and the probe, respectively, i represents the sampled time index and N is the total of the experiment's data points (k runs from 1 to N-D).

The key idea behind this technique is when the intruder is sinking it will be a delay between a_{xR}, a_{xP} and the correlation coefficient will be smaller than one. As depth increases the correlation increases as the intruder with the probe approaches the jammed phase into the granular system. Finally the value of the correlation must reach a plateau close to 1 indicating the end of the sinking process, were the intruder is moving synchronously with the reference.

The figure 4.2 shows the curves of a) the penetration depth of the center of mass and b) correlation coefficient versus time for an experiment with frequency of 2.5 Hz and air flux of 800cm^3/h. The figure 4.2a shows the penetration depth of the center of mass in time obtained by the image processing from the videos taken by the digital camera. The general behavior of the sinking may be characterized, fundamentally, by three stages: initially there is a fast sinking process which takes around 1s, then a decrease in the sinking velocity and after 5s a creep process takes place until the final stop. The figure 4.2b shows the time evolution of the correlation coefficient calculated using Eq. (1) with D = 30. The first region in the correlation curve couldn't be measured due to technical limitations of the accelerometers. In t = 0, as reported for the case of the 3D experiment, the correlation should be 1 because both accelerometers are at rest. Then will have an initial fast-decrease in the correlation because in the initial moments, probe and reference has a delay in its horizontal accelerations as was discussed briefly above. Later there is an increase of its value as a result of the arrival of the intruder to a region in the system in which it starts to move together with the granular mass. Finally the correlation remains at a saturation value until the end of the experiment.

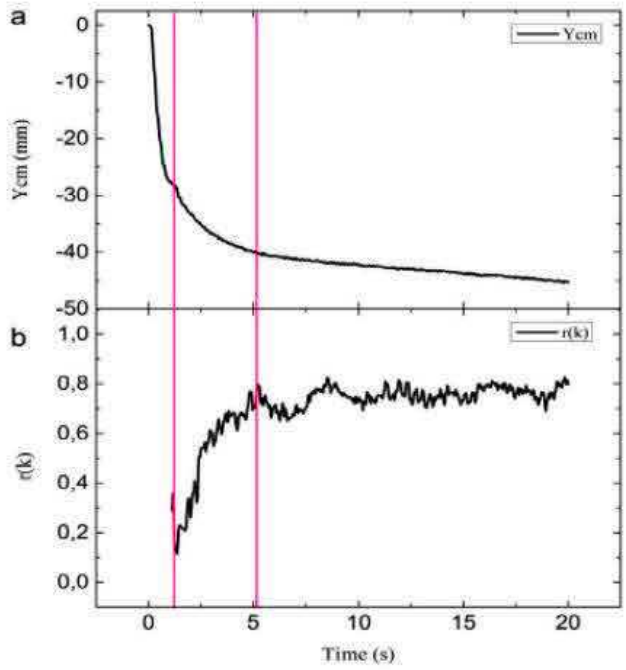

Figure 4.2 a- Penetration depth of the center of mass of the intruder versus time obtained from the video processing. b- Correlation coefficient versus time.

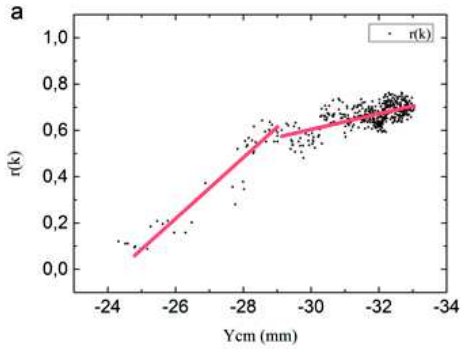

Figure 4.3a Correlation coefficient versus penetration depth of the center of mass for 2.5Hz and 800cm3/h.

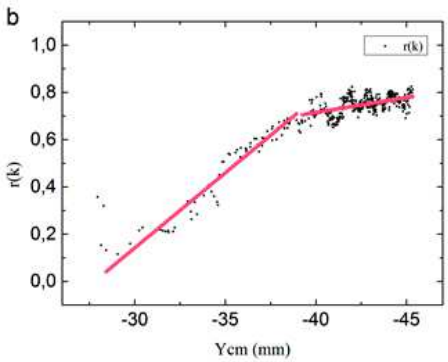

Figure 4.3b Correlation coefficient versus penetration depth of the center of mass for 2.5Hz and 700cm3/h.

The figure 4.3 shows the correlation coefficient as a function of the penetration depth of the center of mass for experiments with a) frequency of 2.5Hz and air flux of 800cm^3/h and b) frequency of 2.5Hz and air flux of 700cm^3/h were it is visible the influence of the air flux in the granular system. With the help of the guide lines is possible to identify two main regions in each experiment, one between 29mm and 39mm of depth and the other from 39mm to 45mm of depth in the figure 4.3a and in the figure 4.3b, one between 25mm and 29mm of depth and the other from 29mm to 33mm of depth. In the case of figure 4.3a those regions match with the two regions after the first guide line in figure.4.2. The previous curves represent the experimental proof of the technique's basis and may be useful as a calibration function to characterize the variation of the penetration depth of the center of mass of the intruder in the time from the temporal dependence of the correlation.

In the present contribution we have studied dry materials, but the technique can also be used for wet granular matter. Finally, substituting the intruder by a solid rock and the granular bed by actual soil may expand the technique to measure, in situ, the rheological response of a soil during an earthquake.

This work was supported by the Project 29942WL (Fonds de solidarite prioritaire France-Cuba), from the EU ITN FlowTrans and from the Alsatian network REALISE.

CHAPTER 5 Ad hoc techniques involving miniature sensors for the study of sink dynamics.

One of the targets of this thesis is the development of devices to be embedded into the intruders used in penetration experiments. They must be affordable, and maintainable by researchers not necessarily trained in electronics.

Most of the semiconductor companies offer development tools for their microcontroller lines of production. The platform *Arduino* appeared to be the most suitable to fulfill the goals of the thesis due to:

1. Good price-performance ratio
2. Open source both for hard and software
3. A great community of skilled users available on the WEB

5.1 What is Arduino?

Arduino was created in the Interaction Design Institute Ivrea, Italy, for the teaching courses on interaction design for physical devices in 2005.

The creators, Massimo Banzi, with David Cuartielles, Gianluca Martino wanted the designers to be able to build without depending on electronics experts. (Severance, Jan. 2014)

Taking a programming language from MIT called *Processing*, meant to teach software design to artists, they make it run on a microcontroller. This is where the idea of a software sketchbook originated. The first version of Arduino was based on Hernando Barragán's Wiring project, reusing the Wiring APIs and simplifying the hardware. As an additional benefit of his wiring inheritance and one of the main reasons for the Arduino success is that the same software is available for use on Microsoft Windows, Apple Mac OS, or Linux. This is due to Java, designed to be quite platform-independent. The Arduino software provides a complete Java environment. It is licensed under the GPL version 2. All that resulted in a device with a microcontroller and

all the associated circuits that releases the user of the job of re-designing the generic parts each time a new project is done: the user simply uploads the code, plugs the board in, and gets a working hardware. In 2005, Tom Igoe started using it in his physical design classes at New York University, contributing to the wide spreading of the platform. (Severance, Jan. 2014).

The smallest Arduino's configuration is a board with a microcontroller, an Atmega328 (Atmel Corporation) in the most popular versions, a ceramic's or quartz system's clock, a regulator to adapt the power level to the chip rating of work and an additional USB-TTL bridge, to connect the card to the IDE or serial terminal on the host computer. (Russell, 2010).

5.2 The Arduino Integrated Design Environment (IDE).

The Arduino interface development environment (IDE) contains an editor where the code is edited or inserted, a compiler who customizes that code for the specific chip and links in the library modules (Margolis, 2011). The set of applications that regulate the building and uploading (writing) process are known as *tool-chain* in microcontroller's argot. All together is wrapped into the IDE. The outcome of the compiled code is a Microsoft binary HEX file. The program AVRDude, integrated under the cover of the IDE, manages the uploading procedure between the compiler and the programmer. The compiler is a variant of GNU C/C++ for Windows or Linux-Mac, depending on the environment.

The programmer is a USB-TTL bridge (FTDI Ltd) included by default in most Arduino cards. Some compact versions of Arduino, like the Arduino-mini, allow separating the programmer, as the board is supposed to remain embedded inside some apparatus. The smart part of the programming work is through a code, the Boot Loader, preloaded in the Program Memory that rules the writing on himself. The Boot Loader can use any available data interface with the associated protocol to read and write code into the flash memory.

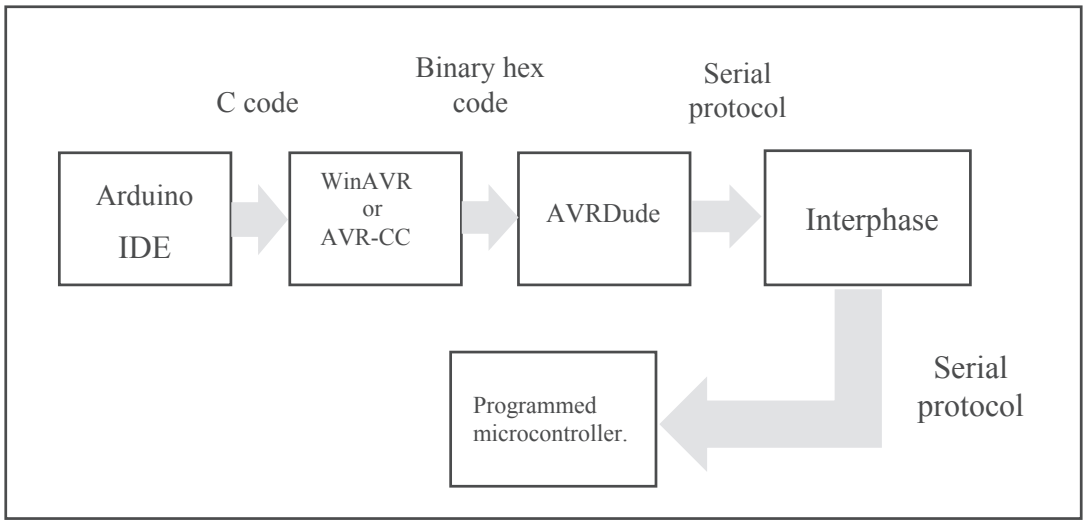

Figure 5.1. Arduino programming environment.

The Atmel's AVR family of micro-controllers have three memory spaces: a SRAM Data Memory, a FLASH Program Memory and an EEPROM Memory. The Atmega328p (the one used by Arduino UNO), has 32Kbytes of reprogrammable Flash memory organized as 32K x 16. The program memory is divided into Boot Loader section and Application Program Section. Atmel warrantees an endurance of 10,000 r/w cycles for the Flash memory. (Atmel Corporation)

There are several external clock sources to choose. The Atmega328p is shipped by default with the internal RC oscillator at 8MHz, pre-scaled to deliver a 1MHz system clock. At the maximum operating (Vdd) voltage, the chip runs at 20MHz. Arduino is intended to run at 8 or16MHz. To stay Arduino-compatible, the system will work at 16MHz, powered with 3.3V, to simplify the interface with the chosen sensors.

For the connection of the peripherals, sensors and data logging devices, the Atmega328p uses three ports with a total of 23 pins. Each port pin in the Atmega328p can be directed by changing the drive value (if output) or enabling/disabling the pull-up resistors (if input).

Most of the pins can enable alternate functions through a multiplexer featuring the essential functions to cope with the system's peripheral. For the data interface and associated protocols, the following functions are available:

a) SPI: Serial Peripheral Interface.
b) USART: Universal Synchronous and Asynchronous serial Receiver and Transmitter.
c) 2-Wire: Serial Interface compatible with Philips' I2C protocol.

The ATmega328p features a 10-bit successive approximation ADC. The ADC is connected to an 8-channel Analog Multiplexer which allows eight single-ended voltage inputs constructed from the pins of Port A. The single-ended voltage inputs refer to 0V (GND).

Nevertheless, the Atmega328p is mentioned as the Arduino generic microcontroller, there are other Atmel's AVRs and ARMs chips, implemented in Arduino's boards. For the purposes intended for the measurement system in this thesis, the Atmega328p is perfectly compliant.

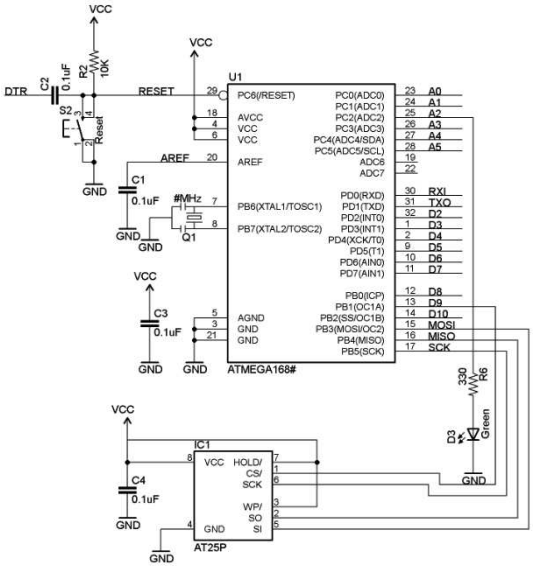

Figure 5.2. A basic Arduino's schematic.

On the Figure 5.2 the big, block at the center is the micro-controller, an Atmega168. The smaller block at the bottom left is a generic memory connected to the ISP port. The serial TTL voltage level communication would go through the RXI, TXO pins, and the A4-A5 pins implements the Two-Wire communication port.

5.3 System's details.

The specifics of the device are described in the following parts. First a general description of the core is presented and then, individually the approaches of data capture and logging will be detailed.

The Arduino was built on a 400 mm x 200 mm QFP32 to DIP adapter plate with the minimum parts to make it functional. This is the core around the other system's components changed to adapt the design to the particular experiment. In the Arduino used in this thesis, the USB-TTL bridge is not included, because once the program is uploaded, the bridge is not needed if the data is not to be directly transferred to the host through USB.

There are four particular cases with the corresponding Arduino's configurations. To each configuration correspond a particular program, driving the specific sensor or data recording device.

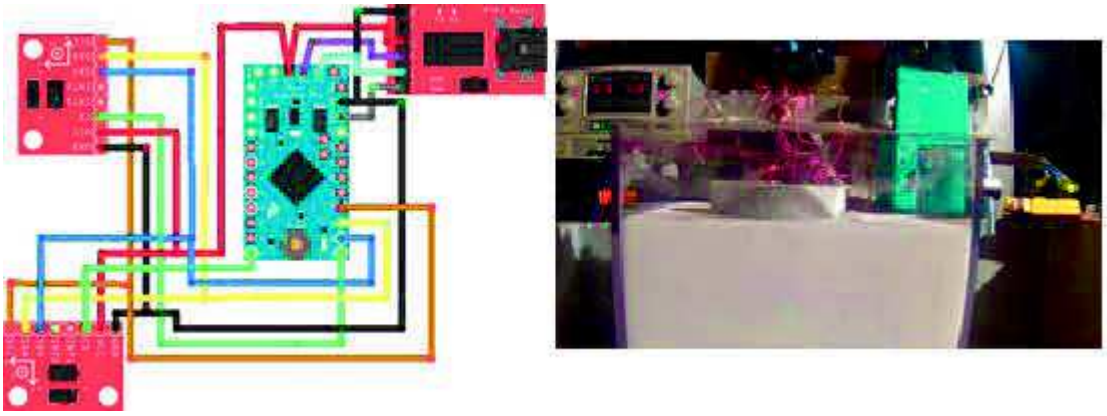

Figure5.3 Arduino wiring to measure online, to the right, an experimental setup with the wired intruder.

In the Figure 5.3, on the left is a simplified wiring schematics of an Arduino configuration including two accelerometer cards (to the left of the scheme). The central card is the Arduino itself, and the card at the right corner is the USB-TTL bridge. Right panel: The actual wired configuration mounted in a way similar to the lock-in accelerometry technique described in Chapter 4, now in a 3D granular bed.

5.4 On-line data acquisition.

This is the simplest configuration: the Arduino is connected to the host computer via the USB bridge, from where it takes the power while transfers the data (on page 91).

In this experiment, a regular Arduino Duemilanove board (Russell, 2010) is used, to which two 3D digital accelerometers were connected. Following the disposition used in the Lock-in experiment, one sensor was fixed to the experimental cell, while the other stood inside a hollow intruder (a pill-box cylinder in the picture of Fig. 5.3). Both sensors were connected to the Arduino by flexible enameled cables to avoid disturbing the free movement of the penetrating intruder. The power on the Duemilanove board was set to 3.3 V to agree with the maximum operating voltage of the accelerometers. The Atmega328p is designed to run safe keeping the clock frequency unaffected by the Vdd level in the operating range.

The sensors were Analog Device's ADXL345 (Analog Devices, Inc) with 3 axis output data 12 bit wide MEMS programmable accelerometers. In the Arduino's code they were set up for the scale of +/- 1g, at a rate of 1000 samples/s 3D. They used the SPI port with separated chip select lines.

The main code after the setup, runs a loop measuring and sending sequentially the data of both sensors to the host, where a serial terminal logged it out to a file at 36400 BPs.(on page 93)

5.5 Data logging to an external memory.

Some of the experiments require a complete freedom of movement of the intruder. For this objective it is reasonable to log the information in a rewritable data media, like Flash memories, Ferroelectric Static RAM (FRAM), or micro-SD cards. In this section will be described the design of a data logger with a FRAM. That memory has much better access speed than the Flash or the micro-SD, with the cost of a reduced data capacity. For this setup was used an MBR25r256 Fujitsu's FRAM memory, because there is an Arduino's shield already available with libraries included. This FRAM has a capacity of 256 Kbit or 32K x8 (Fujitsu, 2013).

The system is devised with the Arduino core set to run with 3.3 V, with two extra cards, one for the sensor, other for the FRAM. Both peripherals were connected to the Arduino by the TWO-Wire (aka IIC or I^2C) port. In this case, the sensor was an Invensense's MPU6050 (InvenSense, Inc.) Inertial Measurement Unit (IMU), well known because it has been long used for drones, robotics and other movement capture projects. This Micro Electro Mechanic Sensor (MEMS), as the ADXL345, has a 3D accelerometer, now enhanced with a 3D gyroscope and a digital processing CPU, all reprogrammable and 16 bits data wide. In the selected configuration the IMU delivers 3 axis acceleration and 3 axis angle rate data is a +/- 2g range and 1000 deg/s ranges at 1000 data samples/s 6D. As the writing speed of the FRAM is of 130 ns/byte, the data rate of the data logger is limited by the sensor's speed, not by the memory. (Thanigai, 2012)

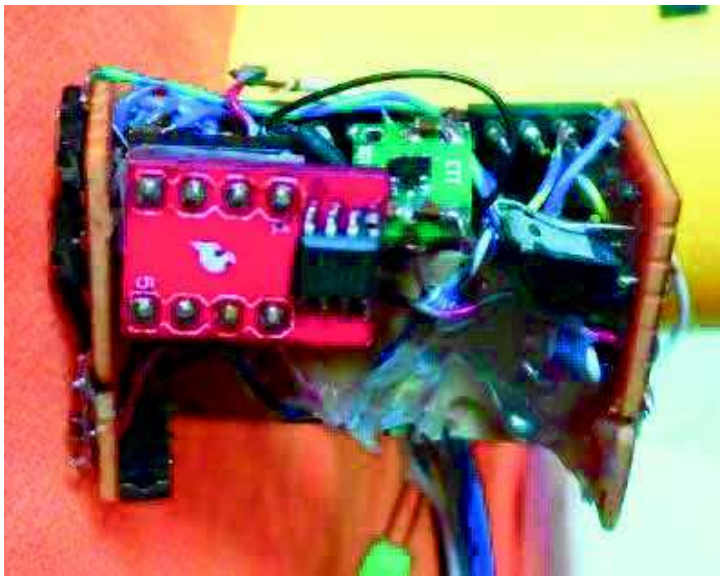

Figure 5.4 A wired prototype with FRAM memory and IMU. The horizontal length of the device in the figure is approximately 40 mm.

The program, after the setup section, runs in an infinite loop, taking groups of 6D measurements and writing it to the FRAM. There are three conditions to be checked for the loop to keep running: if the memory is full, if the pin D7 is HIGH, or if the system is reset. If any of them is met, the program gets out of the measuring loop.

5.6 Data logging to an micro-SD card.

When a rock with a sensor inside is left to the tide and waves in the seashore, in addition to autonomy, you will need a recording medium with great capacity. For such a case, in the configuration is inserted a micro-SD card with 2Gbyte capacity. The micro-SD card interfaces to the Arduino through the SPI port. The information is recorded in a TXT file thanks to a special library allowing the creation of a File Allocation Table (FAT) in the card. This has the great advantage of allowing to write the formatted data to a file.

The marine environment harms seriously the electronics, so it is vital to keep at the minimum the physical access to the data logger during measurement. To this purpose two controls were arranged out of the board: a reset, and a stop of recording. The reset is the standard Arduino's reset pin; the stop function is implemented by requesting the logic state of the pin D7 in every cycle. If the reset is on, a new file is initialized in the SD card. Systematically, a default file name and an order numbering identifies the experiment. (on page 93)

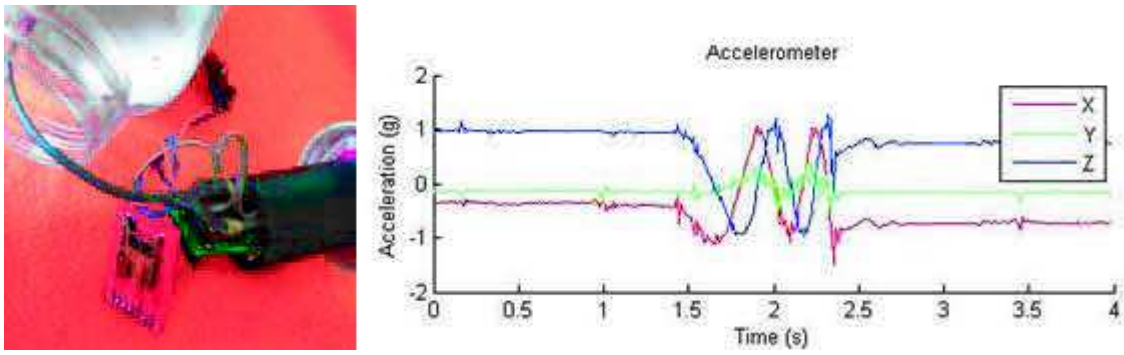

Figure 5.5 Simulating the roll-over of a rock with a pill's bottle equipped with an Arduino data logger.

In the figure 5.5, left, a standard pill bottle is used as an "artificial rock" to test the performance of an Arduino equipped with a gyroscope + accelerometer sensor, and a SD card socket. Right panel: Three-axis acceleration record of the "artificial rock": during the first 1.5 seconds, the system is at rest. Then, it is pushed and released, so during the next second it performs two full turns. Finally, it is again at rest for the last 1.5 seconds, approximately.

For this configuration, the sensor is an Invensense's MPU6050 IMU, the same used for the FRAM's data logger. The sensor's data rate depends on the setting for the acceleration's and

angle's rate ranges, but the writing speed for the micro-SD card is much slower than for the FRAM. To check the real data logging speed a test program was run, that toggled a pin on the Arduino after every measurement–log in cycle. Through the switching frequency of the pin, a mean data logging rate of 48Hz was measured. This is an averaged assessment, as the writing speed depends on the length (bytes) of the data. (on page 95)

5.7 Wireless data acquisition.

For measuring and data logging directly to a file in the host computer there is an alternative to the "brute force" wired method described in the first configuration. This alternative is the wireless data logging. There are several ways to wireless data capture, from the simple radio frequency toy modules, to the sophisticated ZigBee in the 2.4GHz radiofrequency band. We choose an in-between possibility: the NRF24L01 (Nordic Semiconductor ASA). It is a transceiver module with several code examples and libraries available in the WEB.

Figure 5.6 Arduino on the rocks. An actual seabed rock perforated to be loaded with an Arduino data logger.

On the Fig. 5.6 the left panel: an actual marine rock removed from a sandy bottom at "Santa María" beach in Havana in which a hole has been drilled. On the rock, an Arduino equipped with the gyroscope-accelerometer sensor, and a Bluetooth module is shown (the picture includes the battery holder and the battery, separately). Right panel: the electronics is shown almost completely inserted into the rock. In order to protect it from the water, it must be sealed into a plastic bag. As in the FRAM and the micro-SD systems, the sensor is an Invensense's MPU6050 MEMS IMU. The transceivers were interfaced to the Arduino by the SPI port. (on page 96) (on page 97)

The host PC normally does not come with this kind of transceiver device, it is not compatible to the standard Bluetooth, and hence for the data to be recorded to a file, a second Arduino with an additional transceiver must be programmed in order to play the role of a hub connected to the PC. This allows to receive the data of more than one sensor sequentially, as in a Wireless Sensors Network (but the multiple-sensor possibility has not been explored by the author yet).

The data transfer from the hub to the host PC can be configured to the standard 115 Kb/s of serial modems, which is good enough, although the maximum data rate for this configuration depends on the sensor's rate.

Table 5.1 displays a comparison between the main performances of the three data logger prototypes. The performance is labeled by the numbers 1, 2 and 3, where the order goes from the best to the worst for the behavior of the sensor in the specific area. Note that *Capacity* means storage capacity, *Speed* means data sampling velocity, *Autonomy* means energy efficiency and *Size* means physical size, where smaller is better.

Table 1Comparison of the performances of data storage devices.

Comparison of the performance of data storage devices.				
	capacity	speed	autonomy	size
Wireless	1	2	1	2
Micro-SD	2	3	3	2
FRAM	3	1	2	1

Finally, it is worth comparing the performance of the Arduino-based system with the wireless accelerometers based on the Zigbee platform used in earlier chapters in this thesis. There are a number of advantages of the Arduino based systems:

a) The accelerometer embedded in the Freescale-Zigbee sensors are analog, while the ones implemented in the Arduino system, are digital –no analog-to-digital conversion is needed in the latter.

b) The details of the hardware of the Freescale-Zigbee system are not available, and the software needs a special tool to connect with the hardware, while Arduino is fully open.

c) The Freescale-Zigbee system has a maximum speed for data acquisition of 120 Hz, while the Arduino-based systems designed in this thesis can sample data as fast as 1 kHz (the use of the micro-SD memory significantly decreases the sampling rate).

Conclusions and perspectives.

In the present thesis, the penetration of intruders into fluidized granular matter has been studied using optical and miniature accelerometric techniques, some of them created *ad hoc*.

In particular, the author has been able to:

a) Determine the influence of the kind of basement in the behavior of a cylinder used as a model of a human construction or a rock, when it penetrates a vibrofluidized granular bed: flat bottom cylinders tend to sink vertically, while ring-bottomed ones tend to tilt laterally –although the latter behavior tends to dominate for very strong lateral shakings. This study may help understanding the structural damage to man-made structures occurring during earthquakes and other natural catastrophes.

b) Establish the influence of gravity in the sinking of a spherical intruder into light granular matter, measured by wireless accelerometry: the total sink depth is independent from the gravity, while the total sink time increases as the inverse of the square root of the gravity. This may shed light on how to design rovers to move on sandy surfaces of different planets and asteroids, and may be useful to interpret geomorphological data from those astronomical bodies.

c) Create the so-called “Lock-in accelerometry” technique, to study the slow penetration of an intruder into vibro-fluidized granular matter when optical and conventional one sensor based accelerometric techniques are not applicable. The technique can be developed to get data during natural catastrophes where soil fluidization is present.

d) To implement an open-core and open-software Arduino-based platform to study the behavior of intruders into fluidized granular matter both in laboratory and in natural conditions. In particular, a detailed evaluation of different storage systems was performed. The platform was preliminarily tried to get accelerometric data from rocks moving on the bottom of an actual sand beach –a scenario relevant to erosion dynamics.

Several (non exhaustive) perspectives of this work can be envisioned:

The development of light integrated embedded accelerometers and gyroscopes, equipped with data loggers, allows to plan a campaign aimed at studying the erosion of beaches, as for example on the Cuban ones strongly submitted to erosion. Equipping rocks of different sizes, densities and shapes should allow to study their dynamics during several sea conditions on beaches. Together with large scale measurements based on stereophotogrammetry performed on images acquired by unmanned quadcopters, this should allow to progress on the understanding of the dynamics of saturated granular media associated with the erosion processes. The accelerometers can be distributed in superficial highly mobiles rocks, and can be distributed at larger depth to monitor the tilt associated with slow beach creeping.

The same types of accelerometers can also be deployed in intruder along river banks to assess their stability, or in slowly moving landslides. Indeed, rockfalls and landslides are among the main hazards in Europe, and are such are of large societal interest. The low cost of the platform developed should allow to deploy arrays of sensors in the zones of interest.

Researches prolonging the study of friction in dry oscillating granular materials can also be extended to partly or fully saturated ones. Indeed, the presence of water often deeply impacts the ability of soils to liquefy during earthquakes or heavy rainfall.

Another related topic, where sensors could be coupled to autonomous oscillating devices, is the study of quicksands. This mesmerizing phenomenon is so far lowly studied in situ. Coupling accelerometers + gyroscopes embedded devices with an autonomous oscillation source in intruders could allow to probe in situ the rheology of quicksand in the regions where these naturally arise.

References

Albert, R., Pfeifer, M., Barabasi, A. L., & Schiffer, P. (1998). Slow drag in a granular medium. *Phys. Rev. Lett., 82*, 205.

Almeida, M. P., Parteli, E. J., & als. (2008). Giant saltation on Mars. *105*, pp. 6222–6226. Proc. Natl. Acad. Sci. U.S.A. doi:10.1073/pnas.0800202105.

Altshuler, E. H.-P. (2014). Settling into dry granularmedia in different gravities. *GeophysicalResearchLetters, 41*, 3032–3037. doi:10.1002

Ambraseys, N. (1988). *Earthquake Eng. Struct.Dyn., 17*(1).

Analog Devices, Inc. (n.d.). *http://www.analog.com/en/products/mems/mems-accelerometers/adxl345.html#product-overview.* Retrieved july 14, 2016, from http://www.analog.com/: http://www.analog.com/media/en/technical-documentation/data-sheets/ADXL345.pdf

Aspaugh, E. (2007). The shifting sands of asteroids. *Science, 316*, 993-994. doi:10.1126/science.1141971.

Atmel Corporation. (n.d.). *http://www.atmel.com/devices/atmega328.aspx.* Retrieved july 14, 2016, from http://www.atmel.com/devices/atmega328.aspx: https://www.atmel.com/images/Atmel-8271-8-bit-AVR-Microcontroller-ATmega48A-48PA-88A-88PA-168A-168PA-328-328P_datasheet_Complete.pdf

Berrill, J. B., & Davis, R. O. (1985, June). Energy dissipation and seismic liquefaction of sands: revised model. *Soils and foundations , Vol 25*(No. 2), 106-118.

Boudet, J. F., Amarouchene, Y., & als. (2006). Dynamics of impact cratering in shallow sand layers. *Phys. Rev. Lett., 96*(158001-4), 4. doi:10.1103/PhysRevLett.96.158001.

Bray, J. D., & Dashti, S. (2010). Liquefaction-Induced Movements Of Buildings With Shallow Foundations. *International Conferences on Recent Advances in Geotechnical Earthquake Engineering and Soil Dynamics.* San Diego Ca. Abgerufen am June 2016 von http://scholarsmine.mst.edu/icrageesd/05icrageesd/session12/4

Brzinski, T.-A. I., & Durian, D. J. (2010). Characterization of the drag force in an air-moderated granular bed. *Soft Matter., 6*, 3038–3043. doi:10.1039/B926180J.

Chen, L., Umbanhowar, P. B., & als. (2009). Sensitive dependence of the motion of a legged robot on granular media. *106*, pp. 3029–3034. Proc. Natl. Acad. Sci. U.S.A. doi:10.1073/pnas.0809095106.

Ciamarra, M., Lara, A., Golman, D., Vishik, I., & Swinney, H. (2004). Dynamics of drag and force distributions for projectile impact in a granular medium. *Physical review Letters*, 92.

Constantino, D. J., Bartell, J., & als. (2011). Low-velocity granular drag in reduced gravity. *Phys. Rev. E, 83*(011305-4). doi:10.1103/PhysRevE.83.011305.

Council, N. R. (Hrsg.). (1985). Liquefaction of soils during earthquakes.

de Vet, S. J., & de Bruin, J. R. (2007). Shape of impact craters in granular media. *Phys. Rev. E., 76*(041306-4), 4. doi:10.1103/PhysRevE.76.041306.

Dorbolo, S., Ludewig, F., & Vandewalle, N. (2013). Bouncing trimer: A random self-propelled particle, chaos and periodical motions. *Granular Matter., 15*, 033016-033038. doi:10.1088/1367-2630/11/3/033016.

Duran, J. (1999). *Sands, powders and grains, an introduction...* NY: Springer.

Fincham, D. (1992). Leapfrog rotational algorithms. *Molecular Simulation., 8*(165). doi:10.1080/08927029208022474.

Forrestal, M., & Luk, V. (1992). Penetration into soil targets. *Int.J. Impact Eng, 12*(3), 427–444.

Freescale semiconductor. (2009). ZSTAR3 Accelerometer Family Expansion. *ZSTAR3BOARDFS REV.2*. Von http://www.freescale.com/zstar abgerufen

FTDI Ltd. (n.d.). *http://www.ftdichip.com/Products/ICs/FT232R.htm*. Retrieved July 14, 2016, from http://www.ftdichip.com/: http://www.ftdichip.com/Support/Documents/DataSheets/ICs/DS_FT232R.pdf

Fujitsu. (2013). *https://www.fujitsu.com/*. Abgerufen am 14. july 2016 von https://www.fujitsu.com/: https://www.fujitsu.com/us/Images/MB85R256F-DS501-00011-6v0-E.pdf

Goldman, D., & Umbanhowar, P. (2008). Scaling and dynamics of sphere and disk impact into granular media.

Hidalgo, R. C., Kanzaki, T., Alonso-Marroquin, F., & Luding, S. (2013). on the use of graphycs processing units (GPU's) for molecular dynamics simulation of spherical particles. *AIP Conference Proceedings.*, *1512*, S. 169. doi:10.1063/1.4811894

InvenSense, Inc. (kein Datum). *https://www.invensense.com/products/motion-tracking/6-axis/*. Abgerufen am 14. july 2016 von https://www.invensense.com/: http://www.invensense.com/wp-content/uploads/2015/02/MPU-6000-Datasheet1.pdf

Jaeger, M. J., & Nagel, R. J. (1992). Physics of the Granular State. *Science., 225*.

Katsuragi, H. (2012). Nonlinear wall pressure of a plunged granular column. *Phys. Rev. E., 85*(021301-5), 5. doi:10.1103/PhysRevE.85.021301.

Katsuragi, H., & Durian, D. J. (2007). Unified force law for granular impact cratering. *Nature Physics vol3*, 420-423.

Kondic, L., Fang, X., & als. (2012). Microstructure evolution during impact on granular matter. *Phys. Rev. E., 85*(011305-17), 17. doi:10.1103/PhysRevE.85.011305

Liu, L., & Dobry, R. (1997). Seismic response of shallow foundation on liquefiable sand. *J. Geotech. Geoenviron.Engng., 123*(6), 557-567.

Longmore, J. P., Marais, P., & Kuttel, M. (2013). Towards realistic and interactive sand simulation: A GPU-based framework. *Powder Technology., 235*(983). doi:10.1016/j.powtec.2012.10.056.

Luding, S. (1998). Collisions & contacts between two particles. In H. J. Herrmann, J. P. Hovi, & S. Luding, *Physics of dry granular media.* (Bd. E350, S. 285-304). Dordrecht, Germany: Kluwer Academic Publishing.

Margolis, M. (2011). *Arduino Cookbook, Recipes to Begin, Expand, and Enhance Your Projects.* O'Reilly Media.

Metcalfe, G., Tennakoon, S. G., & als. (2002). Granular friction, Coulomb failure, and the fluid-solid transition for horizontally shaken granular materials. *PHYSICAL REVIEW E, 65*, 15. doi:10.1103/PhysRevE.65.031302

Niebling, M. F. (2010). *Physical Review E, 82*.

Nordic Semiconductor ASA. (kein Datum). *http://www.nordicsemi.com/eng/Products/2.4GHz-RF/nRF24L01*. Abgerufen am 14. july 2016 von http://www.nordicsemi.com/eng/: http://www.nordicsemi.com/eng/nordic/download_resource/8041/1/33524214

Obermeier Stephen F. (1996). Use of liquefaction-induced features for paleoseismic analysis. *Engineering Geology*, 76.

Owens, S., Houston, M., Luebke, D., & als. (2008). GPU Computing. *Proc. IEEE., 96*(879). doi:10.1109/JPROC.2008.917757

Pacheco-Vazquez, F., Caballero-Robledo, J. M., & al. (2011). Infinite penetration of a projectile into a granular medium. *Physical Review Letters 106*, 3.

Poschel, T., & Schwager, T. (2005). *Computational granular dynamic, models and algorithms.* Berlin: Springer.

Ruiz-Suarez, J. C. (2013). Penetration of projectiles into granular targets. *Rep. Prog. Phys., 76*, 1–23. doi:10.1088/0034-4885/76/6/066601.

Russell, D. J. (2010). *Introduction to Embedded Systems: Using ANSI C and the Arduino Development Environment.* Morgan & CLaypool.

Sánchez, G. A.-L.-L. (2014). “Lock-in accelerometry” to follow sink dynamics. *REVIEW OF SCIENTIFIC INSTRUMENTS, 85*. doi:10.1063

Sanchez, I. G. (2010). *Physical Review E, 81*.

Sancio, R. B., Bray, J., & als. (2004). Performance of buildings over liquefiable ground in Adazapari,Turkey. *!3th world Conference on Earthquake Engineering.*, (S. Paper 935). Vancouver, CA.

Seguin, A. B. (2013). Experimental velocity fields and forces for a cylinder penetrating into a granular medium. *PHYSICAL REVIEW E, 87*. doi: 10.1103

Severance, C. (Jan. 2014). Massimo Banzi: building Arduino. *Computer, Volume:47*. (IEEE, Ed.)

Shinbrot, T., Duong, N.-H., & als. (2004). Dry granular flows can generate surface features resembling those seen in Martian gullies. *101*, pp. 8542–8546. Proc. Natl. Acad. Sci. U.S.A. doi:10.1073/pnas.0308251101.

Tennakoon, S. G., Kondic, L., & Behringer, R. P. (1999). Onset of flow in a horizontally vibrated granular bed:Convection by horizontal shearing. *Europhys. Lett., 45*(4), 470-475.

Thanigai, P. (2012, july 19). *http://www.embedded.com/.* Retrieved july 14, 2016, from http://www.embedded.com/: http://www.embedded.com/design/mcus-processors-and-socs/4390688/2/FRAMs-as-alternatives-to-flash-memory-in-embedded-designs

Torres, H., Gonzalez, A., & als. (2012). Impact dynamics in “hard” and “soft” granular matter. *Rev. Cub. Fıs., 29*. (E. Altshuler, Hrsg.) La Habana, Cuba.

Tsimring, L. S., & Volfson, D. (2005). Modeling of impact cratering in granular media. In R. Garcia-Rojo, H. J. Herrmann, & S. McNamara, *Powders and Grains* (pp. 1215–1223). Rotterdam: A.A. Balkema.

Uehara, J. S., Ambroso, M. A., Ojha, R. P., & Durian, D. J. (2003). Low-speed impact craters in loose granular media. *Phys. Rev. Lett, 90*. doi:194301

Umbanhowar, P. G. (2010). Granular impact and the critical packing state. *Physical Review E, 82*. doi: 10.1103

Vanneste K. Meghraoui M. Camelbeeck T. (1999). Late Quaternary earthquake-related soft-sediment deformation... *Tectonophysics*, 23.

Verlet, L. (1968). Computer Experiments on Classical Fluids.II. Equilibrium Correlation Functions. *Phys. Rev., 165*(20). doi:doi:/10.1103/PhysRev.165.201.

Walsh, A. M., Holloway, K. E., Habdas, P., & deBruyn, J. R. (2003). Morphology and scaling of impact craters in granular media. *Phys. Rev. Lett., 91*, 104301-4. doi:10.1103/PhysRevLett.91.104301.

Wang, C. M. (2014). *Earthquakes and water.* Berlin: Springer.

Appendix A:

Synchronicity of optical and accelerometric data.

The prototype of the data logger was tested in a series of experiments in similitude to those carried with a cylinder intruding into granular matter. Some of the experimental settings were changed to solve the challenges met in the processing of the data of the previous one.

That problematic was:

The variable shadows on the background of the image sequence disturbing the processing. Those shadows are originated by the punctual light focus outside the experimental cell. As the cell vibrated, and the intruder moves, the shadows blurred the cylinder with the background boundaries.

This problem was solved by fixing a pair of LED lamps to the front wall of the cell, directing to the laterals of the cylinder. This setup almost annulated the lateral shadow while the intruder oscillated in the experiment.

The distortion of the mark as a consequence of the reflections on the cylinder's face. The contrast differences is the main feature to spot the mark the mark to the surroundings. The position of the center of mass is calculated whit the help of the center of the mark's area in the region properties Matlab's structure. The spurious variations of brightness and contrast troubled the tracking through the program leading to a noisy position's data series.

The solution taken was to place a bigger mark joined to a better light disposition letting to better handle the losses due to reflections and in complement, to simplify the angle's measurement.

The light gray color of the original intruder returned a chromatic composition almost indistinct from that of the shadowed granular surface in the image processing. The way to separate the cylinder image from the background is to discriminate the contrast differences and this is perturbed by the shadows.

The cylinder in the new arrangement was printed in a yellow polymer; this made easy to "sieve" the intruder by separating the areas by their chromatic components. The Matlab's 2014a release provides an application suitable for this purpose.

Furthermore, a good definition of the body's boundaries gave a secondary resource to measure the tilt on the image, for the cases were the mark is too much blurred for the border lines of any of the sides to be used to measure the angle.

The experimental array was simplified placing the cell over railings tightening it directly to the shaker. This new arrangement discharged the shaker from useless loads that endangered the safe operation of the power amplifier and the mechanic shaker's systems.

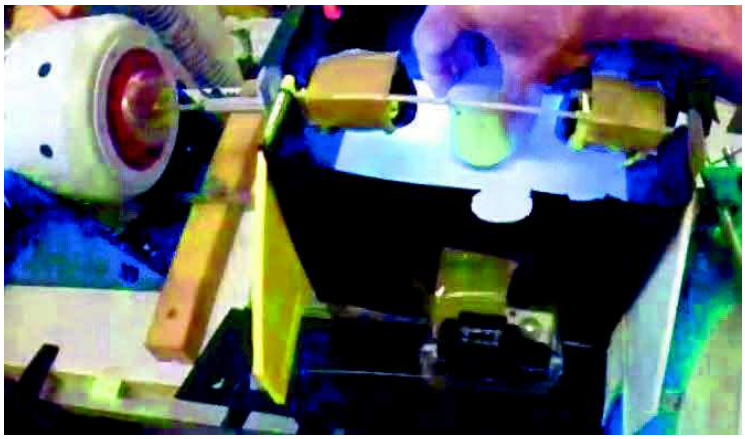

Figure A1 Experimental setup to test the instrumented intruder.

The new series of experiments returned a double data set, one from the recorded film with the images of the intruder, the other one saved in the SD card with the acceleration and angle information from the IMU. (Inertial Measurement Unit)

The dimensions of the prototype dictates to put the device standing up on the center of the hollow cylinder. To feed the electronics a pack of three AAA cells was used, letting us to disregard about the power all along the time of the experiment. The weight of the battery pack and some ballast of added sand made the cylinder isodense with the surrounding effective density of the granular medium.

Since it is positioned in the center of the hole, the data logger was oriented with the Z axis pointing to the front side, in an imaginary line across the mark. In this way the X axis sensed the static gravity's acceleration, normal to the granular bed's surface, and the Y axis was collinear with the shaking force.

Experimental procedure.

This method aims to the test of the performances of the instrumented cylinder with the SD data logger. It is not intended to reproduce the results of the foundation's experiments because the

battery pack displaced the intruder's center of mass out of the geometric center. The main purpose is to develop a procedure to check the matching of the optical data from the image processing with the numerical accelerometric information from the data logger.

In first place, to put the SD card in the socket, turn on the data logger and place it in the intruder, taking care of the orientation of the IMU as explained before in order not to need to readjust the software by reassigning the axis to the reference's frame.

The next step is to assert the jumper intended to enable the recording, from that moment on the data logger is saving data to a file in the SD card. The cylinder is covered with the cap and situated on the center of the granular surface, the lamps are turned on. The camera is also turned on and before the cap of the cell is put down to close the scenery to the spurious reflections, a small shock is applied to the cylinder, in the way the movie's set "clap" which will allow to synchronize the image and the sensors data.

After the vibrations ended, when the sinking or tilting process is completed, all the procedure is done backwards. In the updated Arduino's sketch there is no need to take out the SD card since a new data file will be created every time the jumper is asserted again.

The data processing is analogous to that of the matt or shallow foundation experiments, with the precisions given in the previous paragraphs. An updated Matlab's script was developed corresponding to the new experimental features.

Matlab's code to synchronize the data series.

In order to synchronize the data from both origins a Matlab's script is done. The following code yielded a plot displaying the variation in the acceleration curve of the X axis of the intruder to the sinking of the cylinder in an experiment carried out with a sinusoidal shaking, with an amplitude corresponding to a peak to peak source at 300 mV used in the TIRA shaker at full amplification, and a frequency of 5Hz, both events synchronized.

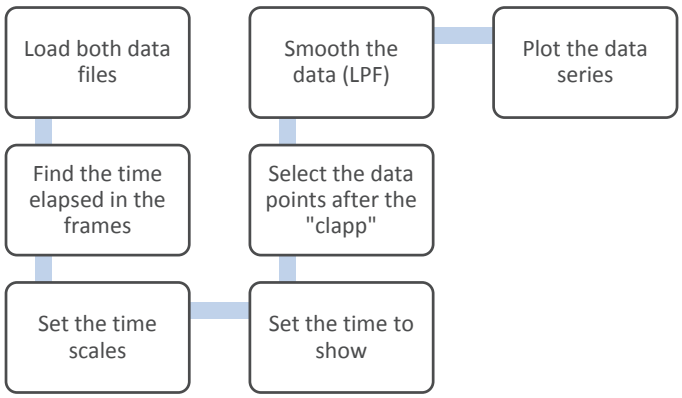

Matlab's script.

Figure A2 Algorithm to set the synchronicity of the accelerometer data to the cylinder's trajectory.

```
close all
clear all
Acc = importdata('fxN5_300a.txt') ;%data from datalogger
CM = importdata('N5XY300aFIT.txt');%data from image process
Acx = Acc(:,1);%take x axis acceleration (normal to the surface)
dim = size(Acc);
s = dim(1);%lenght of Acc data array
Ach = reshape(Acx(12:end),24,59);
AHght=smooth(Acx,23);%smoothing Acc data by moving average span=23
AH = AHght/16535;%Set to the g scale (16 bit, +/-2g)
Adt = 0.0246;%16s/650;%data rate measured between known sequence's points
Tsc = (1:812)'*Adt;%n data points * data rate = time scale
AHp = AH(151:962,:);%151 first data point, 962 last to be plotted

p=2575;%Frames to be processed
%%%%%%%%%%%%%%%%%%%%%%%%%%%%%%%%%%%%%%%%%%%%%%%%%%%%%%%
%Smoothing sinking data
R=round(p/3);
Cy=zeros(3,R);%Remember it should be trasposed to Rx3
P=(R-1)*3;%Frames - 3
Tm=(1:R);
%%%%%%%%%%%%%%%%%%%%%%%%%%%%%%%%%%%%%%%%%%%%%%%%%%%%%%%
%Pixel to mm
ls=4.18;%181pix/44mm

hs=(401/ls);%401 pixels frame height to mm scale
Tmp=Tm*(20/R);%for this experiment time = 20s
%%%%%%%%%%%%%%%%%%%%%%%%%%%%%%%%%%%%%%%%%%%%%%%%%%%%%%%
%smoothing, moving average span 3 steps lead
for n=1:P
    Cy(n)=CM(n)+CM(n+1)+CM(n+2);
    Cy(n)=Cy(n)/3;
end
cY=Cy';    %Traspose to Rx3
```

```
%%%%%%%%%%%%%%%%%%%%%%%%%%%%%%%%%%%%%%%%%%%%%%%%%%
% Plot Image vs accel data
 subplot(2,1,1)
 % plot(Tmp(2:857),cY(2:857,3)),title('Profondeur N5-300a')
 plot(Tmp(2:857),cY(2:857,3)),title('Depth trial N5-300a')
%
  ylabel('Height in mm');
  xlabel('Time in sec');
 hold on
 subplot(2,1,2)
 plot(Tsc,AHp),title('Acceleration normal to ground  N5-300a')
    ylabel('Acceleration in g');
 xlabel('Time in sec');

%publish('PlotImAc.m','doc');
%winopen('html/PlotImAc.doc');
```

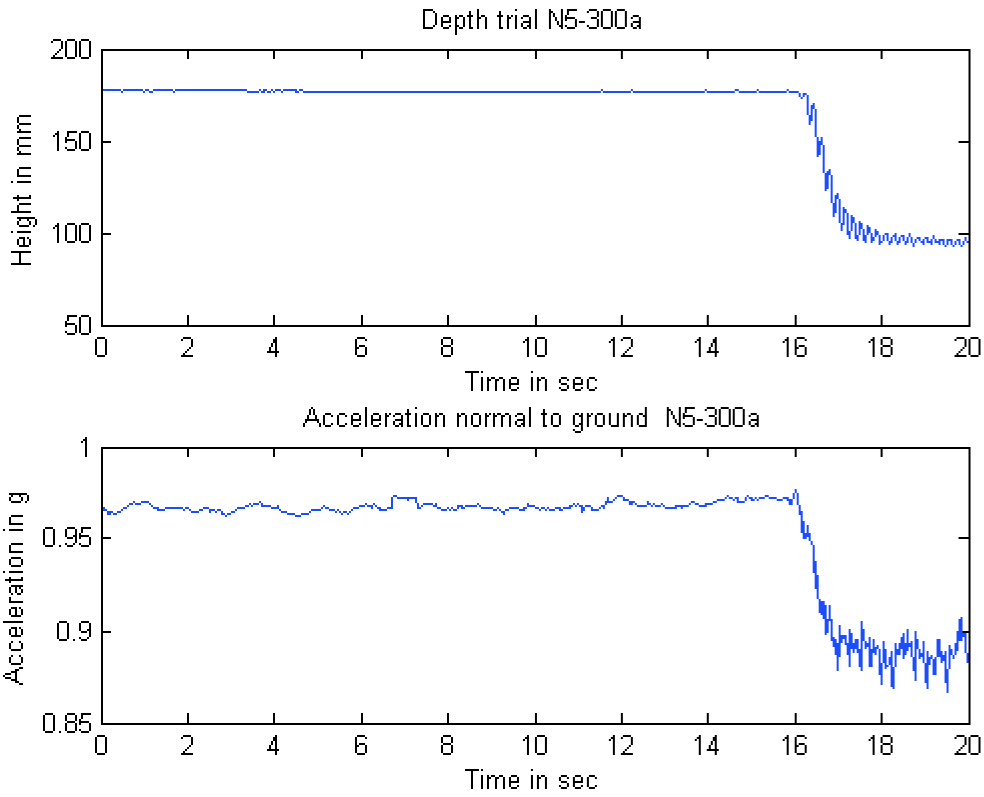

:

Figure A3 Correspondence between intruder's movement and acceleration's variation in time.

Appendix B:

Arduino's sketches.

Sketch for the acquisition on line.

The ADXL345 3D accelerometer is a digital MEMS that can use I2C and SPI serial interfaces. In this application the SPI interface is used. The main code is based in the code examples found in: http://sparkfun.com/tutorial/ADXL/ADXL345_Basic.pde.

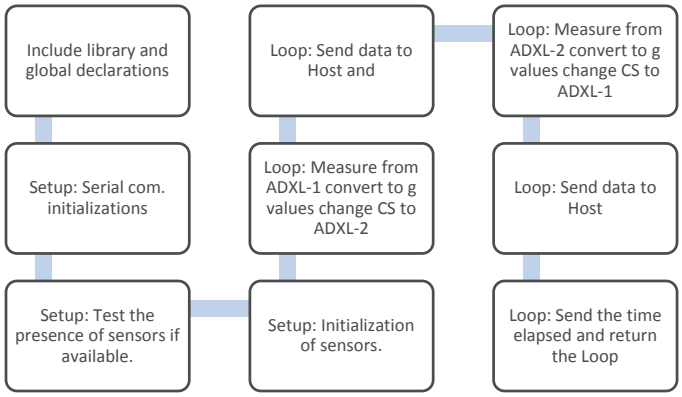

Figure A4 Algorithm for the on line data acquisition.

Excerpt from the sketch for the dual accelerometer on line measurement device:

```
void setup(){
  //Initiate an SPI communication instance.
  SPI.begin();
  //Configure the SPI connection for the ADXL345.
  //Create a serial connection to display the data on the terminal.
  Serial.begin(9600);
    //Set up the Chip Select pin to be an output from the Arduino.
  //Before communication starts, the Chip Select pin needs to be set high.
    //Put the ADXL345 into +/- 4G range by writing the value 0x01 to the DATA_FORMAT
register.
  //Put the ADXL345 into Measurement Mode by writing 0x08 to the POWER_CTL register.
```

```
  void loop()
{
Serial.print(time);
    Read_ADXL1();//Reference accelerometer
  //Print the results to the terminal.
  CS=9;
    Read_ADXL2();//Measurement intruder's accelerometer
  //Print the results to the terminal.
  CS=10;}
```

Instead of a specific library to drive the ADXL345, the registers are read/written using the SPI standard library. The changes introduced to the example code were to implement the reading of the accelerometers as functions, adding a time counter to facilitate the numerical processing of data and effectuate the digital numbers to normalized-by-g dimensional conversion in the Arduino itself.

Sketch for the micro-SD card data logger:

This sketch is based in the standard library for the SD card in the Arduino IDE developed by Tom Igoe, combined with the Invensense'sMPU6050 drivers built-in on the I2Cdev libraries and example codes from Jeff Rowberg.

This is the sketch used to test the instrumented intruder. Later, a function was incorporated enabling to dynamically create a new data file whenever a new experiment starts. The dynamic file creation eases the experimental procedure, as it is not needed to take out the SD card from the intruder on every iteration.

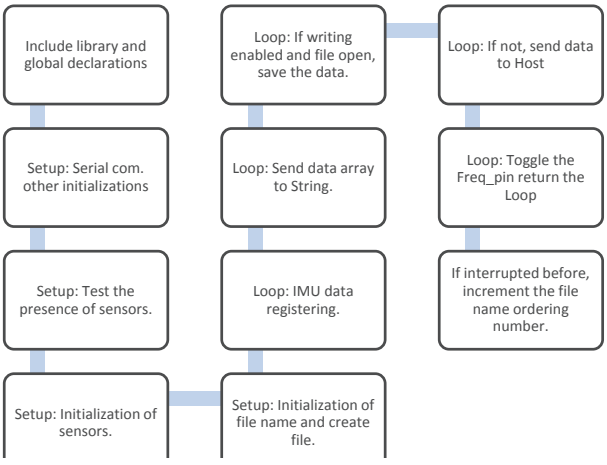

Figure A5 Algorithm for data logging to a micro-SD card.

Excerpt from the sketch uploaded to the SD data logger:

Includes, definitions and declaration of libraries and other variables.

```
// #include <string.h>                    //Standard C library
#include "I2Cdev.h"                       //Library to handle I2C devices
#include "MPU6050.h"                      //Library specific for the MPU6050
#include <SPI.h>                          //Generic SPI Arduino's library
#include <SD.h>                           // SD card specific library
//constintchipSelect = 4;                 // default Chip Select in the Igoe's SD library.
 #include "Wire.h"                        //Generic I2C Arduino's library
MPU6050 accelgyro(0x69);                  // <-- I2C default address for the IMU.
#define FREQ_PIN 7                        //toggling pin to measure the data throughput.
#define STOP_PIN 6                        //Stop of recording pin.
charStrName[13] ;                         //String to save the file name.
charfilName[12] ;                         //Variable to save the new file name.
File logFile;                             //File variable.
```

This is the setup section on the Arduino code.

```
void setup(){
Serial.begin(38400); // Open serial communications and wait for port to open:
if (!SD.begin(chipSelect)) {// see if the card is present and can be initialized:
Serial.println("Card failed"); // don't do anything more:}
Serial.println("card init.");
Wire.begin();
// initialize IMU
accelgyro.initialize();
        accelgyro.setFullScaleGyroRange(2); //set gyro range to +-1000°/s
                                  // verify connection
Serial.println(accelgyro.testConnection() ? (F("MPU conn successful")) :(F( "MPU conn
failed")));
```

```
 if (!accelgyro.testConnection()) return;
Extent = genFiles();// Create a file name template, the extension will change with the iteration.
sprintf(StrName,"SDE_%04d.txt",Extent);                //Template to complete 4digits with 0's
for  (inti = 0;i<13;i++){//fileName a Char
filName[i]=StrName[i];      }
}


void loop()
{
// create a string for assembling the data to log:
  String dataString = ""; //re-initialized chars string to contain the data values.
                            /*Measurement section */
     accelgyro.getMotion6(&ax, &ay, &az, &gx, &gy, &gz);       //Data from IMU
                            // display tab-separated accel/gyro x/y/z values
//         dataString += String(nLoop);
//        dataString += "\t";
dataString += String(ax);//Pass the data from the register to the string.
                                                    •  .
                                                    •  .
                                                    •  .
dataString += "\t";
dataString += String(gz);
STOPBIT = digitalRead(STOP_PIN);   //Check the pin to see if the experiment will continue.
if (!STOPBIT){ logFile = SD.open(filName, FILE_WRITE);}// Then open the file to write.
else {Serial.println(dataString);}       // If not, send it to the host computer via serial-USB.
  if (logFile) {    logFile.println(dataString);//If there is connection to SD and file is ready
logFile.close();            }     //write and close.
 else {    Serial.print(F("error opening file"));}//if the file isn't open, pop up an error:
FreqState = !FreqState ;                  //Toggle the auxiliary variable
digitalWrite(FREQ_PIN, FreqState); // Toggle the frequency measurement pin status
```

}//end of loop section.

Measuring the data logging sample rate.

Data throughput measurement setup:

The FREQ_PIN enabled us with a tool to measure the data throughput of the SD card data logger. Previously an additional variable counting the elapsed time has been implemented, wasting extra processor time, and worst, lengthening the throughput as another long variable has had to be written to the SD card.

The frequency, corresponding to the data throughput for this data logger was measured by a PM2661 high resolution timer/counter connected to the FREQ_PIN. The pin status toggled after every measurement –the saving cycle is completed. The resulting measured frequency stays around 48Hz. The imprecision in the frequency values seems to be due to the variation in the data throughput since the length of the chain variables corresponding to the measured values changed. The test of correspondence in the first of this Appendixes confirmed the measured frequency value.

Sketch for the wireless data logger.

This application is based on the libraries for the transceiver module using the NRF24L01 chip from Nordic Semiconductors, combined with the same libraries for the IMU as in the SD data logger. The NRF24L01 is a single chip RF-transceiver intended for applications in the 2.4 GHz ISM band. (Industrial, Scientific and Medical band)

This system was tested and it can send and receive data accurately to 4m in air with the on board antenna.

The Arduino sketch is based on a combination of the example included in the nRF24L01 library and the sketch for the MPU6050 IMU. The library for the RF transceiver was downloaded from: https://github.com/maniacbug/RF24.

The transceiver module is controlled through a SPI protocol plus a CE Pin to control the RX / TX modes. The transceiver is able to send and receive packets from 16, max 32 bytes, the specialist must take care to keep channel and payload (number of data bytes) definitions the same for all modules (called as nodes in network's vocabulary).

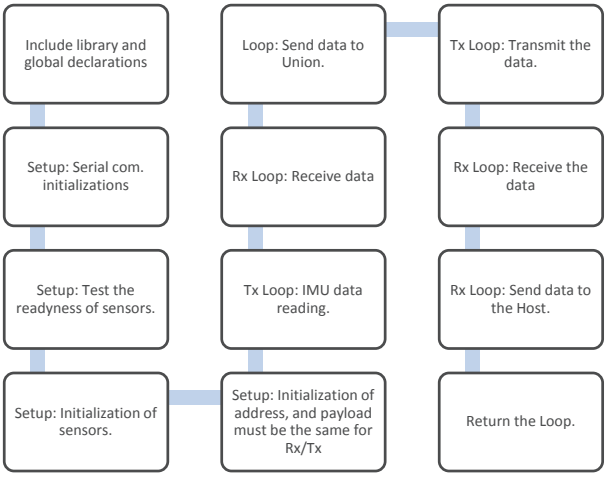

Figure A6 Algorithm for the wireless data acquisition.

Excerpt from the transmitter sketch:

In the following code excerpt the sections concerning the functions of the transceiver will be omitted for clarity. Only the meaningful declarations and the data manipulation is shown.

File: EF_nRF24L01_TX.ino

```
#include <SPI.h>
#include "API.h"
#include "nRF24L01.h"
#include "I2Cdev.h"
#include "MPU6050.h"
#define TX_ADR_WIDTH    5   // 5 unsigned chars TX(RX) address width
#define TX_PLOAD_WIDTH    12  //  12 unsigned chars TX payload
unsigned char TX_ADDRESS[TX_ADR_WIDTH]   =  {   0x34,0x43,0x10,0x10,0x01}; //
//Define a static TX address
charrx_buf[TX_PLOAD_WIDTH] = {0}; // initialize data buffer array.
unsigned char tx_buf[TX_PLOAD_WIDTH] = {0};
MPU6050 accelgyro(0x69);                              // <-- use for AD0 high
```

In the Loop section the received values are stacked in a union to simplify the values type conversion from word to byte before being transmitted.

```
typedefunion {                int16_t DWr;
                               int8_t DCh[2];       } daTxis;//will be the data type
```

```
daTxisdataTx[7];                                        //array for data values

void setup()              // condensed setup section
{  Serial.begin(9600);
SPI.begin();
Serial.println(" EF_nRF24L01_TX_MPU...");
Serial.println("**********TX_Mode Start**********");
TX_Mode();                                                  // set TX mode
Wire.begin();
accelgyro.initialize();                                     // initialize device        }

void loop()
{                          // read raw accel/gyro measurements from device
   accelgyro.getMotion6(&ax, &ay, &az, &gx, &gy, &gz);
dataTx[0].DWr= ax;
                                                    •   .
                                                    •   .
dataTx[5].DWr= gz;
  for(inti=0; i<7;i++){// here the value bytes are transmitted separately
tx_buf[2*i] = dataTx[i].DCh[0];
tx_buf[2*i+1] = dataTx[i].DCh[1];
       }
   unsigned char sstatus = SPI_Read(STATUS);            // read register STATUS's value
   if(sstatus&TX_DS)                                    // if receive data ready (TX_DS) interrupt
   {
SPI_RW_Reg(FLUSH_TX,0);
SPI_Write_Buf(WR_TX_PLOAD,tx_buf,TX_PLOADWIDTH);  //write payload to TX_FIFO
   }
```

Excerpt from the sketch for the wireless data logger in receiver mode:

This piece of code is further abridged as it shares the libraries and initialization with the transmitter. The data manipulation in the loop section of the sketch is shown.

```
** Device: nRF24L01+
** File: EF_nRF24L01_RX.c
#define TX_ADR_WIDTH    5   // 5 unsigned chars TX(RX) address width
#define TX_PLOAD_WIDTH  12  // 12 unsigned chars TX payload
unsigned char TX_ADDRESS[TX_ADR_WIDTH] = {   0x34,0x43,0x10,0x10,0x01}; // Define a
static TX address
unsigned char rx_buf[TX_PLOAD_WIDTH] = {0}; // initialize value
unsigned char tx_buf[TX_PLOAD_WIDTH] = {0};
//************************************************
typedef union{
       int16_t DWr;
        int8_t DCh[2];
} daTxis;
daTxisdataTx[6];
```

In the Loop section the received valuesarestackedin a union to simplify the type conversion from word to byte before the data is sent via a serial port to the host computer.

```
void loop()
{for (;;)  {
   unsigned char status = SPI_Read(STATUS);                    // read register STATUS's value
   if(status&RX_DR)                                          // if receive data ready (TX_DS) interrupt
   {
SPI_Read_Buf(RD_RX_PLOAD, rx_buf, TX_PLOAD_WIDTH);    // read playload to rx_buf
SPI_RW_Reg(FLUSH_RX,0);                                    // clear RX_FIFO
     for(inti=0; i<7; i++)      {
dataTx[i].DCh[0]= rx_buf[2*i];
dataTx[i].DCh[1]= rx_buf[2*i+1];
Serial.print(dataTx[i].DWr);
Serial.print("\t");      }
Serial.println("");    }  }}
```

ABSTRACT

Gustavo Sánchez

Physique et ingénierie des catastrophes naturelles: techniques accélérométriques et optiques pour le suivi de pénétration d'intrus solides dans des sols liquéfiés.

Résumé

Cette thèse porte sur le développement de méthodes et techniques expérimentales pour mieux connaître les principes à l'œuvre dans les glissements de terrains, les avalanches, les écoulements granulaires qui ont un grand rôle dans la liquéfaction des sols, ayant pour conséquences possibles la chute ou l'enfoncement de bâtiments. On conjugue ici des expériences de géophysique expérimentale avec des expériences de physique des milieux granulaires, et en parallèle on développe des appareils de mesure basés sur des microcontrôleurs et capteurs embarqués.

Nous employons des méthodes appliquées en laboratoire de physique des milieux granulaires à l'étude de l'écoulement d'intrus et à des problèmes de recherche en géophysique, tout d'abord, dans le but général de tester l'influence de la pesanteur sur la mobilité des intrus dans des milieux granulaires. Ensuite, dans le but de tester l'influence de la forme des piliers de soutènement sur la pénétration ou la stabilité des intrus dans des milieux granulaires soumis à différents degrés d'excitation horizontale.

On présente des expériences qui établissent dans le principe un lien entre la forme des piliers des bâtiments et leur stabilité pendant des tremblements de terre, utilisant également des procédés de laboratoire d'étude des milieux granulaires étendues aux études de géophysique expérimentale. Cette expérience effectuée entièrement dans l'atelier de géophysique expérimentale à l'IPGS a montré clairement que la forme des piliers influe sur la stabilité des bâtiments en les faisant s'enfoncer ou basculer quand on les soumet à des vibrations ressemblant des tremblements de terre. Les mesures effectuées dans ces expériences ne reposent pas sur de l'accélérométrie, mais sur un traitement d'images optiques. Les résultats

obtenus expérimentalement sont reproduits par des simulations numériques effectués en collaboration avec Cécile Clément, IPGS.

On présente un travail publié dans Review of Scientific Instruments, portant sur des expériences sur le suivi du centre de masse d'un intrus lors de son enfoncement dans un milieu granulaire vibrant. Ici on emploie un accéléromètre sans fil pour acquérir les données d'accélération de l'intrus. La cellule où a lieu l'expérience était soit tridimensionnelle, soit quasi-bidimensionnelle selon le modèle de Hele-Shaw. Le matériau granulaire est composé de grains polymériques autour de 2mm de diamètre. L'ensemble est soumis à des vibrations horizontales de fréquence et amplitude contrôlées. On a monté un double système de suivi optique et électronique de l'intrus avec une caméra qui enregistrait le mouvement du centre de masse, et on applique un traitement numérique des images pour calibrer le suivi de l'intrus par l'accéléromètre. Les données acquises ainsi sur la position par double intégration sont dominées par le bruit, car l'enfoncement de l'intrus est un processus trop lent par rapport à la précision du système d'acquisition accélérométrique. On développe à cette fin une méthode auxiliaire qui permet d'obtenir une information pertinente sur l'état de liquéfaction du milieu proche de l'intrus, par inter corrélation des données d'accélération de l'intrus avec les données d'accélération d'un capteur fixé à la cellule d'essai. Par analogie avec la technique de « Lock-in amplifier », cette technique est nommée « Lock-in accelerometry ».

On applique une formule de corrélation de Pearson modifiée entre l'accélération horizontale de l'intrus et celle du capteur de référence, le coefficient r apporte l'information sur l'approche par l'intrus de la couche non fluidisée en profondeur du milieu granulaire liquéfié:

$$r_{(k)} = \frac{\sum_{i=k}^{k+D} a_x^R(i) a_x^P(i)}{\sqrt[2]{\left[\sum_{i=k}^{k+D} \left(a_x^R(i)\right)^2 \sum_{i=k}^{k+D} \left(a_x^P(i)\right)^2\right]}}$$

Le coefficient r se rapproche de 1 lorsque les deux signaux sont corrélés, c.à.d. lorsque se réduit le déphasage entre les signaux, représentes ici par respectivement accélération de l'intrus et du capteur de référence.

Dans un autre procédé, avec une machine d'Atwood de 15 mètres d'hauteur, sur lequel opère un contrepoids; on contrôle l'accélération éprouvée par la cellule où l'expérience a lieu. Un intrus contenant un capteur d'accélération sans fil recueille les données de son mouvement (accélération) pendant qu'il s'introduit dans un matériau granulaire très léger presque sans friction. En plus de ces capteurs, on emploie des transmetteurs et récepteurs Wifi et Bluetooth pour parvenir à ce contrôle. Les résultats montrent que la profondeur d'enfoncement maximale

ne dépend pas de la pesanteur effective à laquelle a lieu l'expérience. Dans le contexte général de développement de véhicules d'exploration interplanétaire sur milieux granulaires (sables) sous d'autres gravité, ces résultats, imprévus, sont très remarquables. Ces travaux ont été publiés dans Geophysical Research Letters.

Dans le dernier chapitre, on détaille les instruments développés pour le suivi des expériences. Aujourd'hui l'application des microcontrôleurs embarqués est généralisée grâce à l'intégration de nouvelles techniques avec des logiciels pour en faciliter l'emploi. S'étant restreint pour la faisabilité du système à ceux possibles à développer dans les institutions à bas budget, on a choisi la plateforme Arduino, très bien connue parmi les expérimentateurs. Arduino associe à son design ouvert un environnement de développement programmé en langage C, standard indépendant du système d'opération. De plus, l'Arduino n'a pas besoin d'appareil dédié pour télécharger le programme dans la puce électronique embarquée, un logiciel (boot loader) enregistré à priori dans le microcontrôleur étant dédié à cette tâche.

On a développé, testé et recensé divers moyens pour l'archivage ou la transmission des signaux, chacun présentant ses avantages et ses inconvénients, selon l'application visée.

Abstract

The subject of this thesis are the methods and experimental technics to help in the assessment of the underlying principles for the landslides, runaways and the other phenomena playing a main role in soil liquefaction and hence, on the falling or settling of buildings. This thesis conjugates geophysics' to granular materials physics' experiments, and it allowed to develop new measurement devices based on embedded microcontrollers.

Laboratory methods from granular materials physics to study the gliding of intruders were applied to geophysical problems focusing on the determination of the influence of gravity on the mobility of intruders penetrating on granular material. Next, experiments were done to test the influence of the shape of foundations on the mobility of the stability of buildings by means of intruders submitted to different degrees of horizontal vibration on a granular bed.

Those experiences demonstrated at first a relationship between the foundation's shape and the building stability in the course of the earthquake. It was shown in the experiments that the foundation's shape does impact the leaning to settle or to tilt a building during the horizontal

oscillations. The measurements were handled entirely by numerical processing of digitized images. At IPGS Cecile Clement confirmed the practical yields through numerical methods by simulating the experimental arrangement.

A paper published on Review of Scientific Instruments on the subject of the tracking of an intruder sinking in a granular bed under horizontal vibrations is presented. A wireless accelerometer and a 3D cell or a Hele-Shaw cell were used to perform quasi two-dimensional experiments. As a granular material a set of 2mm diameter polymeric spheres was employed. The experimental setup is submitted to vibrations of controlled frequency and amplitude. The track of the intruder is done both by optical and electronics methods. Via numerical processing of images is obtained the calibration data for the tracking of the intruder through the accelerometer. The data returned by the experiment is submerged in spurious noise because the acceleration's magnitude is too small. An auxiliary technique was developed to enable to recover the key information on the status of liquefaction of the medium close to the intruder, by correlating the intruder's accelerometer with a reference accelerometer data. The technics was called "Lock-in accelerometry" in similitude to the well-known data treatment method.

In practice the Pearson's correlation formula with a modification is applied to the acceleration data coming from the axis collinear with the vibration direction on both accelerometers. The r Pearson's coefficient yields the information about the approaching the intruder to the no-liquefied zone of the granular bed. As the correlation of both signals rises, the r coefficient approaches to 1, which means that the phase difference is shrinking.

$$r_{(k)} = \frac{\sum_{i=k}^{k+D} a_x^R(i) a_x^P(i)}{\sqrt[2]{\left[\sum_{i=k}^{k+D} \left(a_x^R(i)\right)^2 \sum_{i=k}^{k+D} \left(a_x^P(i)\right)^2\right]}}$$

The following experience involves a 15 meters tall Atwood's machine regulated by a counterweight to control the acceleration of the experimental cell. An instrumented intruder with an embedded wireless accelerometer measures the movement as the intruder sinks in an almost frictionless granular bed. Besides the wireless sensors, Bluetooth and Zig-bee transceivers were used to remotely control the experiment. The outcomes established that the maximal sinking distance isn't determined by the effective gravity.

Having in mind the possible generalization of the experiment to extraterrestrial scout vehicles travelling over sands or dust on diverse gravities, this unexpected achievement is remarkable. The paper was published in Geophysical Research Letters.

Eventually, some instruments developed to measure the experimental parameters are detailed here. Taking in account the broad use of embedded microcontrollers and cybernetics, the restrictions imposed to the design were economy (price), viability and readiness in view of the low budget institutions. The Arduino platform was chosen because it is well known among the researchers and is open source. On top of all this, Arduino supplements with standard C programming an IDE Java based independent of the operating system. Moreover, Arduino doesn't need a special burning or programming apparatus to upload the code on the microcontroller since it is furnished with a boot-loader code.
Several procedures and materials for data logging were put under test to check the strength and weaknesses of each one and the results are presented.

Résumé Long

Introduction.
Un risque naturel peut être défini comme un événement naturel subi qui présente un danger potentiel, c'est-à-dire peut causer des dommages aux personnes et aux constructions. C'est un phénomène environnemental qui peut être induit par des phénomènes atmosphériques, hydrologiques, géologiques et liés aux feux de forêt. Le niveau de hasard associé à ces menaces varie en fonction de l'emplacement, de la saison et de la probabilité qu'un risque particulier survienne. Certains d'entre eux - comme les tempêtes tropicales et les éruptions volcaniques - peuvent être partiellement prévus, tandis que d'autres - comme les tremblements de terre, les coulées de boue et les tornades - ne peuvent pas avec précision en temps ou en espace à l'heure actuelle. Cette thèse portera sur les catastrophes naturelles associées aux sols granulaires, en particulier lorsqu'elles sont fluidisées, par exemple en présence de vibrations - qui peuvent survenir lors de séismes.

En quelques secondes, un tremblement de terre peut causer des dégâts considérables et laisser des milliers de personnes mortes, blessées ou sans abri. La perturbation des lignes de vie, des systèmes de transport et des systèmes de communication peut être critique. Les principaux

risques géologiques associés aux tremblements de terre de grandeur modérée à grande comprennent le tremblement de terre, la rupture de surface et l'affaissement tectonique, la liquéfaction du sol et les défaillances du sol connexes, les glissements de terrain et divers types d'inondations.

L'attention de cette thèse se concentrera principalement sur la pénétration des intrus dans les lits granulaires secs fluidisés, comme modèle expérimental pour les bâtiments, voire les véhicules. La fluidisation peut être provoquée par des vibrations - comme dans le cas d'un tremblement de terre - par la contrainte associée à la pénétration d'un intrus dans un matériau granulaire particulier - comme dans le cas de grains ultralégers - ou même pendant la pénétration dans un environnement de gravité réduite - comme c'est le cas à la surface sableuse d'un astéroïde. Dans le chapitre 1 de cette thèse, une introduction à la pénétration des intrus dans un milieu granulaire sec est fournie.

Le chapitre 1 ne traitera pourtant pas de la pénétration à grande vitesse des intrus (Ciamarra, Lara, Golman, Vishik et Swinney, 2004), un sujet très étudié en rapport avec la balistique et des cratères d'impact dans les objets sidéraux. Le chapitre vise à la physique de la pénétration à basse vitesse, en incluant le cas où l'intrus repose initialement sur la surface granulaire libre. Il est discuté du travail séminal de Tsimring et Volfson (Tsimring & Volfson, 2005) où les expériences et les simulations sont utilisées pour déterminer les principales contributions à la dissipation d'énergie pendant la pénétration d'un intrus dans un lit granulaire. Ils concluent que les principales sources de dissipation sont: (a) Les collisions inélastiques entre les grains et entre les grains et l'intrus (b) Le frottement dû au glissement des particules et au glissement des intrus (c) L'énergie cinétique du granulaire dans le matériau éjecté lors de la collision dans l'air et (d) l'énergie potentielle accrue du lit granulaire due à la pénétration de l'intrus.

Des expériences soigneuses du groupe de Doug Durian ont abouti à une loi de force dite «universelle» pour la pénétration lente des intrus dans le matériel granulaire (Katsuragi et Durian, loi de force unifiée pour les cratères d'impact granulaires, 2007). En principe, il est possible d'écrire la seconde loi de Newton pour l'intrus où la force gravitationnelle agit verticalement vers le bas et deux forces distinctes associées au matériau granulaire agissent verticalement vers le haut: (a) une force "visqueuse", associée à des chocs entre l'intrus et les grains et (b) une force "dépendant de la profondeur" exprimée en une certaine constante

multipliée par la profondeur dans le matériau granulaire. La force n'est pas complètement comprise, mais elle est définitivement reliée à certains des mécanismes de dissipation décrits par Tsimring et Volfson (Tsimring & Volfson, 2005). Fait intéressant, la constante de proportionnalité entre la profondeur et la force dépendante de la profondeur dépend de la taille et de la forme de l'intrus, et de la gravité.

Quelques années plus tard, Pacheco et ses collègues (Pacheco-Vazquez, Caballero-Robledo et al. 2011) proposent une version raffinée de la «loi universelle» de Katsuragi et de Durian: ils modifient ainsi le terme de force «indépendant de la profondeur» pour que l'interaction avec les parois du récipient soit incluse: différemment des liquides ou des solides, la matière granulaire présente des "chaînes de force", c'est-à-dire qu'un grain qui interagit avec une paroi par frottement, peut transmettre cette interaction au centre du conteneur à travers des chaînes de grains qui sont en bon contact mécanique les uns avec les autres: les murs aident de cette façon à supporter le poids d'un intrus situé au milieu d'un silo granulaire. Pacheco et ses collègues ont introduit une dépendance exponentielle dans le terme de force dépendant de la profondeur de telle sorte que l'effet de Janssen soit pris en compte: pour les petites profondeurs de pénétration, la loi de Katsugari et de Durian est récupérée, alors que pour des profondeurs de pénétration élevées, le terme est indépendant de la profondeur, ce qui permet d'atteindre une "vitesse terminale" (typique de la pénétration dans les fluides). L'équation de mouvement de Pacheco et de ses collègues (Pacheco-Vazquez, Caballero-Robledo, et al. 2011), servira de cadre pour expliquer le comportement des intrus pénétrants examinés dans les chapitres suivants.

Structure par chapitres de la thèse :

La thèse est organisée en cinq chapitres, dont quatre associés à des articles scientifiques. Déplacement dans le sens des aiguilles d'une montre, en commençant par le coin supérieur gauche: Le chapitre 1 offre une introduction sur la pénétration des intrus dans la matière granulaire. Par traitement d'images, le chapitre 2 présente les résultats originaux relatifs à la pénétration d'un intrus dans la matière granulaire fluidisée par vibrations, et comment elle dépend de sa fondation. En utilisant un accéléromètre sans fil, le chapitre 3 fournit de nouveaux aperçus sur la pénétration d'un intrus dans la matière granulaire fluidisée par la contrainte, à différents niveaux de gravité effective. Le chapitre 4 introduit une nouvelle technique pour l'étude de la dynamique de pénétration dans de la matière granulaire fluidisée par vibrations utilisant un couple d'accéléromètres sans fil. Le chapitre 5 introduit la mise en œuvre de

différentes plateformes électroniques pour l'étude de la pénétration d'intrus dans des lits granulaires fluidisés au moyen de capteurs miniatures.

Mais revenons au sujet de la fluidisation des sols. L'importance de cet effet dans le scénario des catastrophes naturelles peut être illustrée par le cas du tremblement de terre de Kocalei survenu le 17 août 1999. Il a gravement endommagé de nombreuses constructions dans la ville d'Adapazari, en Turquie. En particulier, certains bâtiments ont sombré dans le sol, d'autres ont penchés, et un troisième groupe s'est même déplacé latéralement, vraisemblablement en raison de la liquéfaction des sols (Sancio, Bray et al. 2004). En fait, les ondes de cisaillement libérées pendant les tremblements de terre finissent par générer une contrainte de cisaillement cyclique qui mène à l'accumulation graduelle de la pression de l'eau interstitielle. Cela peut aboutir à une liquéfaction prolongée, qui a été étudiée sur des sols sablonneux, granulaires et sédimentaires (Berrill et Davis, 1985) (Obermeier Stephen F, 1996) (Vanneste K. Meghraoui M. Camelbeeck T, 1999). Mais, comment une construction artificielle comme un bâtiment réagirait en étant placé sur un sol partiellement fluidisé à cause des ondes sismiques? Peut-il s’enfoncer, ou éventuellement pencher? Le comportement dépend-il de l'intensité et de la fréquence de l'onde sismique? Ou peut-être la forme et la taille de la construction est l'élément clé pour prédire son sort? Nous tenterons de répondre à certaines de ces questions dans le premier des articles présentés dans cette thèse, qui est présenté au chapitre 2.

La configuration expérimentale présentée au chapitre 2 simplifie le scénario réel en utilisant une configuration très élémentaire: une boîte de sable sec est secouée latéralement, de telle manière que l'amplitude et la fréquence des oscillations sont contrôlées. La compréhension de la dynamique des objets qui pénètrent dans les milieux granulaires a rapidement évolué au cours de la première phase de l'étude (Altshuler et al., 2003) (Altshuler et al., 2008) (Torres, Gonzalez, et al., 2011) (PachecoVázquez, Caballero-Robledo et al., 2011) (Katsuragi et Durian, loi de force unifiée pour les cratères d'impact granulaires, 2007) (Uehara, Ambroso, Ojha et Durian, Als., 2012) (Goldman et Umbanhowar, 2008) (Boudet, Amarouchene, et al., 2006) (Kondic, Fang, et al., 2012). Dans ce contexte, les lits granulaires secoués latéralement ont reçu un certain degré d'attention (Metcalfe, Tennakoon, et al. 2002), mais la performance des objets posés initialement à la surface d'un lit granulaire soumis à une secousse latérale a été beaucoup moins étudiée (Tennakoon, Kondic, et Behringer, 1999) (Liu & Dobry, 1997). Le sujet est abordé au chapitre 2 de la présente thèse.

L'objet pénétrant étudié ici est un «bâtiment modèle»: il consiste simplement en un cylindre imprimé en 3D avec un fond plat, étudié et comparé à un cylindre similaire où une «fondation en anneau» est ajoutée. Contrairement à l'intuition, pour un éventail de fréquences et d'amplitudes disponibles dans les conditions de laboratoire - et en rapport avec des scénarios sismiques réels - on observe le comportement suivant: les «bâtiments cylindriques modèles» à fond plat descendent verticalement, tandis que ceux avec une fondation en anneau, penchent. Les détails de la dynamique sont soigneusement suivis par l'analyse d'images de vidéos prises avec une caméra attachée à la boîte secouée latéralement, avec des outils informatiques ad hoc créés pour la suivre.

Malgré ce comportement assez surprenant, l'explication physique des phénomènes observés est assez simple. Tout d'abord, il faut dire que, comme un lit granulaire est secoué horizontalement, il y a une couche distincte de matière granulaire fluidisée à une certaine profondeur de la surface libre, qui augmente en général avec l'accélération maximale adimensionnée par la pesanteur de la secousse: la couche fluidisée agit, à bien des égards, comme un vrai liquide. Au-dessous, le lit granulaire ressemble à un solide. Lorsqu'un cylindre à fond plat est libéré sur la surface libre, s'il descend juste verticalement, il finit par s'arrêter lorsque son fond atteint la phase solide du lit granulaire. Cependant, si un anneau est ajouté au fond du cylindre, le frottement contre le sable secoué latéralement augmente à la base du cylindre, produisant un couple de basculement. En conséquence, le cylindre s'incline – en plus de l'enfoncement. Le penchement est toutefois également constaté dans le cas des cylindres sans anneau si l'on dispose d'une agitation latérale suffisamment forte - un cas qui n'est pas facilement réalisable par l'installation expérimentale disponible.

Dans le document présenté au chapitre 2, les données expérimentales en 3D sont corroborées par des simulations informatiques 2D où les grains en forme de disque et les cylindres plats avec et sans fondement suivent la dynamique newtonienne de base. De plus, la dynamique d’enfoncement observée expérimentalement est reproduite à l'aide d'une équation de mouvement qui considère l'interaction de l'intrus avec la matière granulaire suivant une équation de mouvement convenablement modifiée (Pacheco-Vazquez, Caballero-Robledo et al.) comme précisé auparavant.

Le chapitre 3 utilise un outil différent pour étudier la pénétration dans un milieu granulaire très léger: un accéléromètre sans fil monté à l'intérieur d'un intrus sphérique. Ici, le lit granulaire n'est pas secoué: il est aisément fluidisé par la contrainte causée par la pénétration de l'intrus due à la pesanteur, puisqu'il consiste en grains ultralégers de polystyrène expansé introduit à l'origine par Pacheco et ses collègues (Pacheco-Vazquez, Caballero-Robledo, et al. 2011). La pénétration de l'intrus est suivie avec un accéléromètre sans fil, dont la sortie est intégrée deux fois pour obtenir l'enregistrement vitesse / temps, puis l'enregistrement profondeur / temps. À la connaissance des auteurs, il s'agit de la première recherche systématique sur la pénétration d'un intrus équipé d'un accéléromètre sans fil en matière granulaire. Du point de vue physique, cependant, la principale nouveauté de ce travail est le fait que le processus de pénétration a été étudié à différentes gravités effectives, équivalentes à des expériences réalisées dans d'autres planètes, comme sur Mars ($g(Mars) \approx 0.4g(Terre)$). Ce type d'étude est potentiellement important pour la conception de véhicules de prospection capables d'opérer efficacement sur des surfaces de sable à des gravités inférieures (et aussi plus élevées) que celle de la Terre. Les différentes densités sont atteintes d'une manière très simple et peu coûteuse: au lieu d'utiliser des avions zéro-g ou d'effectuer des expériences dans une station spatiale, une machine Atwood de 15 mètres de long est utilisée pour contrôler l'accélération de l'un des contrepoids, qui est, en fait, un laboratoire granulaire accéléré, contrôlé et appareillé pour les mesures grâce à l'utilisation de la technologie sans fil.

Les expériences ont révélé deux faits principaux: (a) La profondeur maximale de pénétration de l'intrus est indépendante de la gravité et (b) Le temps total de pénétration est proportionnel à l'inverse de la racine carrée de l'accélération correspondante à la pesanteur effective. La première découverte est tout à fait inattendue, mais peut être rationalisée de la façon suivante: à mesure que la gravité diminue (ou augmente), le poids de l'intrus diminue (ou augmente), mais cet effet est compensé par une diminution de l'inertie et de la contrainte dans le matériau granulaire qui se traduit par différents niveaux de dissipation. Ces hypothèses qualitatives peuvent être justifiées quantitativement en utilisant l'équation du mouvement proposée par Pacheco et ses collègues (Pacheco-Vazquez, Caballero-Robledo et al. 2011) en supposant que le coefficient de proportionnalité entre la force dépendante de la profondeur et la profondeur de pénétration (dans le cas des pénétrations faibles) est proportionnel à la gravité effective. La découverte expérimentale que la pénétration maximale est indépendante de la gravité peut être potentiellement utile pour concevoir des rovers pour Mars plus efficaces, et aussi pour

expliquer les caractéristiques de la surface de Mars et d'autres corps astronomiques, tels que les cratères et les ravines (Shinbrot, Duong et al. 2004) (Aspaugh, 2007) (Almeida, Parteli, et al. 2008).

Comme indiqué précédemment, l'intégration de l'enregistrement d'accélération verticale permet de déterminer l'évolution de la vitesse et de la profondeur au fil du temps. Les données sont bonnes pour des pénétrations relativement rapides dans un lit de billes de polystyrène expansé, mais elles sont trop bruitées si l'intrus pénètre à faible vitesse: c'est le cas typique de la pénétration dans un lit de sable agité horizontalement. En particulier, si un intrus pénètre dans une boîte tridimensionnelle de sable qui est fluidisé par secousses horizontales, les vidéos sont utiles lorsqu'une partie de l'intrus est à l'extérieur du sable (le cas décrit au chapitre 1), mais elles ne le sont pas lorsque l'intrus s'enfonce complètement dans le lit granulaire. Donc, si la vidéo et les techniques accélérométriques simples ne sont pas assez bonnes pour suivre tout le processus de pénétration, que peut-on faire?

Une réponse possible est présentée au chapitre 4 de la thèse. Une cellule de Hele-Shaw pleine de sable est secouée latéralement et un intrus est placé à la surface du sable pour observer le processus de pénétration, qui est observé - à titre de référence - au moyen d'une caméra vidéo attachée au système d'agitation horizontale cadre de référence. Le coeur du système de mesure est le déploiement de deux accéléromètres identiques et sans fil: un (appelé Ref) est fixé à la cellule de Hele-Shaw, tandis que le second (appelé Probe) est attaché à l'intrus s’enfonçant. Au lieu d'enregistrer les accélérations verticales - inutiles ici pour cause de trop lent processus de pénétration - nous enregistrons les accélérations horizontales, puis calculons la corrélation entre elles, à travers le coefficient de Pearson. Cette idée est inspirée des amplificateurs Lock-in (LIA), un instrument couramment utilisé pour mesurer des tensions de bas niveau. Dans un montage typique, un échantillon est excité avec un courant alternatif, qui est également injecté par l'entrée "Ref" du LIA. Le signal de sortie de l'échantillon - qui est une "version modifiée" de l'excitation d'entrée grâce aux propriétés physiques de l'échantillon - est ensuite injecté par la borne "In" du LIA. Ensuite, le dispositif multiplie et filtre les deux signaux. Il est facile de montrer que le résultat est un signal continu proportionnel à la propriété physique de l'échantillon qui est censée être mesuré et, ce qui est tout à fait important, la plupart des bruits externes sont éliminés. Il est facile de voir l'analogie entre le LIA et le concept d'accélérométrie de Lock-in présenté ici.

L'idée de l'expérience spécifique présentée dans cette thèse est la suivante: lorsque l'intrus s'enfonce, il ne peut pas être étroitement lié à la masse granulaire, il y aura donc un délai entre les accélérations horizontales mesurées par Ref et Probe, donc la corrélation entre eux se rapproche de zéro. D'autre part, lorsque l'intrus termine le processus d'enfoncement et parvient dans la «phase granulaire solide», il commence à se mouvoir de façon synchrone avec le référentiel, et la corrélation entre les accélérations Ref et Probe approche l'unité. Au moins, en utilisant cette méthode, nous pouvons déterminer le moment exact où l'intrus cesse de s'enfoncer.

Des expériences préliminaires montrent que nous pouvons (a) détecter le moment où l'intrus touche la "phase solide" à la fin du processus d'enfoncement et (b) identifier au moins différents stades pendant le processus avant l'arrêt: un de pénétration rapide et un second de pénétration lente, "rampante". À l'avenir, il convient d'examiner si l'étude d'autres caractéristiques de la corrélation en plus de son amplitude pourrait être utilisée pour révéler des caractéristiques plus subtiles de la dynamique de pénétration. Bien que la méthode d'accélérométrie de Lock-in ait été présentée ici, elle pourrait être intéressante comme un système standard pour suivre le mouvement des structures artificielles ou naturelles lorsqu'elles s'enfoncent ou se déplacent dans des sols soumis à des secousses sismiques.

Jusqu'à ce stade, les expériences décrites dans la thèse ont utilisé (a) un équipement d'acquisition vidéo standard et (b) des plateformes d'accéléromètres sans fil qui sont disponibles sur le marché avec un logiciel propriétaire. Dans le dernier chapitre de la thèse, un certain nombre de nouvelles plateformes capables de supporter des capteurs miniatures développés par l'auteur sont présentées. En outre, une plate-forme accélérométrique sans fil comme celle utilisée jusqu'ici a de sérieuses limitations pour certaines expériences et applications d'intérêt géophysique et environnemental. Un exemple illustre l'idée: l'étude de l'effet d'érosion des vagues et des vents sur le fond des plages sablonneuses de Cuba - un problème important aggravé par les fréquentes tempêtes associées à El Niño. Une possibilité d'effectuer une telle étude consiste à monter des capteurs sans fil et des dispositifs GPS dans des «roches témoins» et à les déployer à des points critiques au fond d'une plage: les capteurs à l'intérieur de la roche permettraient de reconstituer le mouvement de l'échantillon sur le sable, dans des conditions entièrement naturelles. Le rocher agira comme intrus étudié dans des

conditions de laboratoire dans les chapitres précédents, et le fond sablonneux sera un lit granulaire fluidisé - à cause de la secousse associée aux vagues, et à la présence de fluide réel.

Un accéléromètre sans fil posera de sérieux défis techniques dans une telle expérience, puisque le signal peut être facilement perdu pour au moins trois causes: (a) Si la roche se déplace à plus de 10 mètres du récepteur (même dans l'air), le signal est interrompu B) La situation décrite est finalement aggravée par l'eau de mer elle-même, qui peut agir comme un bouclier électromagnétique et (c) La nécessité d'avoir un récepteur relativement près de la roche portant le capteur pendant toute l'expérience peut être gênant - et éventuellement un environnement venteux. Ensuite, l'enregistreur de données embarqué semble la solution: le capteur acquière et stocke les données dans un dispositif local de mémoire miniature également incorporé au système embarqué dans la roche, et ils sont transférés plus tard sur un ordinateur.

ARDUINO (Severance, Janvier 2014) a été le choix comme plate-forme pour contrôler les capteurs miniatures. Il a essentiellement tous les avantages recherchés dans cette thèse: le design est ouvert, et peut être programmé en langage C, un standard indépendant du système d'exploitation. Surtout, il peut être assemblé de manière assez compacte, ce qui facilite son déploiement dans, par exemple, une roche marine. Des capteurs comprenant un accéléromètre triaxial et un module sans fil sont commandés par l'Arduino. Pour le stockage des données, un nombre de normes ont été étudiées, en tenant compte de différents paramètres, tels que la capacité de stockage, la vitesse d'acquisition des données, la marge d'erreur dans le transfert de données, l'autonomie de fonctionnement - essentiellement donnée par la consommation d'énergie - et la capacité de contrôler plusieurs capteurs. Ainsi, par exemple, alors que Bluetooth excelle en termes de capacité de stockage et d'autonomie, les cartes micro-SD sont le meilleur choix quand la multiplicité est nécessaire. Les mémoires FRAM, d'autre part, sont excellentes en termes de multiplicité et de vitesse. Ces choix - toujours sous la plate-forme ARDUINO - sont essayés préliminairement en laboratoire (intrus pénétrant dans une boîte de sable secoué) et dans des conditions naturelles, lorsqu'il est installé dans des roches déployées dans une plage de sable cubaine.

En résumé, l'objectif de base de la thèse est d'étudier le comportement des intrus dans la matière granulaire fluidisée, créant éventuellement de nouvelles techniques expérimentales pour atteindre cet objectif.

En particulier, les objectifs de la thèse sont:

A) Déterminer l'influence du type de sous-sol dans le comportement d'un cylindre utilisé comme modèle d'une construction humaine ou d'une roche, lorsqu'il pénètre dans un lit granulaire sec fluidisé par vibrations.

B) Établir l'influence de la gravité dans la pénétration d'un intrus sphérique dans un matériau granulaire léger, mesurée par accéléromètres sans fil.

C) Créer une technique accélérométrique permettant d'étudier la lente pénétration d'un intrus dans des matériaux granulaires fluidisés par vibrations.

D) Mettre en œuvre une plate-forme basée sur Arduino à logiciel ouvert pour étudier le comportement des intrus dans la matière granulaire fluidisée, tant en laboratoire qu'en conditions naturelles.

Résumé par chapitres.

Chapitre 1: Pénétration des intrus dans les milieux granulaires secs: Concepts de base.

La pénétration d'objets solides dans les sols a été, pendant longtemps, l'arène des ingénieurs civils, des scientifiques de la Terre et des astronomes. Cependant, depuis les années 1990, la question est devenue un «sujet brûlant» des physiciens. En particulier, au cours de la dernière décennie, la «compréhension physique» de la résistance aux objets pénétrant dans les milieux granulaires a rapidement progressé (Walsh, 2003) (Uehara, Ambroso, Ojha, & Durian, 2003) (Kakura et al., 2002) (Katsuragi et Durian, loi de force unifiée pour les cratères d'impact granulaires, 2007) (Pacheco-Vazquez, Caballero-Robledo et al., 2011) (Boudet, Amarouchene, et al., 2006) (De Vet & de Bruin, 2007) (Chen, Umbanhowar et al., 2009) (Brzinski et Durian, 2010) (Constantino, Bartell et al. , (2012) (Katsuragi, Pression de la paroi non linéaire d'une colonne granulaire plongée, 2012) (Kondic, Fang, et al., 2012) (Ludewig, Dorbolo, & Vandewalle, 2004). Dans ce chapitre, un nombre limité de résultats clés seront brièvement présentés dans ce domaine. En raison de sa connexion directe aux chapitres ultérieurs de la thèse, l'accent sera mis sur la lente pénétration des intrus dans la matière granulaire - un exemple typique étant un objet qui commence son mouvement d'une position de repos sur la surface granulaire libre. Pour un aperçu plus général de ce domaine, il est recommandé de consulter la revue récente de C. Ruiz Suárez (RuizSuarez, 2013).

Chapitre 2: Pénétration Vs. Inclinaison dans un matériau granulaire secoué: le rôle de la fondation.

Les expériences rapportées dans le présent chapitre étudient une variable généralement négligée dans l'étude du comportement du bâtiment stressé par un séisme: la forme de la fondation.

L'architecture établit une diversité de fondations, regroupées sous les classifications des fondations superficielles ou profondes. Les fondations superficielles sont de loin les plus utilisées pour les bâtiments ménagers, parce qu'elles sont technologiquement faciles et accessibles - il est peut-être raisonnable de les identifier avec les cylindres à fond plat étudiés plus haut dans le présent chapitre. Les fondations superficielles sont également les plus touchées par la fluidisation du sol dans les séismes. Avec cette motivation, nous avons conçu et mené des expériences pour étudier les fondations de manteau ou de semelle filante, et la base circulaire (bande, étendue continue ou pied de mur). Les fondations profondes, en tant que piliers, descendent habituellement jusqu'à la roche mère ou jusqu'à la zone sûre où il n'y a aucune chance de liquéfaction - ces fondations pourraient être identifiées avec les cylindres de sous-sol en forme d'anneau. Ensuite, il semble raisonnable de faire une étude approfondie des effets des tremblements de terre sur les bâtiments réels avec des fondations superficielles et profondes et les comparer avec les résultats de laboratoire rapportés précédemment dans le présent chapitre.

Chapitre 3: Simulations de pénétration dans des milieux granulaires secs de différentes densités.

Nous utilisons la modélisation par éléments discrets (DEM) pour simuler une grande sphère qui s'enfonce dans un lit granulaire composé de plus petites sphères (Poschel & Schwager, 2005). La mise en œuvre est un algorithme hybride CPU / GPU qui nous permet d'évaluer efficacement la dynamique de plusieurs centaines de milliers de particules (Owens, Alain, Marion, & Kuttel, 2013) Houston, Luebke, et al. 2008). Nous débutons chaque simulation en générant un empaquetage granulaire aléatoire de sphères mono disperses (rayon r et densité ρ) à la fraction d'emballage φ = 0,62 ± 0,02. L'intrus sphérique (R = 8r et densité ρint = 50ρ) est positionné sur la surface granulaire libre avec une vitesse initiale nulle.

Pour chaque particule i = 1 ... N la simulation DEM comprend trois degrés de liberté de translation et le mouvement de rotation est décrit par un formalisme de quaternion. La force d'interaction entre la particule i et la particule j est composée de composantes normales et tangentielles $\vec{F}_{ij}= \vec{F}_{ij}^{n}+ \vec{F}_{ij}^{t}$. Dans notre approche, la force d'interaction normale entre les particules $\vec{F}_{ij}^{t}$ dépend non linéairement de la distance de chevauchement des particules. De plus, la dissipation locale est introduite par un terme d'amortissement visqueux non linéaire, qui dépend de la vitesse relative normale $\overrightarrow{v}_{rel}^{n}$. Par conséquent,

La force normale totale se lit comme $\overrightarrow{F_{ij}^{n}} = -k_n\delta^{\frac{3}{2}}\hat{n} - \gamma_n m_e \vec{v}_{rel}^{n}\delta^{\frac{1}{4}}$, où kn et $\gamma_n$représentent des coefficients élastiques et d'amortissement et me = mimj /(mi + mj). La composante tangentielle $\vec{F}_{ij}^{t}$ comprend également un terme élastique et un terme visqueux,$\vec{F}_{ij}^{t} = k_t\vec{\varepsilon} - \gamma_t m_e \vec{v}_{rel}^{t}$, où $\gamma_t$est un coefficient d'amortissement et $\vec{v}_{rel}^{t}$la vitesse relative tangentielle de la paire se chevauchant. La variable $|\vec{\varepsilon}$ représente l'allongement d'un ressort imaginaire à constante élastique kt. Tant qu'Il y a un chevauchement entre les particules qui interagissent, $|\vec{\varepsilon}|$ augmente lorsque d$\vec{\varepsilon}$/dt = $\vec{v}_{rel}^{t}$ (Pöschel et Schwager, 2005). L'allongement tangentiel élastique $|\vec{\varepsilon}|$ est maintenu orthogonal au vecteur normal (Weinhart et al, 2012) et il est tronqué comme nécessaire pour satisfaire la contrainte de Coulomb $|\vec{F}_{ij}^{t}| < \mu|\vec{F}_{ij}^{n}|$, où μ est le coefficient de frottement.

Le mouvement de translation et de rotation de chaque particule est régi par l'équation du mouvement de Newton.

Les équations du mouvement sont intégrées à l'aide de l'algorithme leap-frog de Fincham, (rotationnel) (Fincham, 1992) et d'un algorithme Verlet Velocity (translation) (Verlet, 1968). Le pas de temps de la dynamique moléculaire a été fixé dans Δt = 10−6s. Dans toutes les simulations présentées ici, on a utilisé les valeurs de constante élastique kn = 1.2 × 106N/m3/2, densité ρ = 14 kg/m3, coefficient d'amortissement normal γ_n= 12 et friction μ = 0,5. On maintient kt/kn = 2/7et γ_t/γ_n = 0.1, et on modifie seulement le champ gravitationnel $\hat{g}$ d'une simulation à l'autre. Les valeurs de pesanteur sont normalises avec la pesanteur de la Terre geff g/ge.

CHAPITRE 4:«Accélérométrie de Lock-in» pour suivre la dynamique d'enfoncement en matière granulaire secouée.

Comprendre la dynamique de pénétration des intrus dans les lits granulaires est pertinent non seulement pour la physique fondamentale, mais aussi pour les processus géophysiques et la construction sur les sédiments ou les sols granulaires dans les zones potentiellement affectées par les tremblements de terre. Dans ce travail, nous utilisons l'accélérométrie de Lock-in pour étudier la pénétration des intrus dans la matière granulaire sous conditions quasi-2D fluidisée par tremblement latéral. Nous avons observé qu'il y a deux stades bien définis dans la dynamique de pénétration lorsque l'intrus sombre dans le matériau granulaire.

En appliquant une force oscillatoire externe, il est possible de trouver une transition d'une phase solide à une phase fluidisée dans un milieu granulaire (Duran, 1999). Un tel effet provoque la perte de résistance du matériau et provoque un objet posé sur sa surface à sombrer latéralement (Duran, 1999). Cette fluidisation a un effet destructeur pendant les tremblements de terre, car le bâtiment sur ses surfaces perd la stabilité et finit par s'effondrer (Ambraseys, 1988) (Conseil, 1985) (Wang, 2014). Bien que les tremblements de terre ne puissent pas être prévus, les séquelles peuvent être réduites (Ambraseys, 1988). Dans cet article, nous proposons une technique expérimentale visant à comprendre les effets de la fluidisation afin d'atteindre ces objectifs.

Alors que dans les systèmes quasi-2D la pénétration d'un intrus peut être suivie au moyen d'une caméra vidéo (Sanchez, 2010) (Niebling, 2010), dans le cas de systèmes 3D de grains opaques, ce n'est pas possible. L'accélérométrie sans fil a été utilisée à quelques reprises pour quantifier, autant que nous le sachions, la dynamique d'enfoncement d'un intrus (Pacheco-Vazquez, Caballero-Robledo, & Al., 2011) (Altshuler, 2014). Dans cette note nous utilisons une méthode appelée Lock-in accélérométrie (LIA), précédemment rapportée par notre groupe afin de contourner ces problèmes (Sánchez, 2014). En conséquence, nous sommes en mesure d'établir deux étapes bien définies dans la dynamique de pénétration d'un intrus dans la matière granulaire secouée, à mesure que la profondeur de pénétration augmente.

L'essence de la technique LIA est l'utilisation combinée de l'information de l'accéléromètre fixé à la cellule de Hele-Shaw (Ref) et de l'accéléromètre à l'intérieur de l'intrus (Probe). Ensuite, le paramètre expérimental utilisé pour étudier le processus d'affaissement est la corrélation entre les accélérations horizontales des deux accéléromètres. Pour cela on utilise une modification du coefficient de corrélation de Pearson visant à diminuer le bruit dans la sortie qui consiste à calculer l'évolution du coefficient de Pearson dans des intervalles de temps de taille D, chacun à partir du moment K.

$$r_{(k)} = \frac{\sum_{i=k}^{k+D} a_{xR}(i) a_{xP}(i)}{\sqrt[2]{\left[\sum_{i=k}^{k+D} \left(a_{xR}(i)\right)^2 \sum_{i=k}^{k+D} \left(a_{xP}(i)\right)^2\right]}}$$

L'idée clé derrière cette technique est que quand l'intrus est en mouvement, il y aura un délai entre axR, axP et le coefficient de corrélation sera plus petit qu'un. Lorsque la profondeur augmente, la corrélation augmente lorsque l'intrus avec la sonde approche la phase bloquée dans le système granulaire. Enfin la valeur de la corrélation doit atteindre un plateau proche de

1 indiquant la fin du processus d'enfoncement, si l'intrus se déplace de manière synchrone avec la référence.

Dans la présente contribution, nous avons étudié les matériaux secs, mais la technique peut également être utilisée pour la matière granulaire humide. Finalement, la substitution de l'intrus par une roche solide et le lit granulaire par un sol réel peut étendre la technique pour mesurer, in situ, la réponse rhéologique d'un sol lors d'un tremblement de terre.

CHAPITRE 5: Techniques ad hoc impliquant des capteurs miniatures pour l'étude de la dynamique d'enfoncement.

Une des objectifs de cette thèse est le développement de dispositifs à intégrer dans les intrus utilisés dans les expériences de pénétration. Ils doivent être à portée et réparables par des chercheurs qui ne sont pas nécessairement formés en électronique.

La plate-forme Arduino semble être la plus appropriée pour réaliser les objectifs de la thèse en raison des facteurs suivants:

1. Bon rapport qualité / prix.
2. Open source à la fois pour le circuit et le logiciel.
3. Une grande communauté d'utilisateurs qualifiés prête à consulter sur le WEB.

L'Arduino a été construit sur une plaque adaptatrice QFP32 à DIP de 400 mm x 200 mm avec les pièces minimales pour le rendre fonctionnel. C'est le noyau autour lequel des composants du système sont emmenés pour adapter la conception à chaque expérience particulière. Dans l'Arduino utilisé dans cette thèse, le pont USB-TTL n'est pas inclus, car une fois téléchargé le programme, le pont n'est pas nécessaire si les données ne sont pas directement transférées vers l'hôte via USB.

Il y a quatre cas particuliers avec les configurations correspondantes d'Arduino. À chaque configuration correspond un programme spécifique, entraînant le capteur ou le dispositif d'enregistrement de données propres :

1. Acquisition de données en ligne.
2. Enregistrement de données sur une mémoire externe.
3. Enregistrement des données sur une carte micro-SD.
4. Acquisition de données sans fil.

Conclusions et perspectives.

Dans la présente thèse, la pénétration des intrus dans la matière granulaire fluidisée a été étudiée à l'aide de techniques optiques et d'accélérométrie miniature, dont certaines ont été créées ad hoc.

En particulier, l'auteur a pu:

A) Déterminer l'influence du type de sous-sol dans le comportement d'un cylindre utilisé comme modèle d'une construction humaine ou d'une roche, lorsqu'il pénètre dans un lit granulaire fluidisé par vibrations: les cylindres à fond plat tendent à couler verticalement, pendant que les cylindres à fond avec anneau tendent à tomber latéralement - bien que ce dernier comportement tende à dominer pour des secousses latérales très fortes. Cette étude peut aider à comprendre les dommages structurels qui se produisent aux constructions artificielles pendant les tremblements de terre et autres catastrophes naturelles.

B) Établir l'influence de la pesanteur pendant la plongée d'un intrus sphérique dans une matière granulaire légère, mesurée par accéléromètres sans fil: la profondeur totale d'enfoncement est indépendante de la pesanteur, tandis que le temps total d'écoulement augmente comme l'inverse de la racine carrée de la pesanteur. Cela peut éclairer sur la façon de concevoir des véhicules de prospection pour se déplacer sur des surfaces sablonneuses de différentes planètes et astéroïdes, et peut être utile pour interpréter les données géomorphologiques de ces corps astronomiques.

C) Créer la technique dite «d'accélérométrie de Lock-in» pour étudier la lente pénétration d'un intrus dans des matériaux granulaires fluidisés par vibrations lorsque les techniques accélérométriques optiques et conventionnelles ne sont pas applicables. La technique peut être étendue pour obtenir des données pendant les catastrophes naturelles où la fluidisation du sol est présente.

D) Mettre en œuvre une plate-forme basée sur Arduino à logiciel et noyau ouverts pour étudier le comportement des intrus dans la matière granulaire fluidisée, tant en laboratoire qu'en conditions naturelles. En particulier, une évaluation détaillée des différents systèmes de stockage a été réalisée. La plate-forme a été essayée préliminairement pour obtenir des données accélérométriques des roches se déplaçant sur le fond d'une plage de sable réelle-un scénario pertinent pour l'étude de la dynamique d'érosion.

Plusieurs perspectives (non exhaustives) de ce travail peuvent être envisagées:

Le développement d'accéléromètres et de gyroscopes intégrés légers, équipés d'enregistreurs de données, permet de planifier une campagne visant à étudier l'érosion des plages, comme par

exemple celles de Cuba fortement soumis à l'érosion. Équiper des roches de différentes tailles, densités et formes devrait permettre d'étudier leur dynamique pendant plusieurs conditions de mer sur les plages. Avec des mesures à grande échelle basées sur la stéréophotogrammétrie effectuée sur des images acquises par des quadricoptères sans pilote, ceci devrait permettre de progresser sur la compréhension de la dynamique des milieux granulaires saturés associés aux processus d'érosion. Les accéléromètres peuvent être distribués dans des roches superficielles très mobiles, et peuvent être distribués à une plus grande profondeur pour surveiller l'inclinaison associée à une dégradation lente de la plage.

Les mêmes types d'accéléromètres peuvent également être déployés en intrus le long des berges afin d'évaluer leur stabilité, ou en cas de lents glissements de terrain. En effet, les chutes de pierres et les glissements de terrain sont parmi les principaux risques naturels en Europe, et de ce fait sont d'un grand intérêt commun. Le faible coût de la plate-forme développée devrait permettre de déployer des réseaux de capteurs dans les zones d'intérêt.

Les recherches qui continuent l'étude du frottement dans des matériaux granulaires secs oscillants peuvent également être étendues à des surfaces partiellement ou totalement saturées. En effet, souvent la présence d'eau affecte profondément la capacité des sols à se liquéfier lors de tremblements de terre ou de fortes précipitations.

Un autre sujet connexe, où les capteurs pourraient être couplés à des dispositifs oscillants autonomes, est l'étude des sables mouvants. Ce phénomène fascinant est peu étudié in situ. Accéléromètres de couplage + gyroscopes embarqués avec une source d'oscillation autonome dans les intrus pourraient permettre de tester in situ la rhéologie des sables mouvants dans les régions où ceux-ci apparaissent naturellement.